2017

Chemical Exchange Saturation Transfer Imaging Of Endogenous Metabolites For Monitoring Oxidative Phosphorylation And Glycolysis In Vivo

Catherine Debrosse
University of Pennsylvania, debrosse@mail.med.upenn.edu

Chemical Exchange Saturation Transfer Imaging Of Endogenous Metabolites For Monitoring Oxidative Phosphorylation And Glycolysis In Vivo

Abstract
Oxidative phosphorylation (OXPHOS) and glycolysis are two cellular metabolic pathways that play a crucial role in the functions of biological systems. Currently, magnetic resonance spectroscopy (MRS) (13C, 31P, and 1H) and positron emission tomography (PET) methods are used to investigate changes in these pathways that result from metabolic dysfunction. However, MRS methods are limited by low resolution and long acquisition times. While 18F-fluoro-2-deoxy-D-glucose (18F-FDG) PET is a widely used clinical modality, it requires the use of radioactive ligands. Thus, there is an unmet need for techniques to image these metabolic processes noninvasively, and with higher resolution in vivo. In this dissertation, we exploited the chemical exchange saturation (CEST) phenomenon to develop and optimize endogenous CEST magnetic resonance imaging (MRI) methods to measure OXPHOS and glycolysis, and demonstrated application of those techniques to study impaired metabolism in vivo. These CEST methods offer several orders of magnitude higher sensitivity compared to traditional spectroscopic techniques. Recently developed CEST imaging of free creatine (CrCEST) was targeted as a means of measuring OXPHOS. We optimized and validated this technique in healthy human skeletal muscle, showing that CrCEST imaging in dynamic exercise studies provides a measure of the mitochondrial rate of OXPHOS. CrCEST imaging was then implemented in a cohort of subjects affected by genetic disorders of the mitochondria. The results of these studies demonstrate that CrCEST has the capability to distinguish between healthy and impaired OXPHOS in muscle. In some diseases with altered metabolism, like cancer, aerobic glycolysis dominates, leading to increased lactate production. Existing methods for imaging lactate in vivo involve expensive, radiolabeled tracers. In this work, we demonstrated the feasibility of imaging lactate with CEST ("LATEST") in phantoms with physiological concentrations. Then, we validated the method dynamically in vivo by measuring lactate production and clearance in intensely exercised human skeletal muscle, which utilizes anaerobic glycolysis. Finally, we infused rats bearing lymphoma tumors with non-labeled pyruvate and demonstrated the ability of LATEST MRI to image tumors and measure dynamic lactate changes over time. Together, these studies demonstrate that metabolic processes can be monitored in vivo using CEST MRI, with potential for widespread clinical applications.

Degree Type
Dissertation

Degree Name
Doctor of Philosophy (PhD)

Graduate Group
Biochemistry & Molecular Biophysics

First Advisor
Ravinder Reddy

CHEMICAL EXCHANGE SATURATION TRANSFER IMAGING OF ENDOGENOUS METABOLITES FOR MONITORING OXIDATIVE PHOSPHORYLATION AND GLYCOLYSIS IN VIVO

Catherine M. DeBrosse

A DISSERTATION

in

Biochemistry and Molecular Biophysics

Presented to the Faculties of the University of Pennsylvania

in

Partial Fulfillment of the Requirements for the

Degree of Doctor of Philosophy

2017

Supervisor of Dissertation

_____

Ravinder Reddy, Ph.D.
Professor of Radiology and Director, Center for Magnetic Resonance and Optical Imaging

Graduate Group Chairperson

_____

Kim A. Sharp, Ph.D.
Associate Professor of Biochemistry and Biophysics

Dissertation Committee:
Jerry D. Glickson, Ph.D., Research Professor of Radiology
John A. Detre, M.D., Professor of Neurology
Sergei Vinogradov, Ph.D., Associate Professor of Biochemistry and Biophysics
Kathryn E. Wellen, Ph. D., Associate Professor of Cancer Biology
David Roalf, Ph.D., Assistant Professor of Behavioral Neuroscience in Psychiatry
Michael T. McMahon, Ph.D., Associate Professor of Radiology and Radiological Sciences

CHEMICAL EXCHANGE SATURATION TRANSFER IMAGING OF ENDOGENOUS METABOLITES FOR MONITORING OXIDATIVE PHOSPHORYLATION AND GLYCOLYSIS *IN VIVO*

Dedicated to my parents, Joan and Charles

Acknowledgements

I would like to thank everyone who has supported me throughout my graduate school studies. I am especially grateful for the help and guidance from all the members of the Center for Magnetic Resonance and Optical Imaging, particularly for that of my advisor, Ravinder Reddy, who has encouraged me to always think critically about science. Thank you to Hari Hariharan for his hours spent teaching and for his constant patience. Thanks to Mark Elliott and Ari Borthakur for their answers to all my questions, from everything to statistics, data processing, politics, and beyond. I am eternally indebted to Ravi Nanga for patiently teaching me how to perform MRI experiments, and for being a wonderful friend during challenging projects. Special thanks to Susan Colleluori for her endless support and encouragement. I also want to acknowledge my former lab mate and student mentor, Rachelle Crescenzi, for her incredible friendship and determination, for being the best travelling companion for conferences, and for always having chocolate in her desk. Thanks to Shana McCormack for being a wonderful mentor and collaborator. Thanks to the friends I've made at Penn, for your support and enthusiasm and for sharing in each other's life milestones in addition to our educational ones. Finally, I would like to thank my family. My parents Joan and Charles always provided the best example of hardworking and passionate scientists, and constantly encouraged me to stick with it even when I felt challenged. I would like to thank my brother Patrick for his support and all of our entertaining conversations about the grad school experience. My husband Paul Selesky has been cheering me on from the day I was accepted to graduate school to my dissertation defense, and I'm incredibly thankful for his constant support.

ABSTRACT

CHEMICAL EXCHANGE SATURATION TRANSFER IMAGING OF ENDOGENOUS METABOLITES FOR MONITORING OXIDATIVE PHOSPHORYLATION AND GLYCOLYSIS IN VIVO

Catherine DeBrosse

Ravinder Reddy

Oxidative phosphorylation (OXPHOS) and glycolysis are two cellular metabolic pathways that play a crucial role in the functions of biological systems. Currently, magnetic resonance spectroscopy (MRS) (^{13}C, ^{31}P, and ^{1}H) and positron emission tomography (PET) methods are used to investigate changes in these pathways that result from metabolic dysfunction. However, MRS methods are limited by low resolution and long acquisition times. While ^{18}F-fluoro-2-deoxy-D-glucose (^{18}F-FDG) PET is a widely used clinical modality, it requires the use of radioactive ligands. Thus, there is an unmet need for techniques to image these metabolic processes noninvasively, and with higher resolution *in vivo*. In this dissertation, we exploited the chemical exchange saturation (CEST) phenomenon to develop and optimize endogenous CEST magnetic resonance imaging (MRI) methods to measure OXPHOS and glycolysis, and demonstrated application of those techniques to study impaired metabolism *in vivo*. These CEST methods offer several orders of magnitude higher sensitivity compared to traditional spectroscopic techniques. Recently developed CEST imaging of free creatine (CrCEST) was targeted as a means of measuring OXPHOS. We optimized and validated this technique in healthy human skeletal muscle, showing that CrCEST imaging in dynamic

exercise studies provides a measure of the mitochondrial rate of OXPHOS. CrCEST imaging was then implemented in a cohort of subjects affected by genetic disorders of the mitochondria. The results of these studies demonstrate that CrCEST has the capability to distinguish between healthy and impaired OXPHOS in muscle. In some diseases with altered metabolism, like cancer, aerobic glycolysis dominates, leading to increased lactate production. Existing methods for imaging lactate *in vivo* involve expensive, radiolabeled tracers. In this work, we demonstrated the feasibility of imaging lactate with CEST ("LATEST") in phantoms with physiological concentrations. Then, we validated the method dynamically *in vivo* by measuring lactate production and clearance in intensely exercised human skeletal muscle, which utilizes anaerobic glycolysis. Finally, we infused rats bearing lymphoma tumors with non-labeled pyruvate and demonstrated the ability of LATEST MRI to image tumors and measure dynamic lactate changes over time. Together, these studies demonstrate that metabolic processes can be monitored *in vivo* using CEST MRI, with potential for widespread clinical applications.

TABLE OF CONTENTS

LIST OF TABLES

LIST OF ILLUSTRATIONS

Chapter 1 - Chemical Exchange Saturation Transfer (CEST) and Metabolism

1.1 Introduction

The motivation for this dissertation work was to develop chemical exchange saturation transfer (CEST) magnetic resonance imaging (MRI) biomarkers of metabolism and demonstrate *in vivo* applications. In this chapter we will review the benefits of molecular imaging techniques for studying metabolism, describe the CEST theory and current applications, and then discuss the motivation for using CEST for imaging metabolic dysfunction.

Molecular imaging techniques have become vital tools for investigating biochemical processes *in vivo* (James and Gambhir 2012). They are particularly useful for studying disease mechanisms and pathology in living tissue. As we investigate the molecular basis of disease, the capability of measuring biological functions within a living subject becomes more and more important, particularly as the new molecular therapies are developed. Imaging techniques can be used in combination with other modalities to aid in diagnostics, drug development, and evaluating therapeutic efficacy.

Compared to traditional *in vitro* or *ex vivo* methods, molecular imaging has several key advantages (Wouters, Verveer et al. 2001). First, molecular imaging methods are relatively non-invasive. This allows us to study organisms, such as cells, living tissue, or live subjects, without disrupting the natural environment (Massoud and Gambhir 2003). Therefore, we can track dynamic biological processes *in vivo* and in real time, which provides a more comprehensive picture of the organism. Pre-clinical animal studies are

greatly benefitted by molecular imaging techniques as we can perform multiple studies per animal, ultimately using fewer research animals and gaining the ability to perform longitudinal studies. Molecular imaging also improves the development of therapeutics by aiding *in vivo* assessment of pharmaceutical metabolism and safety (Willmann, van Bruggen et al. 2008). Finally, most molecular imaging techniques provide sufficient temporal and spatial resolution, making them ideal for studying physiological processes in real time.

Many molecular imaging techniques, such as positron emission tomography (PET) (Phelps 2000, Blake, Johnson et al. 2003), computed tomography (CT) (Agatston, Janowitz et al. 1990, Lardinois, Weder et al. 2003), ultrasound (Christiansen and Lindner 2005), optical imaging (Couillard-Despres, Finkl et al. 2008), and photoacoustic imaging (de la Zerda, Liu et al. 2010, Wang and Hu 2012) have been developed in recent decades. While these techniques have many advantages (Plathow and Weber 2008) particularly in cancer imaging, they also possess some limitations, primarily use of ionizing radiation, limited tissue-penetration depth, or inherent low-quality soft tissue contrast that requires use of injected contrast agents (James and Gambhir 2012).

The work presented in this thesis utilized MRI, which has been used for decades to provide high-resolution anatomical images of human tissue (Lauterbur 1973). Compared to most other modalities MRI has excellent spatial and temporal resolution. Through the use of specialized pulse sequences we can acquire dynamic contrast-enhanced (DCE) images to study vasculature (Padhani and Husband 2001), diffusion-weighted (DW) images (de Figueiredo, Borgonovi et al. 2011) for determining tissue architecture, arterial

spin-labeling (ASL) to image cerebral perfusion (Alsop and Detre 1998), and blood-oxygen level dependent (BOLD) (Ogawa, Lee et al. 1990) for measuring the oxygenation status of red blood cells. Molecular imaging with MRI is often performed with the aid of contrast agents that respond to changes in the environment by changing the measured MRI signal. These contrast agents are used to mitigate the inherently lower sensitivity of MRI compared to the other available techniques. Some of these commonly used MRI contrast agents such as gadolinium (Gd) (Caravan, Ellison et al. 1999) or superparamagnetic iron oxide (SPIO) act by shortening the T_1 (longitudinal) or T_2 (transverse) relaxation times of water protons. This causes a change in the signal intensity in the MR images where the contrast agent is present. T_1 or T_2 contrast agents respond to changes in the local microenvironment such as enzymatic activity or changes in concentration of a target molecule (Moats, Fraser et al. 1997, De Leon-Rodriguez, Lubag et al. 2009). A primary goal for these contrast agents is the ability to image change in tissue pH or metabolite levels to observe defects in metabolism (Aime, Botta et al. 2005, Aime, Fedeli et al. 2006). However, there are challenges to utilizing these contrast agents *in vivo* due to low specificity and some concerns about use of these agents in patients with impaired renal function – an important consideration in patient populations with impaired metabolic function due to disease such as diabetes. Recent reports also suggest that Gd from these agents is retained in tissues for several months, the consequences of which are under investigation (Rogosnitzky and Branch 2016). Furthermore, the behavior of some of these agents at the higher-strength fields (>3T), i.e., decreased relaxivity

effects, precludes more widespread use (Terreno, Delli Castelli et al. 2010, Viswanathan, Kovacs et al. 2010).

In an effort to overcome some of the sensitivity limitations of the above techniques, a hyperpolarized magnetic resonance spectroscopy (MRS) technique has been developed to enhance the signal-to-noise (SNR) by ~10,000-fold (Albert, Cates et al. 1994, Middleton, Black et al. 1995, Navon, Song et al. 1996, Golman, in't Zandt et al. 2006). With this technique, the distribution of spin is artificially altered, creating a larger difference in the spin states (anti-parallel vs. parallel). Essentially, this enhances the sensitivity by greatly increasing the polarization of the spins compared to the thermal equilibrium state. Typically, the ^{13}C labeled compound (e.g., pyruvate) is mixed with a free radical, the mixture is frozen to liquid helium temperature, and then the electron spin states of the free radical are saturated by microwave irradiation. The saturated magnetization is then transferred to the ^{13}C pyruvate spins through dipolar relaxation (Maly, Debelouchina et al. 2008). The magnetization of ^{13}C pyruvate is enhanced by two effects: (i) since the electron spin magnetic moment is 1000 times higher than that of nuclear spin, ^{13}C polarization is enhanced a thousand-fold, and (ii) the liquid helium temperature further enhances the magnetization by a factor of 10. This technique can be used to track molecules labeled with ^{13}C, which is otherwise difficult to measure due to its low natural abundance. Biochemical processes such as glycolysis can be studied *in vivo* with hyperpolarization by labeling important intermediates like pyruvate. To date, hyperpolarized ^{13}C MRS has proved an extremely useful technique for studying cancer metabolism (Golman, in't Zandt et al. 2006, Day, Kettunen et al. 2007, Kennedy,

Kettunen et al. 2012, Nelson, Kurhanewicz et al. 2013). Typically, the method used to create this hyperpolarization is a process called dynamic nuclear polarization (DNP) (Chen, Albers et al. 2007, Comment, van den Brandt et al. 2007). Since the hyperpolarization (of ^{13}C-labeled pyruvate) created by this method only lasts for approximately as long as the T_1 of ^{13}C pyruvate (~20-30s), there is a short window of time in which measurements can be made. Therefore, this technique can only be used to probe fast kinetics *in vivo*.

This thesis will focus on chemical exchange saturation transfer (CEST) contrast agents (Ward, Aletras et al. 2000, Sherry and Woods 2008, van Zijl and Yadav 2011), specifically, endogenous metabolites that exist at physiological concentrations suitable for *in vivo* imaging. The first part of this chapter will describe the CEST theory and current uses. The remainder of this chapter will provide motivation for further development of CEST for studying metabolism *in vivo* and a review of the mitochondrial function and structure that underlies many metabolic processes. In Chapter 2, we will focus on metabolism in skeletal muscle, the currently used "gold-standard" spectroscopy technique, and then the development of a specific CEST biomarker, creatine (Haris, Nanga et al. 2012), and its initial *in vivo* applications to skeletal muscle metabolism in healthy subjects (Kogan, Haris et al. 2013, Kogan, Haris et al. 2013) followed by a pilot reproducibility study (DeBrosse, Nanga et al. 2016).

Chapter 3 will discuss the efforts made toward the application of the creatine CEST technique to study impaired metabolism in a patient population with known mitochondrial dysfunction (DeBrosse, Nanga et al. 2016). Chapter 4 will focus on a new

CEST biomarker, lactate, which was developed as part of this thesis work and validated in skeletal muscle and in a tumor model (DeBrosse, Nanga et al. 2016). Finally, we will summarize and discuss some future directions for these two CEST techniques.

Ultimately the goal for this thesis is to explore the following questions:

I. What are the available CEST biomarkers for monitoring metabolism *in vivo*?

II. Can we develop and apply those techniques to disease states and identify impaired metabolism?

1.2 Chemical Exchange Saturation Transfer

1.2.1 CEST theory

Chemical exchange saturation transfer (CEST) experiments are performed on solute protons that are in exchange with protons of a solvent. In the CEST experiments presented in this dissertation the solutes are metabolites with exchangeable protons (such as creatine in Chapters 2 and 3, and lactate in Chapter 4) and the solvent is water, either phosphate-buffered saline solutions in phantom experiments, or the bulk water in mammalian tissue.

CEST theory is typically described using a generalized case in which there are two nuclear spin systems (spin ½), where W represents the bulk water protons, and S represents the solute protons (**Figure 1.1**) (Forsen and Hoffman 1963, Ward, Aletras et al. 2000). The protons in these systems must be in exchange with one another and have a distinct chemical shift difference which is denoted by $\Delta\omega$. First, we irradiate the protons of S with a frequency-selective radiofrequency (RF) pulse (Wolff and Balaban 1990,

Ward, Aletras et al. 2000). The pulse is designed to "saturate" the magnetization of the protons of S. This means that in the presence of a static magnetic field, when the RF pulse is applied, the population of the two spin states of S will be equalized, i.e., the number of spins aligned *with* the field is equal to the number of spins aligned *against* the field. The result is saturated magnetization of the S protons; in other words, we would observe zero MR signal from those saturated protons. Because the spins of S are exchanging with the spins of W, the saturated magnetization of the S protons is transferred to W protons. During the same time, the W spins are transferred to S, where they are saturated again. This process continues during the entire period of the saturation pulse—typically a few hundred milliseconds to several seconds. The signal of W, which we measure with MRI, is therefore reduced in proportion to the concentration of the exchangeable protons of S. As longitudinal relaxation occurs, both spin systems are returned to equilibrium values as the system approaches steady state (van Zijl and Yadav 2011, Cai, Haris et al. 2012).

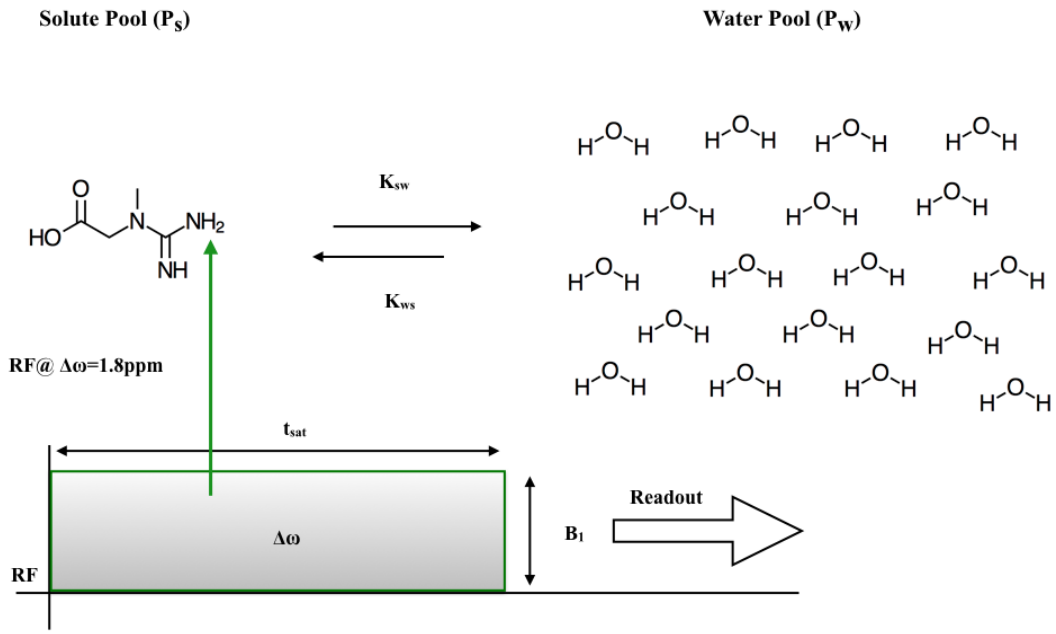

Figure 1.1 CEST theory diagram. An irradiation radiofrequency (RF) pulse is used to selectively saturate the protons of a solute that contains exchangeable protons at some chemical shift Δω. Here, an example is shown using the amine protons of creatine. The solute protons exchange with the solvent protons, typically those of surrounding bulk water. *(Adapted from Liu et al. (Liu, Song et al. 2013)).*

The magnetization of the water and solute protons is described by the Bloch-McConnell equations, modified for chemical exchange (Abergel and Palmer 2004). If we apply the RF pulse along the x-direction, the Bloch-McConnell equations for the water protons are given by **Equations 1.1-1.3**, and the equations for the solute protons are given by **Equations 1.4-1.6** (see **Table 1-1**). Even using the simple two-site exchange model, it is difficult to (analytically) solve the full Bloch-McConnell equations that describe the magnetization (X, Y, and Z) of the entire system. We can make some simplifying assumptions that reduce the Bloch-McConnell equations to the Y and Z magnetization

components. First, we assume that the populations of S and W are asymmetric, with the solvent pool being much greater than the solute pool. The equilibrium magnetization (M_0) for the water is therefore much greater than that of the solute: $M_{0W} >> M_{0S}$. We also assume that we will only be saturating the solute pool S. As described in Zhou et al., it is simpler to re-write the equations by first defining **Equations 1.7-1.12**, which leaves us with the simplified equations for the water magnetization **Equations 1.13 and 1.14**, and for the solute proton magnetization **Equations 1.15 and 1.16**.

Then we assume that both systems reach a steady state (SS), which would require that all left-hand sides of **Equations 1.13-1.16** are zero. Solving the equations with that assumption yields the z-axis magnetization for the water protons (**Equation 1.17**). We can also define the saturation efficiency, α or the amount of pool S that was saturated by the RF pulse (**Equations 1.20 and 1.21**), from which it is apparent that we would only fully saturate S if we use a very strong RF pulse, i.e., $\omega_1 \rightarrow \infty$ so that $\alpha=1$.

For practical purposes, we will consider the effects of a weak pulse, where $M_{zW}(t_0)=M_{0W}$ and $m_{zW}(t_0)=0$, and so the magnetization of the water protons is given by **Equation 1.22**, where the water pool approaches steady-state at a rate r_{1W} (**Equation 1.23**), which defines the spin-lattice relaxation rate of the water protons while the RF pulse is applied to the solute protons. The proton transfer ratio (PTR) is given in **Equation 1.24** in which the applied RF saturation time is $t_{sat}=t-t_0$. The analytical derivation only applies in the steady-state condition with a two-pool exchange model (Zhou, Wilson et al. 2004, Woessner, Zhang et al. 2005, McMahon, Gilad et al. 2006, van Zijl, Jones et al. 2007). We use non-steady-state experimental conditions and use a numerical analysis of the full

Bloch-McConnell equations for experimental analysis (McConnell 1958). More in-depth theoretical considerations of CEST are available in several reviews (Zhou and van Zijl 2006, Sherry and Woods 2008).

1.2.2 Calculation of the CEST effect

The saturated, transferred magnetization from solute pool to water pool is imaged to detect the "CEST effect". We can visualize the CEST effect by plotting the water signal as a function of saturation frequency, producing a "z-spectrum". In order to observe the signal from saturation of a particular metabolite, we calculate the CEST asymmetry ratio by subtracting the magnetization signal obtained while saturating the exchangeable solute proton chemical shift, defined as $M_{sat(+\Delta\omega)}$, from the magnetization signal obtained while saturating at the same chemical shift on the opposite side of the water peak, defined as $M_{sat(-\Delta\omega)}$. The CEST asymmetry is defined by **Equations 1.25 and 1.26**. This asymmetry analysis, normalized with the magnetization signal (M_0) observed when saturating very far away from water (>20ppm), elucidates the CEST effect from the solute protons. When implementing CEST *in vivo* in biological tissues, we must consider the effects of direct saturation (DS), also called "spillover" (Sun, Wang et al. 2014) in which the irradiating pulse applied to the solute protons also ends up saturating the water protons. Any accidental saturation of the water peak would confound the CEST signal, so the asymmetry calculation is performed to subtract out those effects. Additionally, the effect of magnetization transfer (MT) can also affect the measured CEST signal (Leibfritz and Dreher 2001) (**Figure 1.2**). MT is a well-studied NMR phenomenon (Bryant 1996) in which irradiation of a frequency far from the water resonance leads to transfer of

saturated magnetization from immobilized macromolecules or exchangeable side-chain protons to the bulk water. Unlike CEST, MT depends on both chemical exchange and cross-relaxation (Zhou and van Zijl 2006). Since the MT and DS are largely symmetric around the water resonance, the asymmetry analysis described above helps to mitigate the effects of DS and MT in biological tissues (Cai, Haris et al. 2012).

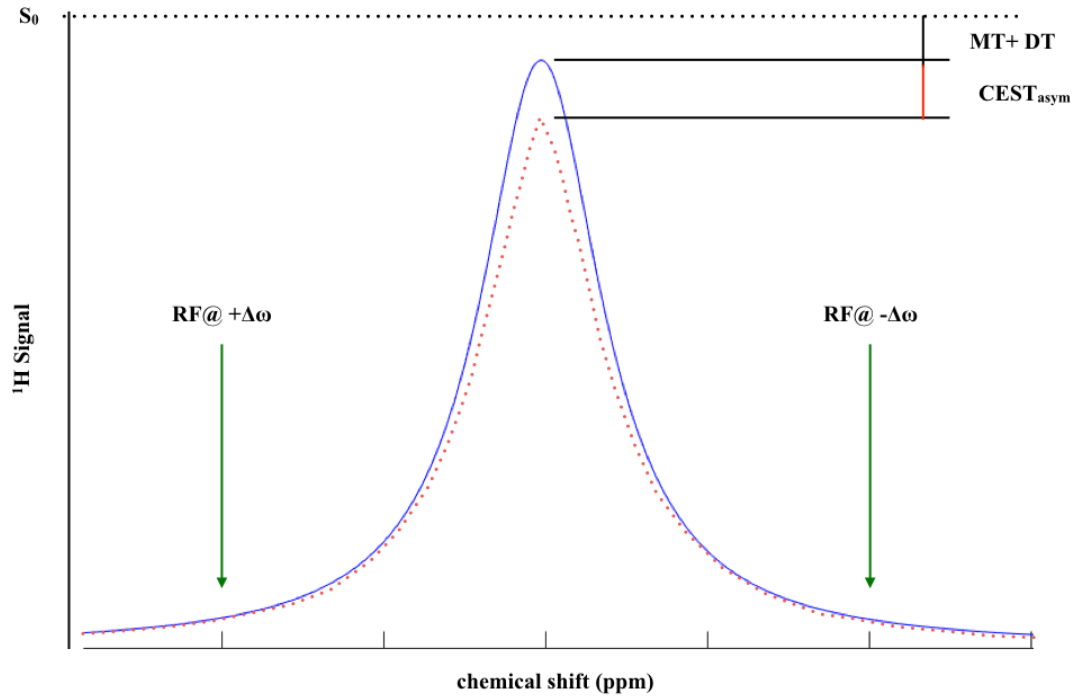

Figure 1.2 The CEST effect. When the selective RF pulse is applied to solute protons at their specific resonance, they exchange their saturated magnetization with the bulk water protons (shown by the decreased signal height in the red line). The resultant signal is decreased compared to that acquired with no saturation. Applying a pulse on the symmetric side of the bulk water peak allows for calculation of the CEST asymmetry, in order to mitigate the effects of direct saturation and magnetization-transfer (adapted from (Zhou and van Zijl 2006)).

In phantom experiments where the transverse relaxation time of water (T_2) is long, normalization with M_0 is sufficient, as there is not usually much DS. In many biological tissues, such as muscle, that have short water T_2 (Stanisz, Odrobina et al. 2005) the CEST experiments require high saturation pulse amplitudes, which leads to increased DS. This is not entirely alleviated by simply normalizing with M_0; rather, for *in vivo* experiments we often calculate the CEST effect by normalizing with $M_{sat(-\Delta\omega)}$ instead (Liu, Gilad et al. 2010) (Equation 1.27).

Although this calculation is straightforward, in practical applications of CEST imaging we must also consider the effects of B_0 (static field) and B_1 (applied pulse) variations across the tissue. Due to the asymmetry analysis, any inhomogeneity in the B_0 field will introduce errors in the CEST contrast calculation. In the experiments performed for this dissertation local B_0 fields were always mapped, either with a gradient-echo image or with a Water Saturation Shift Reference (WASSR) image (Kim, Gillen et al. 2009) and used to correct the CEST calculation. Similarly, B_1 variations will also affect the CEST calculation and so B_1 maps and B_1-dependent calibration curves were used to account for that variation in the final CEST calculations (Singh, Cai et al. 2013).

Table 1-1 CEST equations

Equations	
$\frac{dM_{xW}}{dt} = -\Delta\omega_W M_{yW} - R_{2W}M_{xW} + k_{SW}M_{xS} - k_{WS}M_{xW}$	*(1.1)*
$\frac{dM_{yW}}{dt} = \Delta\omega_W M_{xW} - R_{2W}M_{yW} + k_{SW}M_{yS} - k_{WS}M_{yW} + \omega_1 M_{zW}$	*(1.2)*
$\frac{dM_{zW}}{dt} = -\omega_1 M_{yW} - \square_{1W}(M_{zW} - M_{0W}) + k_{SW}M_{zS} - k_{WS}M_{zW}$	*(1.3)*
$\frac{dM_{xS}}{dt} = -\Delta\omega_S M_{yS} - R_{2S}M_{xS} + k_{WS}M_{xW} - k_{SW}M_{xS}$	*(1.4)*
$\frac{dM_{yS}}{dt} = \Delta\omega_S M_{xS} - R_{2S}M_{yS} + k_{WS}M_{yW} - k_{S\square}M_{yS} + \omega_1 M_{zS}$	*(1.5)*
$\frac{dM_{zS}}{dt} = -\omega_1 M_{yS} - R_{1S}(M_{zS} - M_{0S}) + k_{WS}M_{zW} - k_{SW}M_{zS}$	*(1.6)*
$m_{zW} = M_{zW} - M_{0W}$	*(1.7)*
$m_{zS} = M_{zS} - M_{0S}$	*(1.8)*
$r_{1W} = R_{1W} + k_{WS}$	*(1.9)*
$r_{1S} = R_{1S} + k_{SW}$	*(1.10)*
$r_{2W} = R_{2W} + k_{WS}$	*(1.11)*
$r_{2S} = R_{2S} + k_{SW}$	*(1.12)*
$\frac{dM_{yW}}{dt} = -r_{2W}M_{yW} + k_{SW}M_yS$	*(1.13)*
$\frac{dM_{zW}}{dt} = -r_{1W}m_{zW} + k_{SW}m_{zS}$	*(1.14)*
$\frac{dM_{yS}}{dt} = \omega_1 m_{zS} - r_{2S}M_{yW} + \omega_1 M_{0S}$	*(1.15)*
$\frac{dm_{zS}}{dt} = -\omega_1 M_{yS} - r_{1S}m_{zS} + k_{WS}m_{zW}$	*(1.16)*
$SSm_{zW} = -\frac{k_{SW}}{r_{1W}}\left(\frac{M_{0S}\omega_1^2}{(\omega_1^2 + pq)}\right)$	*(1.17)*
$p = r_{2S} - \frac{k_{SW}k_{WS}}{r_{2W}}$	*(1.18)*
$q = r_{1S} - \frac{k_{SW}k_{WS}}{r_{1W}}$	*(1.19)*

Equations	
$\alpha = \frac{-m_{zS}^{SS}}{M_{0S}}$	*(1.20)*
$\alpha = \frac{\omega_1^2}{\omega_1^2 + pq}$	*(1.21)*
$m_{zW}(t) = \frac{k_{SW} m_{zS}^{SS}}{r_{1W}}\left[1 - e^{-r_{1W}(t-t_0)}\right]$	*(1.22)*
$r_{1W} = R_{1W} + k_{WS}$	*(1.23)*
$PTR = \frac{M_{0W} - M_{zW}(t_{sat})}{M_{0W}} = \frac{k_{sW}\alpha M_{0S}}{(R_{1W} + k_{WS})M_{0W}}\left[1 - e^{-(R_1 + k_{WS})t_{sat}}\right]$	*(1.24)*
$CEST_{asym}(\Delta\omega) = \frac{M_{sat\,(-\Delta\omega)} - M_{sat(+\Delta\omega)}}{M_0}$	*(1.25)*
$CEST_{as\square m}(\Delta\omega) = \frac{\alpha k_{SW} M_{0S}}{(R_{1w} + k_{WS})M_{0W}}[1 - e^{-(R_{1W} + k_{WS})t_{sat}}]$	*(1.26)*
$CEST_{asym}(\Delta\omega) = \frac{M_{sat}(-\Delta\omega) - M_{sat}(+\Delta\omega)}{M_{sat}(-\Delta\omega)}$	*(1.27)*

$\omega_0 = \gamma B_0$ (main magnetic field)
$\omega_1 = \gamma B_1$ (applied RF field)
$\Delta\omega = \omega - \omega_0$
R_1 = spin-lattice relaxation rate ($1/T_1$)
R_2 = spin-spin relaxation rate ($1/T_2$)
M_0 = equilibrium magnetization
k_{SW} = exchange rate for protons from pool S to pool W
k_{WS} = exchange rate for protons from pool W to pool S

1.2.3 CEST optimization

The CEST contrast is dependent on several factors including exchange rate, saturation pulse parameters, and relaxation times (van Zijl and Yadav 2011). Detection of the CEST effect necessitates that the solute protons fall in the slow-intermediate exchange regime (**$k \leq \Delta\omega$**) where Δω is the chemical shift between water and solute protons (Ward, Aletras et al. 2000). Faster exchange rates where k>Δω lead to coalescence, where the solute peak cannot be resolved from the water peak. This affects the CEST measurement: when

the saturation pulse is applied, nearby spins will also be saturated along with the targeted solute protons.

Due to the above requirements, the strength of the static magnetic field (B_0) is also an important consideration for CEST experiments. At higher field strengths, the chemical shift $\Delta\omega$ between solute protons and water protons is increased. This allows for CEST imaging of molecules with faster exchange rates to be imaged at higher fields ($\geq$3T) where the condition $k \leq \Delta\omega$ is satisfied (Kogan, Hariharan et al. 2013).

Optimal saturation parameters must be determined for each individual CEST target. While the saturation pulse needs to be strong to fully saturate the solute protons, if it is too strong, spillover effects will contaminate the signal. When determining the optimal parameters for specific CEST experiments, we typically titrate combinations of B_1 (pulse strength) and saturation duration (time the pulse is left on), until the maximum CEST asymmetry can be obtained with minimal spillover effects. As we would anticipate, the exchange rate affects the optimal saturation parameters. If the exchange rate is slow, maximum CEST signal can be obtained by using a low power pulse, applied for a long duration in order to reach steady state. If the exchange rate is fast, a higher pulse power will be required to achieve sufficient saturation, and subsequently the pulse can be much shorter in duration (Kogan, Hariharan et al. 2013).

1.2.4 CEST of endogenous metabolites

As with the other techniques described in Section 1.1, the goal for CEST imaging is to identify "bioresponsive" agents that provide non-invasive measures of biochemical processes *in vivo*. There are exogenous agents that have been developed for CEST

imaging, such as paramagnetic CEST (PARACEST) agents that create large Δω, permitting selective saturation of molecules with fast exchange rates (Zhang, Merritt et al. 2003, Woessner, Zhang et al. 2005, Zhang, Malloy et al. 2005, Woods, Donald et al. 2006). PARACEST agents provide information on processes like enzymatic activity or redox state changes, which change the properties of exchangeable protons and, by extension, the CEST signal (Zhang, Merritt et al. 2003, Aime, Carrera et al. 2005, Woods, Donald et al. 2006, Yoo and Pagel 2006, Pikkemaat, Wegh et al. 2007, Yoo, Raam et al. 2007, Chauvin, Durand et al. 2008, Viswanathan, Ratnakar et al. 2009). Although these exogenous agents are useful, like the other contrast agents described in the introduction, they must be injected into the subject for *in vivo* imaging. This is undesirable for many reasons, including invasiveness, cost, and concern with possible organ toxicity.

The goal for this dissertation was to further identify and develop *endogenous* CEST agents, primarily to avoid the complications that arise when injecting exogenous agents. To date, several types of endogenous metabolites have been imaged using CEST. In order to image an endogenous metabolite with CEST, it must exist at a high concentration (mM) in addition to having the optimal exchange conditions and chemical shift as described above. It must also contain exchangeable protons. Typically, these are amide (-NH), amine (-NH2), or hydroxyl (-OH) protons (Zhou, Blakeley et al. 2008, Haris, Cai et al. 2011, Jia, Abaza et al. 2011, Singh, Haris et al. 2012, Klomp, Dula et al. 2013, Yadav, Xu et al. 2014). These protons on various metabolites have been imaged with CEST to study cancer, neurological disorders, and muscle energetics.

Amide CEST, or amide proton transfer (APT) imaging has proven useful in imaging of tumors that contain a high concentration of mobile macromolecular protons (Zhou, Lal et al. 2003). APT imaging provides a means of measuring changes in concentration of cytosolic proteins due to the CEST contrast from the slow-exchanging amide protons of peptide backbones. It also reports on the tissue pH, which is decreased in some tumor types and in ischemic tissue. The chemical exchange rate is highly dependent on tissue pH and so a change in the APT signal is observed when the pH is decreased (Zhou, Payen et al. 2003, Zhou, Blakeley et al. 2008, Jia, Abaza et al. 2011). However, when both pH and mobile macromolecular proton content changes, it is difficult to assess the individual contributions to APT.

In our effort to further develop CEST for study of cellular metabolism, we have chosen to focus on small metabolites. Metabolite levels are involved in cellular regulation of metabolism (Zimmerman 2005). Although overall cellular metabolic pathways are complex, they share common metabolites that are highly regulated to maintain proper cellular function (Metallo and Vander Heiden 2013). In turn, local concentrations of metabolites provide short-term regulation of enzymatic activity (Wegner, Meiser et al. 2015). The goal of our utilization of the CEST technique is to image metabolites that are altered in a way that is reflective of disruptions in metabolism, thus providing another tool for probing metabolic diseases.

There have been several recent publications on imaging of small metabolites from the Reddy lab (Haris, Cai et al. 2011, Haris, Singh et al. 2013). Amine protons of glutamate have been imaged with CEST (Cai, Haris et al. 2012, Kogan, Singh et al. 2013) (**Figure**

1.3) and validated by NMR spectroscopy. With glutamate CEST (GluCEST), the variation in glutamate between gray and white matter in healthy human brain is clearly visible.

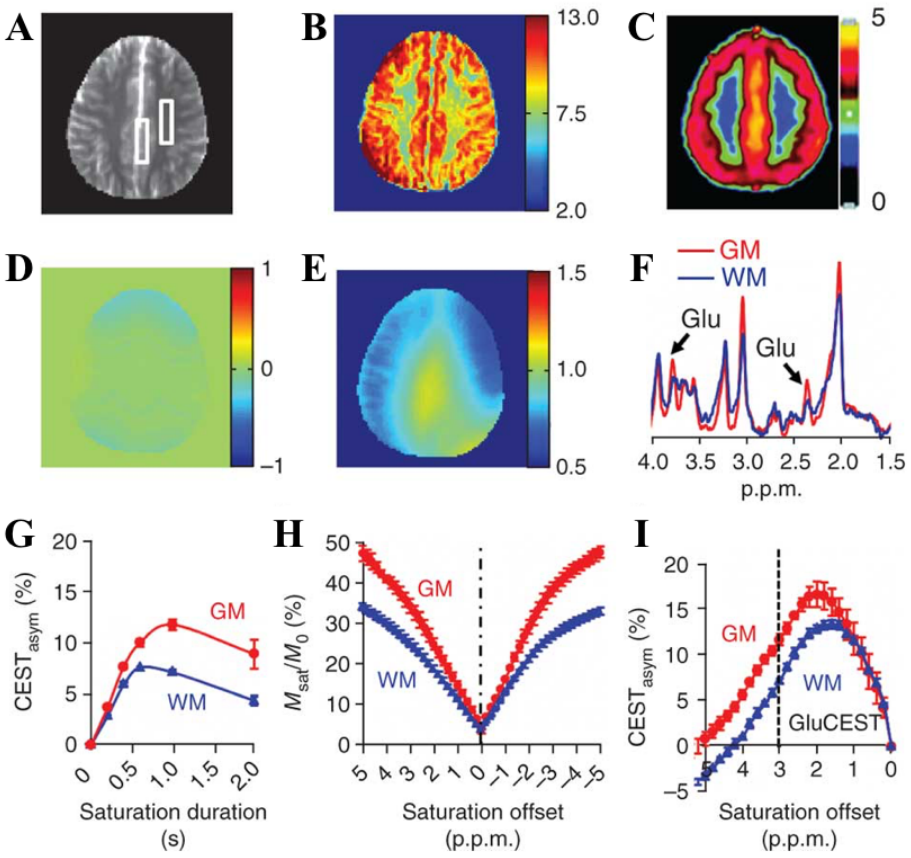

Figure 1.3 GluCEST imaging and ^{1}H MRS from a healthy human brain acquired at 7T. A) anatomic proton image of an axial slice in human brain, showing the two voxel locations where spectroscopic data was acquired separately in the gray and white matter; B) B_1 and B_0 corrected GluCEST contrast map; C) map of distribution volumes (DVs) of metabotropic Glu receptor subtype 5 from a PET image *(Reprinted by permission of the Society of Nuclear Medicine: J Nucl Med* [31], Figure 2, copyright (2007)). The GluCEST map and the PET image show similar distribution pattern of Glu in brain, which is higher in GM compared to WM; D) B_0 map and E) B_1 map corresponding to the slice in A), and used to correct the final CEST map for field inhomogeneity; F) ^{1}H MRS spectra obtained from the voxels of gray matter and white matter in A). These spectra show higher amplitude of Glu $–CH_2$ resonance (at 2.3 ppm.) and –CH resonance (at 3.75 ppm) in gray matter; G) saturation pulse duration dependence of GluCEST data from human brain. H,I) z-spectra and corresponding asymmetry plots from human gray matter and white matter regions. The GluCEST peak at 3 ppm is ~11% from gray matter and ~7% from white matter. (*Reprinted with permission (Cai, Haris et al. 2012).)*

GluCEST has also been used to study brain neurotransmitter alterations in an Alzheimer's disease (Alz) mouse model (**Figure 1.4**) (Haris, Nath et al. 2013, Crescenzi, DeBrosse et al. 2014) and 1-methyl-4-phenyl-1,2,3,6-tetrahydropyridine (MPTP)-based model of Parkinson's (Bagga, Crescenzi et al. 2016). We also implemented the GluCEST technique in a longitudinal study, demonstrating the ability of the technique for measuring changes in GluCEST within a cohort of Alz mice over time (Crescenzi, DeBrosse et al. 2017). These studies have shown progressive loss of glutamate associated with neurodegenerative disease due to metabolic dysfunction. This has also provided some exciting evidence to support the concept of glutamate excitotoxicity in neurodegenerative diseases (Bagga, Crescenzi et al. 2016). Glutamate CEST (GluCEST) has also been used to study neuropsychiatric disorders such as epilepsy (Davis, Nanga et al. 2015) and schizophrenia (Roalf, Nanga et al. 2017). Overall, GluCEST has promise as a biomarker for metabolic changes, especially in neuropathologies.

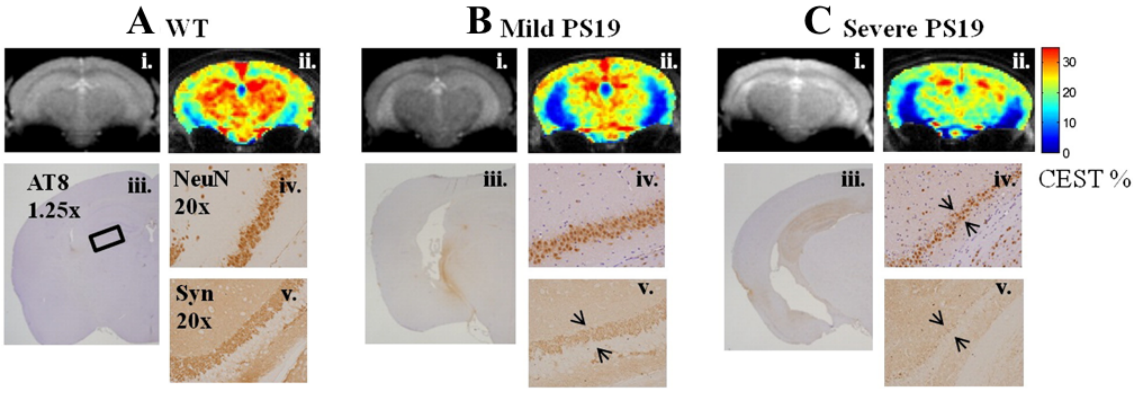

Figure 1.4 4 GluCEST maps and corresponding immunohistochemistry (IHC). A–C i) anatomical, coronal-slice images in a mouse brain corresponding to the GluCEST slice through the mid-hippocampus. A–C ii) GluCEST maps in a wild-type and in a progressive tauopathy model of Alzheimer's (PS19) mice reveal lower glutamate levels throughout the brain of tauopathy mice, which continues to decrease with disease

severity. A–C iii) The corresponding immunohistochemistry in the same slices of post-mortem brain tissue stained for hyper-phosphorylated tau (AT8) reveal varying severity of pathological tau protein within the PS19 cohort and show progressive loss of synapses. (Neuron staining (NeuN) and synapse staining (Syn) were both performed on the ex vivo tissue.) This is a clear example of the utility of the CEST method: imaging correlated to a standard technique provides more detailed insight into the biochemical pathways during the progression of disease.

In this work, we focused on CEST imaging of the amine protons of creatine to study oxidative phosphorylation (OXPHOS) and the hydroxyl protons of lactate to study glycolysis, which will be the subject of the following chapters. As discussed above, compared to classic spectroscopic methods for measuring metabolites *in vivo*, CEST has much higher spatial resolution (van Zijl and Yadav 2011). This is particularly beneficial for studying metabolic disruption, for example, in tumors that have heterogeneous tissue, or in skeletal muscle where specific muscle fiber types may be affected.

1.3 Metabolic Dysfunction

Metabolic disease is characterized by dysfunctional energy metabolism and underlies conditions such as obesity and hypertension, and diseases including: cancer, neuromuscular disorders, diabetes, primary mitochondrial diseases, and cardiovascular disease (Lin, Wu et al. 2004). Mammalian cells use both glycolytic and mitochondrial metabolism. In healthy tissue, in the presence of oxygen, cells typically metabolize glucose to carbon dioxide via the tricarboxylic acid (TCA) cycle in the mitochondria (**Figure 1.5**).

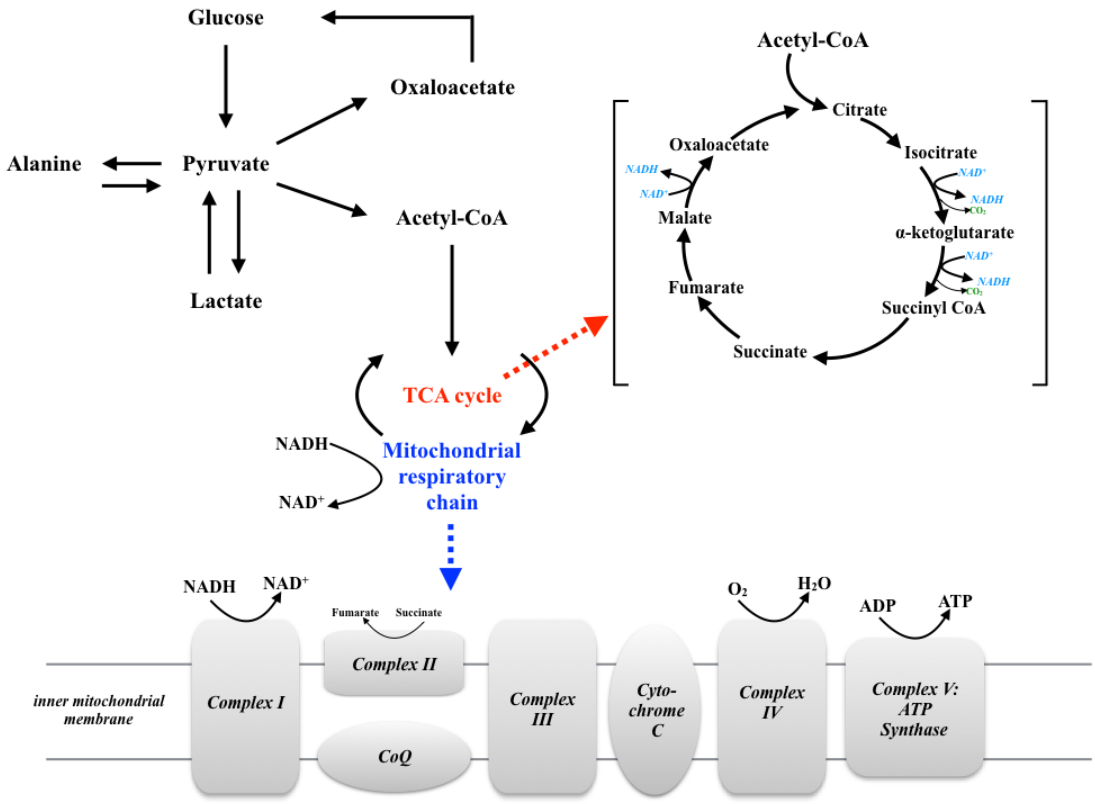

Figure 1.5 Summary of key metabolic pathways. Tricarboxylic acid (TCA) cycle and the mitochondrial respiratory chain *(adapted from Adeva et al.(Adeva, Gonzalez-Lucan et al. 2013)).*

The result of glucose metabolism is production of nicotinamide adenine dinucleotide (NADH), the electron donor for OXPHOS, which ultimately generates the adenosine triphosphate (ATP) necessary for cellular function (Alberts, Johnson et al. 2008). By this process, ~36 molecules of ATP are produced for every molecule of glucose. If sufficient oxygen is not available, cells will still metabolize glucose through anaerobic glycolysis, generating lactate and producing 2 molecules of ATP for every molecule of glucose (Adeva, Gonzalez-Lucan et al. 2013). One of the most widely studied metabolic

alterations is the “Warburg effect” in cancer cells (Warburg 1956). Unlike the scenario for healthy tissue, cancer tissue converts the majority of consumed glucose into lactate even in the presence of sufficient oxygen (Warburg 1956). This is also called “aerobic glycolysis” (Wang, Marquardt et al. 1976) and much research is still underway to determine exactly why cancer cells preferentially use it over the pathways used by healthy tissue. The altered metabolic state of cancer cells begs an interesting question – why would cells undergo aerobic glycolysis when, from an energy standpoint, it is much more efficient to produce ATP by means of oxidative phosphorylation (DeBerardinis, Sayed et al. 2008). In proliferating cells (like cancer cells), there is a continuous supply of glucose obtained from the bloodstream. As they continue to proliferate, although they do require ATP for energy, cancer cells have a demand to build up necessary cellular components, such as lipids, amino acids, fatty acids, etc., or the “biomass” of new cells (Pizer, Wood et al. 1996, Rashid, Pizer et al. 1997). Essentially, cancer cells need to use the glucose carbon source for anabolic processes at a higher demand than the need to generate ATP by catabolic processes. The answer to this question – why do cancer cells preferentially utilize aerobic glycolysis? – is complex, involving both oncogenic and metabolic reprogramming, and far outside the scope of this thesis work, but has been explored in many reviews (DeBerardinis, Lum et al. 2008, Hsu and Sabatini 2008, Heiden, Cantley et al. 2009, Hanahan and Weinberg 2011, Carrer and Wellen 2015, Hirschey, DeBerardinis et al. 2015, DeBerardinis and Chandel 2016). We will focus on one aspect, excess production of lactate by cancer cells, which provided the motivation to develop lactate CEST imaging and is the subject of Chapter 4.

Altered metabolism affects many biological processes in cancer cells such as signaling, growth suppressors, and apoptosis, and the exact metabolic changes that drive cancer cell reprogramming are incredibly challenging to identify. Recently, it has been suggested that study of so-called "inborn errors of metabolism" (IEM) may help to elucidate individual aspects driving cancer cell metabolism (Erez, Shchelochkov et al. 2011). IEM are due to genetic defects that lead to disruption of a single metabolic pathway (Dipple and McCabe 2000, Pampols 2010). The complexities of the overall metabolic network can begin to be simplified by identifying an IEM and observing all of the metabolic consequences (Erez and DeBerardinis 2015). This has strong implications for cancer as well as other metabolic diseases. We will discuss some IEM in Chapter 3 in context of CEST imaging of creatine to study muscle metabolism.

The rest of this introductory chapter will focus on the metabolic pathways of glycolysis and OXPHOS with emphasis on the latter, which occurs in mitochondria. Mitochondrial structure and function can be affected in metabolic disorders. Mitochondrial processes help regulate an array of other biological processes. In addition to cellular respiration, they are responsible for generation of reactive oxygen species (ROS), maintaining redox status, and calcium homeostasis (Venditti, Di Stefano et al. 2013). Therefore, mitochondrial function is indicative of health of individual cells, as well as whole-body metabolic state. In recent decades our understanding of the mitochondrion has evolved from the basic description ("mitochondria make ATP for energy") as we've realized the complex and ubiquitous role it seems to play in almost every medical discipline (Picard, Wallace et al. 2016). Mitochondrial dysfunction is observed in cancer, in skeletal muscle

in type 2 diabetes, and in cardiovascular disease (Wallace 1989, Wallace 1992, Mecocci, Macgarvey et al. 1993, Ballinger, Shoffner et al. 1994, Wallace 2005), which necessitates the study of mitochondrial function noninvasively and *in vivo*.

In Chapter 2, we will describe how the CEST technique has been applied to observe mitochondrial function in healthy skeletal muscle. As the importance of the mitochondria in many disease states has become increasingly evident across multiple disciplines, the past few decades have seen an enormous amount of literature about mitochondrial DNA (mtDNA) mutations. In the 1980s, it was discovered that mtDNA, inherited maternally, could be the culprit in human disease due to point mutations or deletions(Giles, Blanc et al. 1980, Wallace 1992). Although a complete description of mtDNA defects is not the focus of this work, the effects are far-reaching into neurology, endocrinology, oncology, immunology, etc. Chapter 3 of this dissertation will discuss a small, heterogeneous group of mitochondrial impairments and our application of CEST for assessing impaired mitochondrial function in skeletal muscle. The next section summarizes the function of the mitochondrion and the process of OXPHOS.

1.4 Mitochondria and Oxidative Phosphorylation

The mitochondrion was essential for the evolution of present-day eukaryotic cells (Gray, Burger et al. 1999) by providing a method for metabolism of sugars in order to produce energy. Mitochondria are large (0.5-1μm) organelles within the cytoplasmic space of cells (Alberts, Johnson et al. 2008), and have a wide range of functions, depending on the cell type requirement. Different cell types also contain specific numbers of mitochondria, depending on their particular energy demands (Szewczyk and Wojtczak 2002). Tissues

that are very metabolically active, such as brain, liver, cardiac, and skeletal muscle, contain the highest number of mitochondria. Although this work will primarily focus on their function in skeletal muscle, mitochondria are also the center of ion homeostasis and other biochemical pathways (Pagliarini, Calvo et al. 2008). In the 1950s, Britton Chance and others (Lardy and Wellman 1952, Low, Siekevitz et al. 1958, Mitchell and Moyle 1967) identified and described the mitochondrial respiratory chain and the process of OXPHOS, by which mitochondria generate ~80-90% of their ATP (Chance and Williams 1956). Mitochondria use the products of the TCA cycle and fats derived from diet to produce ATP and heat. OXPHOS measurement in human mitochondria using CEST will be the focus of the next two chapters.

1.4.1 Mitochondrial structure

The structure of the mitochondrion contains two membranes, outer and inner, that perform two distinct functions (Alberts, Johnson et al. 2008). These membranes create two compartments within the mitochondrion: the matrix, and the intermembrane space. The outer membrane is permeable to molecules and small proteins that are < 5000 daltons. This permeability is due to the transport proteins, called porins, which form channels through the lipid bilayer. Molecules that pass through the outer membrane can enter the intermembrane space, but the inner membrane prevents them from entering into the matrix. The matrix contains the "major working part" of the mitochondria, which means that only highly specific molecules are permitted to pass through the inner membrane. The inner membrane is highly selective due to its unique lipid bilayer, which is made up of cardiolipin (a double phospholipid) that contains four fatty acids. Because

the matrix is where key metabolic processes take place, it contains many mitochondrial enzymes that require specific small molecules for metabolism. The inner membrane allows those small molecules to enter the matrix through specialized transport proteins.

Some of the most important processes that occur in the matrix are metabolism of pyruvate and fatty acids, producing acetyl coenzyme-A (CoA), which is then oxidized in the TCA cycle. When acetyl CoA is oxidized, carbon dioxide (CO_2) is produced and leaves the cell as a waste product. More importantly, this oxidation of CoA is the first step in generating the high-energy electrons that enter the electron-transport chain, which is referred to in mitochondria as the respiratory chain. These products of the TCA cycle, NADH and flavin adenine dinucleotide ($FADH_2$), carry the high-energy electrons to the inner membrane where they enter the respiratory chain (Alberts, Johnson et al. 2008). The respiratory chain is composed of enzymes that facilitate the process of OXPHOS, which generates most of the ATP required by the cell.

1.4.2 Respiratory chain components

The respiratory chain (RC) is composed of five key enzyme complexes (I-V) that are imbedded within the inner membrane (Hatefi 1985). Electrons are donated from NADH and $FADH_2$ and flow through the complexes. As mentioned previously, NADH is generated in the matrix and electron transport in the respiratory chain begins with reoxidizing NADH by removing a hydride ion (2 electrons) to regenerate NAD^+ (**Equation 1.28**).

These two electrons are passed to the first of many electron carriers in the RC. They start with very high energy, which is gradually lost as the electrons are passed along the chain

(Alberts, Johnson et al. 2008). Essentially, the electrons pass along metal ions bound to proteins, altering the electron affinity of the metal ions. The proteins are grouped into the RC enzyme complexes that are held in the inner mitochondrial membrane by transmembrane proteins. The complexes have increasing levels of affinity for electrons, which are passed along each complex until they are transferred to oxygen, which has the highest affinity. This complicated process of electron transfer exists in cells in order to avoid the huge free-energy drop of simply transferring the electrons from NADH directly to molecular oxygen (O_2), in which the majority of the energy would be released as heat (Alberts, Johnson et al. 2008). Instead, cells manage to store approximately half of the energy that is released by utilizing the electron transport chain (ETC).

It is important to briefly define some of the other proteins and enzymes that are involved in the RC. Flavoproteins are a polypeptide that contains a flavin adenosine dinucleotide (FAD) or a flavin mononucleotide (FMN) prosthetic group. Flavoproteins can accept or donate electrons as pairs (**Equation 1.29-1.30**) (Karp 2008). Cytochromes are proteins that contain bound heme groups and only facilitate one-electron transfers. They accomplish this by changing the oxidation state of their iron atom from Fe^{3+} to Fe^{2+} when accepting an electron (Karp 2008). There are other iron-sulfur proteins that can carry electrons, and like cytochrome, participate in one-electron transfer. Usually, these contain either two or four iron atoms bound to an equal number of sulfur atoms and to cysteine side-chains. Another important component is Coenzyme Q (CoQ), quinone (Q), or ubiquinone (uq), which is is a small, soluble electron carrier within the lipid bilayer of the

inner membrane (**Equation 1.31**). Bound to these respiratory chain proteins are flavins, and two copper atoms that also carry electrons.

Table 1-2 Electron transfer in mitochondria

Equations	
$H^- \rightarrow H^+ + 2e^-$	*(1.28)*
$FAD + 2e^- + 2H^+ \rightarrow FADH_2$	*(1.29)*
$FMN + 2e^- + 2H^+ \rightarrow FMNH_2$	*(1.30)*
$Q + 2e^- + 2H^+ \rightarrow QH_2$	*(1.31)*
$2O_2^- \cdot + 2H^+ \rightarrow H_2O_2 + O_2$	*(1.32)*
$H_2O_2 + Fe^{2+} \rightarrow Fe^{3+} + OH \cdot + OH^-$	*(1.33)*

The individual complexes contain several electron carriers (**Table 1-3**) (Karp 2008).

1. **Complex I**, known as NADH dehydrogenase (or NADH-coenzyme Q reductase) is the largest complex, containing over 45 polypeptides (Guenebaut, Schlitt et al. 1998). It accepts two electrons from NADH, making it the first link between the products of the TCA cycle / fatty acid oxidation and the respiratory chain. Within Complex I, electrons flow from: NADH→ FMN→ iron-sulfur centers→ ubiquinone→ cytochrome *bc1* complex. The end result is the net transport of protons from the matrix to the intermembrane space, generating a proton-motive force (Grivennikova, Kapustin et al. 2001).
2. **Complex II**, known as succinate dehydrogenase (or succinate-coenzyme Q reductase) (SDH) provides another direct link to the TCA cycle, as it is the only enzyme of the TCA cycle that is also an integral membrane protein. Here, succinate binds and a hydride is transferred to FAD, resulting in electron transfer to iron-sulfur centers before a final transfer to 2 electrons to CoQ: succinate + CoQ → Fumarate + $CoQH_2$. Unlike complex 1, there is no proton-motive force

generated due to the small free energy of the reaction, and only ~1.5ATP are generated per $FADH_2$, contrasted with the 2.5ATP per NADH (Cecchini 2003).

3. **Complex III,** or coenzyme Q reductase, transfers electrons from CoQH2 generated either by Complex I or Complex II to reduce cytochrome c. Complex III functions as a dimer and utilizes a pathway known as the Q-cycle. Briefly, $CoQH_2$ binds to the **Q** site, and then one electron is transferred to an iron-sulfur protein, and then to cytochrome *c1*. This allows 2 protons to be released into the intermembrane space. The second electron is transferred to a heme, generating CoQ, which can diffuse from the **Q** site. This process occurs twice within to complete a Q-cycle, with a net result of two electrons transported to cytochrome c1, and finally to cytochrome c (Karp 2008).
4. **Complex IV,** or cytochrome c reductase, transfers electrons, one at a time, from cytochrome c, which are passed (four at a time) to reduce molecular oxygen into water. This is a key point: that the cell can use O_2 for respiration because this complex holds onto molecular oxygen at a special bimetallic center until it picks up four electrons, and can be safely released while avoiding the generation of superoxide radicals ($O_2^- \cdot$). This reaction accounts for ~90% of total oxygen uptake in most cells, and is vital for aerobic respiration (Alberts, Johnson et al. 2008).
5. **Complex V or ATP synthase** is composed of two principle sectors, F1 and F0. It has a ring of six subunits that project out onto the matrix side of the inner membrane. This ring is held in place by an "arm" that connects it to a group of

transmembrane proteins that form a "stator" within the membrane. This piece is in contact with the "rotor"—a ring of 10-14 transmembrane protein subunits (Abrahams, Leslie et al. 1994).

Table 1-3 Properties of the components of the mitochondrial respiratory chain

Complex	Mass (kD)	# subunits	Substrate binding site sides	Electron carriers
I	850	46	NADH (matrix) CoQ (lipid)	FMN Iron-sulfur
II	140	4	Succinate (matrix) CoQ (lipid)	FAD Iron-sulfur
III	248	11	Cyt c (intermembrane) CoQ (lipid)	Iron-sulfur Heme
IV	162	13	O_2 (matrix) Cyt c (intermembrane)	Heme Copper
Cytochrome c	13	1	Cyt c1,a	Heme

1.4.3 Oxidative phosphorylation

As a result of the flow of electrons through the complexes, which is energetically favorable, protons are pumped out of the inner membrane through complexes I, III, and IV (Karp 2008). Overall, protons are pumped from the matrix, across the inner membrane, into the intermembrane space. This generates both a pH gradient (ΔpH) and a voltage gradient (membrane potential, ΔV), across the inner membrane, known as the electrochemical proton gradient (ΔP= ΔV+ ΔpH). In the matrix, then, the pH is higher

(>7) in the matrix than in the cytosol. The voltage gradient creates a negative "inside" and positive "outside". The pH gradient drives protons back into the matrix, which in turn reinforces the effect of the membrane potential. The membrane potential attracts positive ions into the matrix and pushes negative ions out. This proton-motive force is measured in units of millivolt (mV). An average proton-motive force of mitochondria undergoing respiration is approximately 190mV across the inner membrane (Alberts, Johnson et al. 2008).

The electrochemical proton gradient drives ATP synthesis during the process of oxidative phosphorylation. ATP synthase, which is bound to the membrane, creates a hydrophilic pathway across the inner membrane. In turn, protons flow down the electrochemical gradient (Mitchell 1991). This is how cells are able to achieve the energetically unfavorable reaction of adenosine disphosphate (ADP) + inorganic phosphate (P_i) to produce ATP. In the ATP synthase, there is a narrow channel between the stator and the rotor. When protons pass through this channel their own movement causes the rotor ring to spin. When the rotor spins it moves the attached stalk. This mechanical energy of the rotating stalk proteins moving against the rigid head of the ring proteins is generated by the flow of protons. In the ring, three of the six subunits contain binding sites for both ADP and inorganic phosphate. The ultimate production of ATP occurs thanks to the chemical bond energy derived from the mechanical energy of the conformational protein changes that are caused by the rotating stalk. ADP and P_i are bound, condensed, and then released as ATP (Mitchell and Moyle 1965). ATP synthase is capable of producing 100 molecules of ATP per second, generating 3 molecules of ATP per revolution. ATP is then

exchanged from the matrix in return for cytosolic ADP by the adenine nucleotide translocator (Wang, Rennert et al. 2008).

ATP produced by OXPHOS in the matrix is rapidly pumped out into the cytosol. ATP and ADP are constantly exchanged through a carrier protein in the inner membrane. When ATP is hydrolyzed in the cytosol, the resulting ADP is quickly exchanged back into the matrix for generation of more ATP. Cells maintain, in general, a ratio of ATP:ADP of 10:1. Cells also make use of the hydrolysis of ATP, which is energetically favorable, to drive other, unfavorable reactions by coupling them to that process. After subtracting the energy required to release ATP into the cytosol, the result of OXPHOS is that for every pair of electrons donated by NADH, enough energy is produced to form 2.5 molecules of ATP. Additionally, for every molecule of $FADH_2$, OXPHOS can produce 1.5 molecules of ATP. In total, when considering the combined energy production from both glycolysis and the TCA cycle, for one molecule of glucose approximately 30 molecules of ATP are generated during OXPHOS. The efficiency of OXPHOS to turn substrates from diet into ATP is called coupling efficiency. This term encapsulates the efficiency of: 1) the ability of Complexes I, III, and IV to pump protons out of the matrix, 2) generating ATP via the proton flux through Complex V, and 3) any other proton flow through the inner membrane. When there are variations in mitochondrial proteins, the coupling efficiency is affected, meaning that the proportion of calories used by mitochondria for ATP generation (vs. heat production and other processes) is altered.

1.4.4 Respiratory states

In mitochondria literature, there are often references to the "respiratory states" that were first described by Chance and Williams in 1955 (Chance and Williams 1955). These states are defined based on an *in vitro* experiment in which mitochondria were added into a phosphate-containing medium, which causes slow respiration or a "substrate starvation" condition (State I). When ADP is then added, respiration starts to increase slowly and the "substrate starvation" is exacerbated by the increased ATP demand (State II). If substrates (pyruvate, etc.) are added, then respiration increases rapidly to a high rate (State III) and then decreases to a slower rate as the added ADP is converted into ATP (State IV). Respiration continues until oxygen is exhausted, causing an anoxic state (State V). *In vivo*, we typically refer to mitochondria in States III and IV. These are summarized in **Table 1-4**.

Table 1-4 Summary of respiration states

State	Respiration rate	Substrate levels	ADP levels	Oxygen present?
I	Slow	Low	Low	Yes
II	Slow	Low	High	Yes
III	Fast	High	High	Yes
IV	Slow	High	Low	Yes
V	--	High	High	No

The important takeaway from this discussion of respiration states is: mitochondrial oxygen consumption is regulated by the matrix concentration of ADP. If there's no ADP, then the consumption of oxygen is regulated by proton leakage across the inner membrane, which is a slow process (State IV respiration). When ADP is present it binds to the ATP synthase and is rapidly converted into ATP, which requires the use of the

electrochemical gradient. Thus, when protons flow through the ATP synthase proton channel the gradient becomes depolarized. When this occurs, stored fats or carbohydrates are then utilized to provide the needed electrons to the ETC in order to pump the protons back out of the matrix in order to maintain OXPHOS.

1.4.5 Reactive oxygen species (ROS) and mitochondrial damage

In the process of generating ATP needed for cellular function OXPHOS creates by-products, including reactive oxygen species (ROS) (Chance, Sies et al. 1979). ROS are consistently generated in the cell during the process of electron transport, but are typically kept at a steady-state concentration (Cadenas and Davies 2000). Trouble arises for the cell when there is an excess production of ROS (Venditti, Di Stefano et al. 2013). Increased numbers of ROS can cause free-radical chain reactions, in turn causing damage to vital cell components including proteins, lipids, and polysaccharides. Furthermore, ROS can cause damage to mtDNA and nDNA, ultimately disrupting mitochondrial function and causing oxidative stress (Lenaz 1998).

Reactive oxygen species are derived from molecular oxygen (O_2) (Inoue, Sato et al. 2003). Oxygen plays a dual role: on one hand, it is essential for aerobic respiration, and on the other, it acts as a toxin (Gerschman, Gilbert et al. 1954) and is also the precursor to dangerous ROS. Molecular oxygen itself, a vital part of the electron-transport process, is not very reactive when in its electronic ground state. In the electronic ground state, it is bi-radical, which means it contains two unpaired electrons in the outer shell and is a "triplet". Because those two electrons have the same spin, O_2 can only react with one electron at a time. When it is in contact with two electrons in a chemical bond then it is

not prone to reaction. However, if one of its two electrons changes spin and becomes excited, the resultant "singlet" oxygen is highly reactive, since two electrons with opposite spins can react with other pairs of electrons, like those found in chemical bonds (Turrens 2003).

Approximately 90% of consumed oxygen ends up reduced to water by cytochrome oxidase as described previously. However, one-electron reduction of O_2 can occur, creating superoxide anion $O_2^-\cdot$. Formation of $O_2^-\cdot$ can happen both enzymatically and non-enzymatically. Examples of enzymatic sources include NADPH oxidases which are located on the cell membrane (Babior 2000). More relevant to this discussion, non-enzymatic production of $O_2^-\cdot$ is the result of processes along the electron transport chain in mitochondria. ROS that are produced by mitochondria are often generated when electron carriers in the first steps of electron transport remain reduced, meaning that they have more electrons than they should. This happens if OXPHOS is inhibited, or if there is an excessive supply of substrates – such as when too many are derived from dietary calories.

Superoxide anion itself is a relatively stable intermediate, but is the precursor to ROS generated during a process called dismutation, often catalyzed by enzymes called superoxide dismutases (SOD) (McCord and Fridovic.I 1969) (McCord, Keele et al. 1971). $O_2^-\cdot$ can be converted into H_2O_2 and oxygen (Fridovich 1995) (**Equation 1.32**). The role of the SOD enzymes is to maintain the rate of dismuatation so that the levels of $O_2^-\cdot$are kept low at steady-state (Muller, Liu et al. 2004). $O_2^-\cdot$ can be converted to H_2O_2 by a specific mitochondrial matrix enzyme, Mn superoxide dismutase (MNSOD) (Sod2)

or by Cu/ZnSOD (Sod1) within the mitochondrial intermembrane space. H_2O_2 ideally diffuses out of the mitochondria and is converted into water.

The rate at which $O_2^- \cdot$ is produced by the respiratory chain increases if electron flow is reduced (Turrens, Freeman et al. 1982), which can happen in the absence of ADP. Without ADP, the proton gradient "builds up", causing the respiratory chain to become more reduced (State IV respiration). This ultimately leads to an increase in oxygen concentration (Boveris, Chance et al. 1972) .

If there is a subsequent increased steady-state concentration of $O_2^- \cdot$, enough H_2O_2 can be generated that it reacts with reduced transition metals, creating hydroxyl radicals ($OH^- \cdot$) (Boveris and Chance 1973) (**Equation 1.33**), which are strong oxidants that are quite reactive and can disrupt the function of proteins, thus interfering with the function of the mitochondria. This reaction is catalyzed by the transition metals, which can start a chain reaction as they can be reduced again by $O_2^- \cdot$. Because there are so many iron-sulfur centers in the mitochondrial enzymes, they are especially vulnerable.

The *in vivo* location of superoxide generation is difficult to fully pinpoint due to the complexity of the enzyme structures. Several of the redox centers can "leak" electrons to oxygen (Duchen 2004), for example during electron transfer to oxygen by reduced coenzymes, flavins, or iron-sulfur complexes (Andreyev, Kushnareva et al. 2005). Complex I can produce superoxide from reduced flavin of FMN in the presence of highly reduced NAD. It can also produce superoxide during reverse electron transport, when NAD+ is being reduced (Abramov, Scorziello et al. 2007). A two-site (FMN and ubisemiquinone) model was proposed to account for the high rate of production of

superoxides during both forward and reverse electron transport (Treberg, Quinlan et al. 2011). At Complex I, II, and III, the unpaired electron of ubisemiquinone can be donated to molecular oxygen to create superoxide anions (Lambert and Brand 2004).

Although there are many opportunities for mitochondria to produce ROS, they also possess antioxidant defense systems. These primarily aim to prevent the production of $OH^{-}\cdot$ while continuously repairing damage. A concise review of these methods is available in (Venditti, Di Stefano et al. 2013). As mentioned, once there is an imbalance of ROS that cells are no longer able to mitigate, oxidative stress develops (Sies 1997). The ability of mitochondria to remove ROS is dependent on several complicated factors. Different tissue types contain varying numbers of mitochondria. Higher cellular mitochondria levels may indicate higher production of ROS, but as mitochondria themselves are capable of preventing and repairing ROS damage, higher number of mitochondria can also protect against cellular stress (Droge 2002).

The production of ROS can eventually damage many mitochondrial components leading to disruption of mitochondrial function. As OXPHOS is so vital to cellular respiration, when mitochondria are damaged or impaired there can be severe consequences. Mitochondrial myopathy was first observed in the 1960s and described as a "defect of the biochemical function of mitochondria" in skeletal muscle of a patient with "severe hypermetabolism of unknown origin" (Luft, Ikkos et al. 1962). Over the past few decades, it has become more and more evident that mitochondrial defects are present in disease states ranging from diabetes to cancer to neurodegenerative diseases (Wallace 1999).

1.5 Glycolysis

While Chapters 2 and 3 will focus on CEST in the context of OXPHOS, in Chapter 4 we will discuss a novel CEST biomarker for monitoring glycolysis *in vivo*. Glycolysis, unlike OXPHOS, produces ATP without molecular oxygen. Through glycolysis, which occurs in the cytoplasm, cells oxidize glucose by converting each molecule of glucose (6 carbons) into two molecules of pyruvate (3 carbons each) (**Figure 1.5**). Two molecules of ATP are required for this process, which eventually produces four molecules of ATP, for a net gain of 2 ATP per molecule of glucose. Briefly, glycolysis contains ten reactions that are catalyzed by individual enzymes to produce intermediate sugar molecules (Alberts, Johnson et al. 2008). Oxidation of those sugar molecules, which involves removal of electrons by NAD^+, occurs in these small steps so that as much energy as possible can be stored in the carrier molecules, NADH. Two molecules of NADH are produced through glycolysis for every molecule of glucose and they donate their electrons to the electron transport chain described in the previous sections. For most mammalian cells, glycolysis is the initial step in the breakdown of fuel (glucose), and the pyruvate produced enters the TCA cycle in the mitochondrial matrix to be converted into acetyl CoA and CO_2, as described in the previous sections. In certain tissues, when conditions are anaerobic, instead of moving into the mitochondria and used for OXPHOS, the pyruvate and NADH remain in the cytosol. In skeletal muscle, for example, the pyruvate is converted into lactate and NAD^+ is regenerated for additional glycolysis.

The glucose used in glycolysis is obtained through diet; mammals have developed a means of storing fatty acids and sugar for periods of fasting. Sugar is stored as a large polysaccharide, glycogen, which is made up of glucose subunits. This provides short-term storage, so when cells need more ATP than they can generate from available food molecules they can break down glycogen to produce glucose for glycolysis. Glycogen is found in liver and muscle cell cytoplasm. Glycogen does not provide as efficient a means of storage as fat, which releases twice as much energy upon oxidation (Alberts, Johnson et al. 2008). We will discuss lactate production in tumor cells with altered glycolysis, and in skeletal muscle under anaerobic conditions in Chapter 4.

1.6 Summary

Within the constantly developing field of molecular imaging, researchers are always looking for new ways to study biochemical processes *in vivo*. This dissertation explores a new MRI technique, CEST, and its applications to study metabolism noninvasively. In Chapter 2 we will focus on skeletal muscle metabolism and the current ways it is studied *in vivo* and then describe the development of the CEST technique for skeletal muscle applications. Tissues that have large energy demands, such as cardiac, renal, and skeletal muscle are especially compromised by metabolic dysfunction. We have targeted mitochondrial function and developed the CEST technique in order to identify OXPHOS impairment *in vivo*. Within the last 20 years, it became possible to study the genetics of metabolic diseases in a much more robust way, which have been linked to diseases ranging from cancer to mitochondrial myopathy. The clinical study that is the subject of Chapter 3 will discuss several specific genetic mutations that result in defects in

OXPHOS. We will demonstrate the ability of CEST to identify impaired mitochondrial function *in vivo*. Finally, in Chapter 4 we will discuss the development of the CEST technique for measuring lactate *in vivo*, and its relevance to metabolic disorders.

Chapter 2 - Development of Creatine Chemical Exchange Saturation Transfer (CrCEST)

2.1 Introduction

Mitochondrial bioenergetics have been studied extensively with *in vitro* methods in an attempt to understand overall mitochondrial function. Techniques such as fluorescence imaging have provided much information about mitochondrial function in cells and are especially useful for studying mitochondria in different cell types. This method of studying mitochondrial function extends back to the 1960s and 70s, when Britton Chance showed that mitochondrial metabolism could be identified through fluorescence arising from NADH and flavoproteins, which provides information about the redox states and respiratory capabilities of individual cells (Scholz, Thurman et al. 1969, Chance, Schoener et al. 1979). While much of what we know about mitochondrial function has come from such studies, we would prefer to observe mitochondria *in vivo* without disrupting the native environment. Ideally, noninvasive *in vivo* measurements of mitochondrial function would provide enhanced information about biochemical processes in entire systems, especially those disrupted by pathophysiological conditions (Duchen 2004). Mitochondrial function is an ideal target for molecular imaging techniques as discussed in the introduction of Chapter 1. In the 1980s it was suggested that nuclear magnetic resonance (NMR) spectroscopy could be used to study oxidative metabolism in intact muscle tissue. This chapter will review the current spectroscopic techniques used to monitor mitochondrial function and then discuss the initial motivation and work to develop creatine CEST (CrCEST) technology and apply CrCEST imaging in healthy human skeletal muscle.

2.1.1 Skeletal muscle metabolism

CEST imaging for study of *in vivo* metabolism, which will be the focus of the rest of this chapter and Chapter 3, was validated in healthy human skeletal muscle. In this section, we will briefly review some relevant muscle structure and function. Skeletal muscle makes up ~40% of total human body weight and contains ~75% of all body proteins (Frontera and Ochala 2015). It is a significant contributor to many metabolic functions; in addition to maintaining basal energy metabolism, it stores amino acids and carbohydrates that are substrates for other metabolic processes and protein synthesis. It helps maintain body temperature by producing heat and participates in blood glucose regulation. Skeletal muscle is comprised of highly-ordered muscle cells called fibers, which are generally ~100um in diameter and ~1 cm in length. Individual fibers are surrounded by a membrane called the sarcolemma. Muscle fibers are arranged in groups and surrounded by a layer of connective tissue. Individual muscle fibers are mostly composed of protein. The nucleus of muscle fibers controls protein synthesis in particular cellular regions (Alberts, Johnson et al. 2008) (Wolfe 2006). Several proteins, including actin, form a complex that is associated with the sarcolemma and physically connected to the internal proteins or myofilaments. Each fiber is comprised of thousands of myofibrils and millions of myofilaments that form sarcomeres. Sarcomeres are the fundamental contractile units of skeletal muscle. Two important myofilaments are myosin and actin, which make up ~80% of the total fiber protein content (Alberts, Johnson et al. 2008). Myosin is the main molecular motor driving muscle contraction and movement. Muscle fibers are generally classified according to color, red or white, which corresponds to myoglobin content. Myoglobin is a protein that binds iron and carries oxygen to muscle

tissue. Muscle fibers are also distinguished by type of metabolic pathways they utilize: glycolytic vs. oxidative (Schiaffino and Reggiani 2011). Muscle oxidative capacity is correlated with the mitochondrial content. Overall classification is into one of three muscle fiber types (Zierath and Hawley 2004):

1. type I: slow, oxidative, fatigue-resistant
2. type IIA: fast, oxidative, intermediate metabolic properties
3. type IIb or IIx: fastest, glycolytic, fatigable

Muscles produce adenosine triphosphate (ATP) by using glucose, glycogen, fatty acids, or triglycerides through the biochemical pathways of mitochondria discussed in Chapter 1. Utilization depends on the intensity and duration of exercise (Liu, Mac Gabhann et al. 2012). Exercise that is performed at sustainable durations is supported by ATP produced by mitochondrial oxidative phosphorylation. Glycolysis produces ATP rapidly during intense exercise but quickly leads to fatigue and generation of lactate, which will be discussed in more detail in Chapter 4.

Skeletal muscle is very heterogeneous in terms of mechanical, biochemical, and metabolic properties. Muscles contain different compositions of muscle fiber types. This is one of the key motivations for developing an imaging technique that has high spatial resolution capabilities: to provide a more complete view of metabolism across entire large muscle regions.

2.1.2 The creatine-kinase reaction

To provide some context for the use of spectroscopy to study mitochondrial metabolism, first we will examine the creatine-kinase reaction, which utilizes high-energy phosphates that are detectable by MRS. During resting-state conditions, cells produce the majority of their ATP through OXPHOS in the mitochondria. Some tissues, such as cardiac and skeletal muscle, brain, retina, etc., have a very high, rapidly changing demand for ATP (Wallimann, Wyss et al. 1992). What happens when there's a sudden increase in cellular ATP demand, such as during exercise? Cells can't simply increase the intracellular concentration of ATP, because there are many metabolic processes that are tightly regulated by local concentrations of ATP, as well as the overall ratio of ATP/ADP. If cells generated high levels of ATP in response to increased energy demands, many other metabolic processes would be disturbed. Typically, resting cells have a low ATP concentration of ~5mM, maintained by OXPHOS (Infante and Davies 1965). Instead, to accommodate fluctuating energy demands, tissues contain an enzyme called creatine-kinase (CK) that provides a shuttle system for storage of high-energy phosphate in the form of phosphocreatine (PCr). There are isoforms of CK specific to cytosolic muscle or brain tissue, and two mitochondrial-associated isoforms (Mi-CK): ubiquitous and sarcomeric. Those isoforms are located in the mitochondrial intermembrane space and are compartmentalized at the locations where energy is either produced or consumed (Wyss, Smeitink et al. 1992). The function of the CK enzymes is to catalyze the reversible transfer of the γ–phosphate group of ATP to the guanidino group of creatine (Cr), generating ADP and PCr.

$$Cr + ATP \overset{CK}{\Leftrightarrow} ADP + PCr + H^+$$

(Equation 2.1)

During the CK reaction, ATP is produced from the conversion of phosphocreatine and ADP to Cr (Cain and Davies 1962). Creatine is synthesized in the liver and then transported to muscle and other tissues through the bloodstream. ATP is synthesized in the mitochondrial matrix, and the γ–phosphate group is transferred to creatine by the mitochondrial CK isoform in the intermembrane space to generate ADP and PCr. ADP that is generated by the CK reaction is transported into the matrix to be re-phosphorylated into ATP. When cells undergo processes that require an increase in energy, like muscle contraction, PCr is depleted to maintain the available supply of ATP, while keeping the ATP concentration constant. This mechanism allows cells access to an immediate energy supply, without requiring storage of large amounts of ATP (Wallimann, Wyss et al. 1992). PCr diffuses out of the mitochondria into the cytosol to places where it is required to facilitate ATP consumption. Once the instantaneous energy demand is reduced, generation of ATP through OXPHOS leads to a subsequent increase in PCr production to restore it to its previous concentration. The “liberated” or “free” creatine diffuses back into the mitochondria.

There are differences in high-energy phosphate requirement for various tissue types. In fast-twitch skeletal muscle that performs short bouts of intense exercise, there is a large pool of PCr (~25mM). This form of energy demand causes high activity of cytosolic CK, and the overall reaction is near-equilibrium, with the concentrations of ATP and ADP kept constant over the activity period. This allows skeletal muscle cells to buffer the

phosphorylation potential needed for ATPases to function. Other tissue types, like cardiac or slow-twitch muscle, have different energy demands. They require a more continuous supply of high-energy phosphates to perform biochemical reactions that constantly require ATP. In those tissues, like brain and smooth muscle, the CK shuttle acts more like a transport system for PCr, which is present at ~10mM. This is a general explanation of the buffer/transport models of CK enzymatic function, however, there is evidence that the CK system can adapt to new physiological requirements, such as the effects of endurance training in skeletal muscle, and "switch" the function of the CK system, e.g., from buffer to transport (Saks, VenturaClapier et al. 1996).

From the above discussion, it's clear that small metabolites like creatine and phosphocreatine play a vital role in bioenergetics. Unlike ATP and ADP, creatine and PCr can exist at high cellular concentrations without disrupting other biochemical processes. Cells that contain CK systems are capable of high intracellular flux of phosphates, and are also able to buffer the cytosolic phosphorylation potential at a higher level than other cell types. This indicates that cells that utilize the CK system depend on it for proper function of other enzymatic processes. In muscular diseases and metabolic disorders, creatine kinase kinetics are often affected (Bottomley, Lee et al. 1997).

How does the CK system report on mitochondrial function? After a period of increased energy demand, like exercise, PCr is temporarily depleted. The rate of "recovery" of PCr, or the return to baseline concentrations, is reflective of the oxidative phosphorylation capacity of the mitochondria. In other words, the rate at which PCr recovers is correlated to the return of the cells to resting-state oxidative phosphorylation by mitochondria. A

delayed recovery of PCr has shown to be associated with metabolic disorders where mitochondrial function is compromised. Luckily, it was discovered that PCr, along with inorganic phosphate, and the three phosphate groups of ATP, are visible by a specific type of NMR to look at phosphorus resonances, ^{31}Phosphorus magnetic resonance spectroscopy (^{31}P MRS).

2.1.3 ^{31}Phosphorus MRS

Metabolism of exercising muscle and myocardium has been studied extensively through non-invasive magnetic resonance (MR) techniques. While ^{1}H MRS methods can be used to measure total creatine (PCr+Cr), they cannot be used to differentiate PCr from Cr and thus have had limited application towards muscle energetics. The most commonly used technique has been ^{31}P MRS (Gorenstein 1984). For many decades, it has been the standard technique for the study of phosphorus compounds *in vivo* (Chance and Bank 1995, Lee, Komoroski et al. 2012). It is an extremely useful tool due to particular properties of phosphorus: its natural abundance (100%), spin (1/2), and large range of chemical shifts (Hoult, Busby et al. 1974, Gorenstein 1984). Inorganic compounds had been studied using ^{31}P MRS since the early 1950s (Dickinson 1951, Cohn and Hughes 1962), and during the 1970s it was applied to the study of biological phosphorus compounds (Burt, Glonek et al. 1977). Since then, it has been an invaluable technique for the study of muscle metabolism. In muscle tissue, ^{31}P MRS can noninvasively measure the phosphate components of the creatine-kinase (CK) reaction (Kemp, Meyerspeer et al. 2007). Concentrations of these metabolites (PCr, ATP, inorganic phosphates (Pi), phosphomonoesters (PME), and phosphodiesters (PDE)) can be obtained from ^{31}P

spectra. Additionally, changes in intracellular pH can be estimated by changes in chemical shift of the inorganic phosphate (P_i) peak (Moon and Richards 1973, Thompson, Kemp et al. 1995).

As mentioned in **Section 2.1.2**, during exercise of healthy muscle tissue, the CK reaction maintains a constant concentration of ATP by conversion of PCr to Cr. ^{31}P MRS spectra of exercising skeletal muscle shows the depletion of PCr and any changes in intracellular pH (Burt, Glonek et al. 1976). It can be applied during dynamic exercise studies to monitor the PCr depletion and follow the recovery after cessation of exercise (**Figure 2.1**). Conditions of muscle fatigue (Dawson, Gadian et al. 1978, Bendahan, Giannesini et al. 2004) or muscle injury can be studied by ^{31}P MRS. Muscle related disorders, such as muscular dystrophy, mitochondrial myopathies (Chance, Eleff et al. 1981, Argov and Bank 1991), and cardiac disease (Yabe, Mitsunami et al. 1995) have also been studied using ^{31}P MRS. More background about mitochondrial ^{31}P MRS studies will be given in Chapter 3.

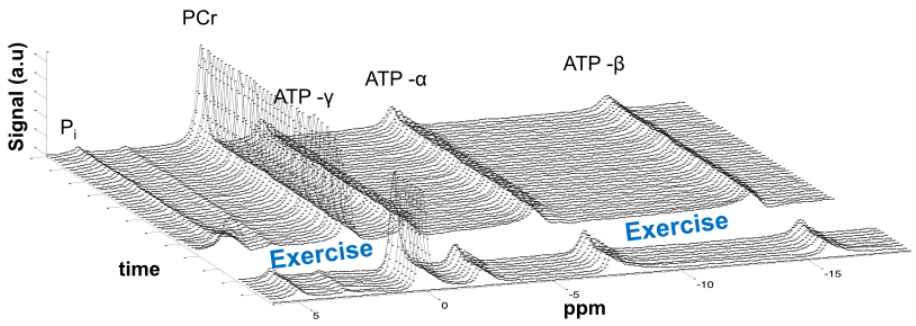

Figure 2.1 ^{31}P MRS spectra. ^{31}P MRS spectra from skeletal muscle shown at rest, and following a period of mild exercise. The three ATP phosphate groups are visible, as well as inorganic phosphate.

The ^{31}P MRS technique has been critical to understanding muscle energetics, but it has several disadvantages that have proved particularly challenging, especially for large clinical studies. Technical limitations of ^{31}P MRS may have contributed to heterogeneity in the findings of previous studies (Roussel, Bendahan et al. 2000). Characteristic of most spectroscopy techniques, ^{31}P MRS suffers from low sensitivity, even lower than ^{1}H MRS, due to the small gyromagnetic ratio of ^{31}P (Hoult, Busby et al. 1974). One of the most impactful limitations is that ^{31}P MRS has poor spatial resolution. The disadvantage of poor spatial resolution becomes apparent if during exercise studies, subjects utilize muscle groups in an unexpected way. If subjects exercise a muscle that is not the target of the study (for example, using the anterior tibialis instead of the gastrocnemius muscles in calf muscle) and not included in the coil detection region, it will appear that the subject hasn't exercised. This presents a serious challenge especially for studies of patient populations who often can't follow instructions precisely due to physical limitations. Being able to produce a more accurate "snapshot" with higher resolution of every muscle simultaneously would perhaps allow data to be salvaged from a different muscle group, even if the target muscle wasn't utilized. It may also help to ensure a comprehensive understanding of the metabolic response to disease in muscle. Techniques for studying muscular diseases and secondary conditions that also affect muscle energy metabolism would be greatly benefitted by a more robust method for studying OXPHOS *in vivo*.

To this end, in 2011 the Reddy lab began developing a chemical exchange saturation transfer (CEST) (Sherry and Woods 2008) for imaging of creatine (CrCEST). The concentration of creatine, like PCr, should be altered after a period of exercise. Creatine is suitable for CEST studies as it contains amino groups in the slow-intermediate exchange regime and exists at high cellular concentrations (~7-20mM in skeletal muscle). The goal for creatine CEST (CrCEST) was to observe increases in [Cr] after a dynamic exercise study analogous to the decrease in [PCr] observed by spectroscopy.

The rest of this chapter will review the original development of CrCEST in phantoms (Haris, Nanga et al. 2012) and the preliminary applications in skeletal muscle (Kogan, Haris et al. 2013, Kogan, Haris et al. 2014) and cardiac tissue (Haris, Singh et al. 2014), and discuss the capability of CrCEST imaging in the brain (Cai, Singh et al. 2015). The rest of this chapter will detail a small reproducibility study performed at 3T and include the designs for a custom-built MRI-compatible ergometer. Chapter 3 will be entirely focused on a clinical CrCEST study that was performed at 7T in a population affected by mitochondrial dysfunction.

2.2 Development and application of CrCEST

2.2.1 CrCEST in phantoms

Creatine (Cr) was originally targeted for CEST experiments in light of some of the shortcomings of ^{31}P MRS described above. The general CEST methodology can be adapted to metabolites that possess adequate concentration *in vivo* and have an amenable exchange rate (Kogan, Hariharan et al. 2013). The following discussion of CrCEST implementation is adapted from a review chapter on CrCEST imaging to which the

author contributed (McMahon, Gilad et al. 2017). During initial development of creatine CEST, limited information was available about exchange rates of the creatine kinase metabolites under physiological conditions (i.e., in phosphate-buffered solution, at physiological pH and temperature). Using high-resolution ^{1}H NMR (9.4T), the resonances from the CK components with exchangeable protons (Cr, PCr, and ATP) were identified (**Figure 2.2A**).

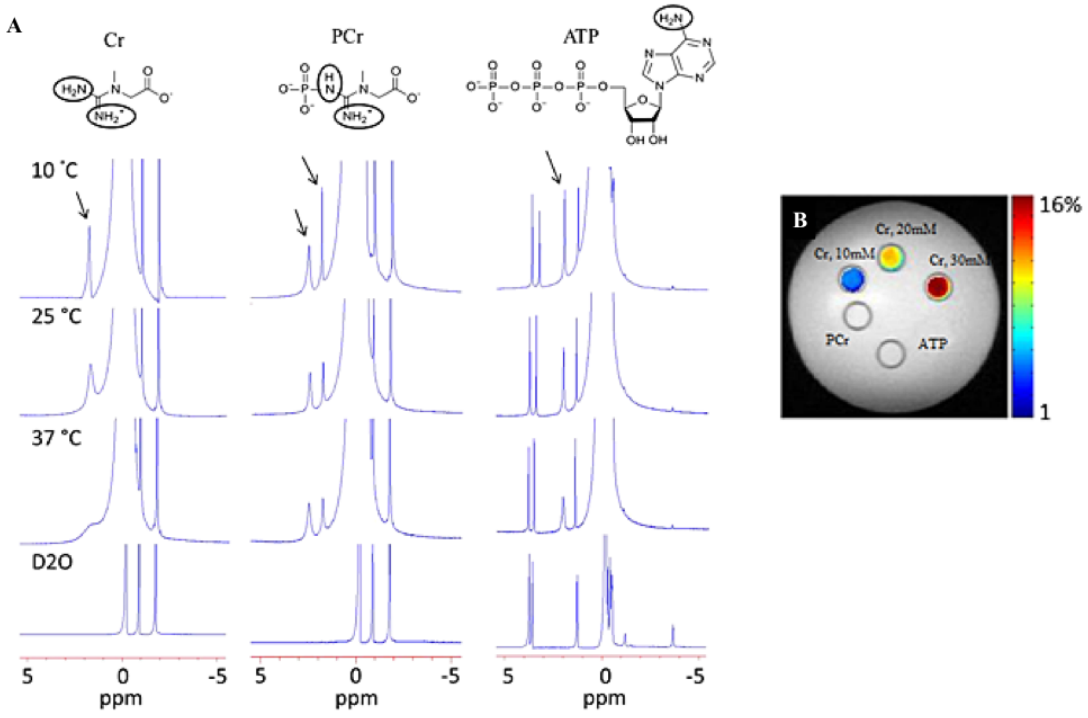

Figure 2.2 High-resolution NMR-derived location of exchangeable protons and CEST maps. A) high resolution ^{1}H NMR spectra obtained at 9.4 T showing sharp amine proton resonances of Cr (1.8 ppm), PCr (2.5 ppm and ~ 1.8 ppm) and ATP (2.0 ppm) at lower temperatures while broadening was observed at higher temperature due to exchange with bulk water; B) CEST mapping at 3 T acquired at 1.8 ppm from different concentrations of creatine, phosphocreatine, and ATP overlaid on the proton image show

the predominant CEST contrast from Cr. (*Reprinted with permission (Haris, Nanga et al. 2012))*

Creatine in its ionic form has two groups of guanidinium protons (imine: $=NH_2^+$ and amine: $-NH_2$) that show a single resonance at 1.8 ppm away from water (Haris, Nanga et al. 2012). Phosphocreatine has one amide group (2.5 ppm), and one amine group (1.8 ppm), while the amine group of ATP resonates at 2.0 ppm (van Zijl and Yadav 2011). When the exchange rates for these protons were determined (McMahon, Gilad et al. 2006), it was discovered that Cr has a much faster exchange rate ($950\pm100\ s^{-1}$) than the other components ($<140\pm50\ s^{-1}$) of the CK reaction. This result was anticipated due to the observed line broadening of creatine's exchangeable protons at physiological temperature (37°C), and pH (7.0). Line broadening indicates that the Cr protons are in faster exchange with bulk water compared to those of PCr or ATP. The pKa values determined for the CK metabolites at 37°C validate the exchange rates. Under physiological conditions, creatine has a lower pKa than both PCr and ATP, suggesting a faster dissociation, which leads to faster exchange with bulk water spins. From these initial experiments, it was determined that at 3T, the exchange rate of Cr is in the slow-intermediate exchange regime ($k\leq \Delta\omega$, $\Delta\omega$=1300rad/s). On the other hand, the exchange rates of amine protons of PCr ($\Delta\omega$=1900rad/s) and ATP ($\Delta\omega$=1500rad/s) are in a slow exchange regime at 3T ($k<<\Delta\omega$). Based on the exchange rate information it was determined that CEST imaging could be performed on the exchangeable protons of creatine. An initial study was performed on creatine phantoms, as well as the other creatine-kinase reaction components that contain exchangeable protons (PCr, ADP, and ATP).

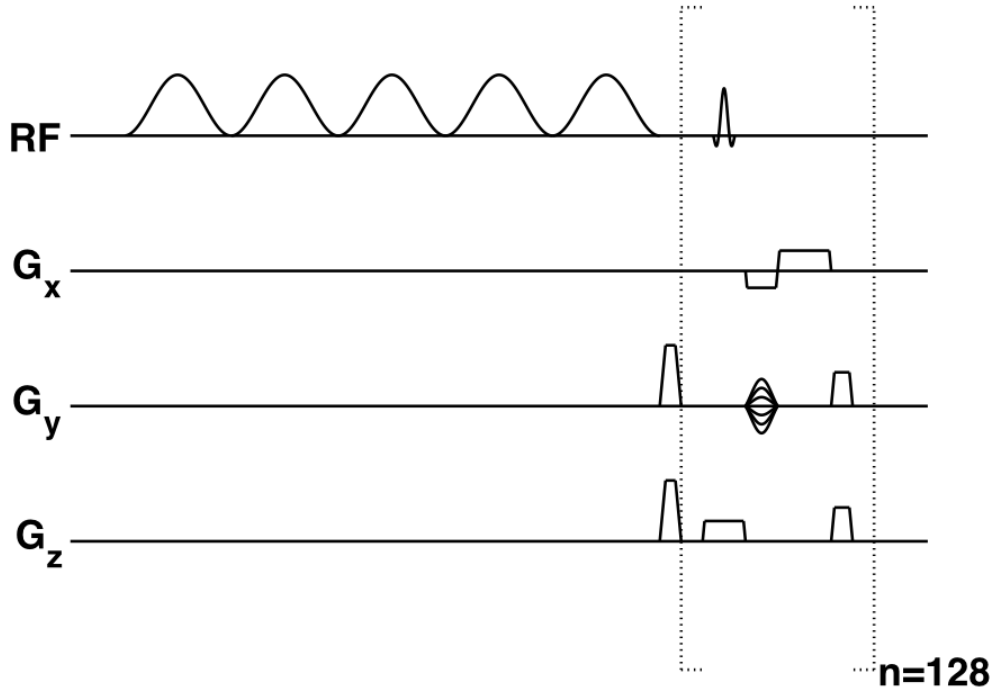

Figure 2.3 Schematic for the CEST pulse sequence

Phantom experiments typically consist of a CEST imaging protocol performed on an NMR tube containing the metabolite of interest in a buffered saline solution at a physiological temperature and pH. This provides a concentration-dependent CEST contrast that can then be used to guide subsequent *in vivo* experiments. CEST imaging of creatine-kinase metabolites was performed at 3T on separate phantoms containing components of the CK reaction (Cr, PCr, ATP, and ADP) at approximate physiological concentrations (Wallimann, Tokarska-Schlattner et al. 2011), (**Figure 2.2B**): Cr: 10, 20, and 30mM; PCr: 10mM; and ATP: 5mM. The same experiment was performed on a

5mM phantom of ADP, the amine protons of which had a similar exchange rate and pKa value to those of ATP (data not shown). Although the target metabolite for CEST was creatine, the other metabolites that may be present physiologically were also included so as to determine whether they also contribute to any observed CEST contrast. A preliminary z-spectrum (Ward, Aletras et al. 2000) was gathered on a 30 mM Cr phantom, and showed a broad resonance centered at ~ 1.8 ppm (**Figure 2.4**), attributed to the ($-NH_2$) protons, also observed in those earlier ^1H NMR experiments.

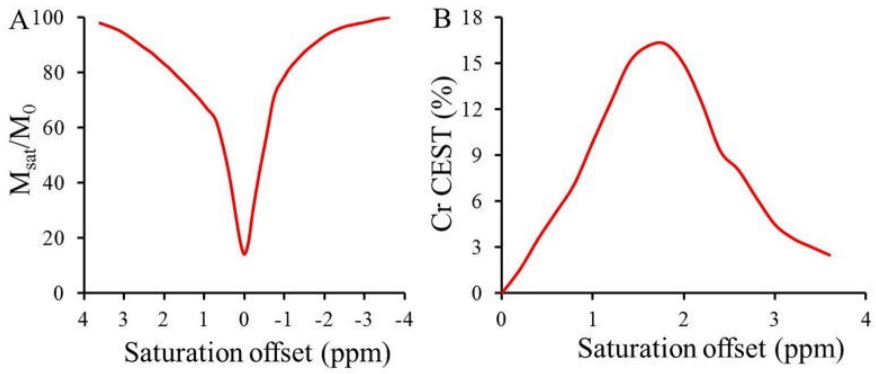

Figure 2.4 CEST effect from creatine. A) Z spectra and B) CEST asymmetry curve collected at 3 T on a 30mM creatine phantom show a broad resonance from creatine amine protons centred at ~ 1.8 ppm. *(Reprinted with permission (Haris, Nanga et al. 2012).)*

For the CEST experiments in this dissertation work, a specially optimized saturation pulse train was used that consisted of 20 Hanning windowed rectangular pulses of 49 ms duration, each with a 1 ms delay between them, for total saturation duration of 1s. The saturation pulse excitation bandwidth was 5 Hz for 1s pulse, with a 1% bandwidth of 20 Hz (~0.15 ppm at 3T). CEST contrast for Cr was computed using **Equation 1.25**, and mapped onto a T_2* weighted reference image. M_{sat} ($-\Delta\omega$) and M_{sat} ($+\Delta\omega$) are the B_0

corrected MR signals acquired while saturating at -1.8 ppm and +1.8 ppm from water resonance. The CEST contrast map was further corrected for B_1 inhomogeneity.

With these parameters, the CrCEST contrast observed in Cr phantoms showed a linear relationship to Cr concentration with a slope of 0.6%. For CrCEST imaging of phantoms at 3T, the optimal saturation pulse amplitude (B_{1rms}) was 3.64 μT. No appreciable CEST was observed from the other components of the CK reaction, which is likely due to their slower exchange rates. As discussed previously, one of the expected benefits of using CEST instead of traditional spectroscopy is an increase in sensitivity. This was observed using single voxel point resolved spectroscopy (PRESS) on the 30mM Cr phantom (**Figure 2.5**).

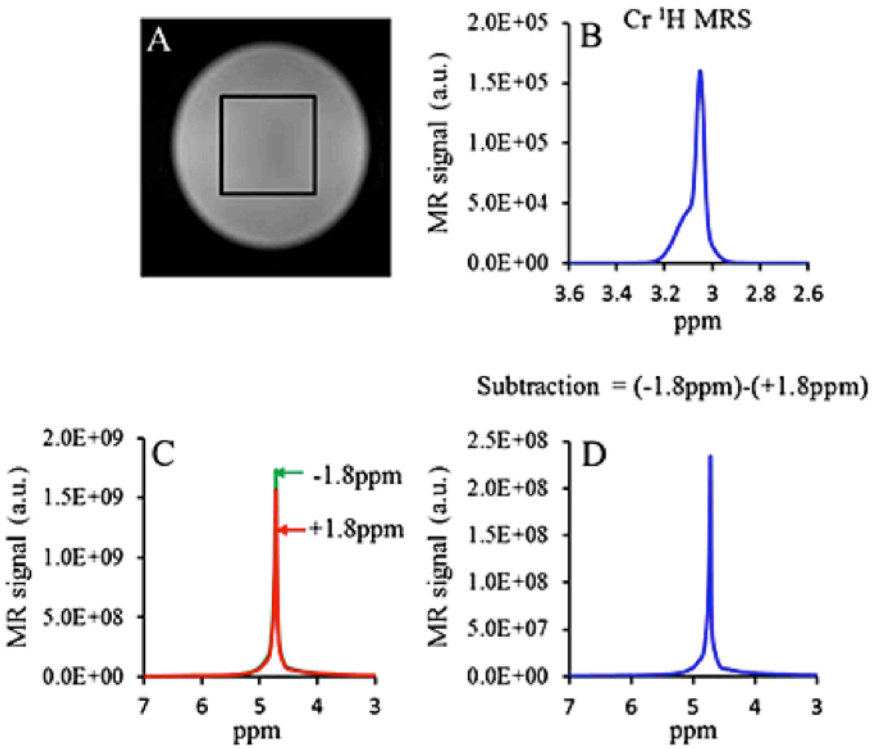

Figure 2.5 Sensitivity of CrCEST compared to ^{1}H MRS. A) image of a 30mM creatine phantom, showing the single voxel localization; B) ^{1}H MRS PRESS water suppressed spectrum from the voxel. The measured amplitude of the Cr peak at 3.02 ppm was 1.5 x 10^{5} units; C) Two water ^{1}H resonance spectra obtained when a saturation pulse was applied at ± 1.8 ppm. The subtracted spectrum is shown in D, with an amplitude of 2.3 x 10^{8} units. Therefore, the sensitivity of Cr CEST was ~ 1500 times higher than ^{1}H MRS ($2.3x10^{8}$ / $1.5x10^{5}$ = 1533). Data acquired at 3T. *(Reprinted with permission (Haris, Nanga et al. 2012).)*

Furthermore, the sensitivity of CrCEST is approximately three orders of magnitude greater than ^{31}P MRS due to the low receptivity of ^{31}P compared to ^{1}H (Kogan, Haris et al. 2014). The benefit of such increased sensitivity is the ability to detect relatively small changes in Cr levels at high resolution (Haris, Nanga et al. 2012).

2.2.2 in vivo CrCEST: skeletal muscle exercise at ultra-high field

After establishing that CrCEST images could be obtained from simple phantoms the next goal for CrCEST was implementation in skeletal muscle *in vivo*. The ultimate goal was to detect creatine in muscle through the CEST technique and then to measure dynamic changes in creatine induced through an exercise paradigm. Analogous to ^{31}P MRS of PCr, this would provide an indirect measure of OXPHOS as discussed in Chapter 1. The expected result from CrCEST of muscle post-exercise, based on our understanding of the creatine-kinase reaction, was an *increase* in CrCEST signal proportional to the *decrease* observed in the ^{31}P MRS signal of PCr. This was primarily the thesis work of Feliks Kogan in the Reddy lab (Kogan, Haris et al. 2013) and is the basis for the subsequent reproducibility and clinical studies that were the focus of this work. The first *in vivo* CrCEST study on healthy humans was performed at 7T. An important initial step for *in vivo* optimization was maximizing both the $CrCEST_{asym}$ and the signal-to-noise (SNR) ratio. While CrCEST signal increased with increasing B_{1rms}, this led to a decrease in SNR (**Figure 2.6**).

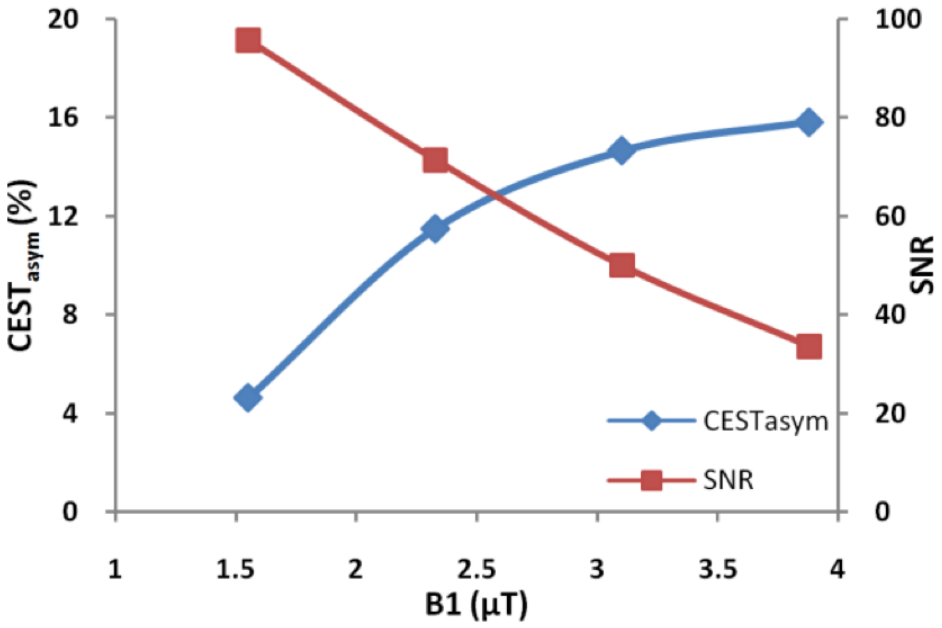

Figure 2.6 CEST asymmetry vs. SNR. Plot of the $CEST_{asym}$ as well as the signal-to-noise ratio (SNR) of the anatomic image as a function of saturation pulse B_{1rms} for a 500 ms pulse. *(Reprinted with permission (Kogan et al).)*

To maximize both of these parameters, a saturation pulse train with a B_{1rms} of 123Hz (2.9µT) and 500ms duration, with a SHOT TR of 8s were chosen for CrCEST *in vivo* at 7T. Another consideration for *in vivo* imaging was the fat content of the muscle tissue. In order to reduce the fat signal, a chemical shift selective fat saturation pulse was applied before image readout.

CrCEST of human skeletal muscle was performed on calf muscles at 7T using a 28-channel ^{1}H knee coil. One of the complexities of CEST data lies in calculating accurate CEST contrast when there are B_0 and B_1 inhomogeneities. To correct for any inhomogeneities, water saturation shift reference images (Kim, Gillen et al. 2009) and B_1 maps were collected along with CEST maps using a double-angle method. By utilizing higher order shimming, B_0 inhomogeneities for a human skeletal muscle (imaging slice thickness = 4mm) could be kept within 0.3 ppm (ΔB_0<0.3ppm) and thus CrCEST images were collected in a chemical shift range of ±1.5 to ±2.1 ppm, acquired in steps of 0.3ppm, for a total of 6 images. As Cr amine protons have a chemical shift of 1.8 ppm downfield from water (Haris, Nanga et al. 2012), this allows for adequate B_0 inhomogeneity correction in calculating $CrCEST_{asym}$. To correct for B1 inhomogeneities, B_1-field maps were obtained using the double angle method as described previously (Cai, Haris et al. 2012, Singh, Cai et al. 2013), using a 2D single-slice fast spin echo (FSE) readout sequence, acquiring two images using preparation square pulses with duration (τ) and flip angles (θ) 30° and 60°. We used the RF pulse amplitude for the 30° flip-angle as a reference B_1 ($B_{1reference}$). Flip angle maps were generated by solving:

$$\frac{\cos(2\theta)}{\cos(\theta)} = \frac{S(2\theta)}{S(\theta)}$$

where S(θ) and S(2θ) represent pixel signals in the image with the preparation flip angle θ and 2θ respectively. We generate a B_1 field map from the flip angle map using $B_1=\theta(360\tau)^{-1}$. The CEST contrast maps were corrected using the coefficient of $B_1/B_{1reference}$. Then, second-degree polynomials were fitted to the measured CEST

contrast over a range of B_1 amplitudes. The CEST asymmetry was corrected based on the coefficients of the polynomial for a given tissue (muscle, in this case) and using the B_1 field map described above.

In resting muscle tissue, CrCEST maps showed a uniform $CrCEST_{asym} \approx$ 12-15% on average (**Figure 2.7A,B**). The exercise paradigm consisted of two minutes of mild plantar flexion, a type of exercise designed to utilize the muscles in the posterior compartment of the lower leg. Exercise was performed in the magnet using a MRI-compatible, pneumatically controlled foot pedal set at a constant pressure for all of the subjects. CrCEST images were acquired with a temporal resolution of 48s both before (2 min total) and after (8 min total) exercise. CrCEST imaging during exercise is not feasible due to the extreme sensitivity of CEST to motion.

For this initial study of CrCEST *in vivo*, only mild exercise was performed in order to maintain a consistent pH. During strenuous exercise, the pH of the muscle can drop, due to breakdown of glycogen and production of lactate (Iotti, Lodi et al. 1993). A pH decrease would consequently decrease the exchange rate between Cr amine protons and water protons, leading to a lower CEST contrast (Singh, Haris et al. 2011). An example set of CEST images for one subject are shown in **Figure 2.7C**, where an increase in the MG and LG is observed post-exercise and recovers within two minutes. Two minutes of mild exercise was sufficient to induce creatine changes in exercising muscle without changing the pH of the muscle tissue. In CrCEST maps post-exercise, an increase in CrCESTasym from 1%-7% was observed in various muscle groups (**Figure 2.7D**) for 8 subjects.

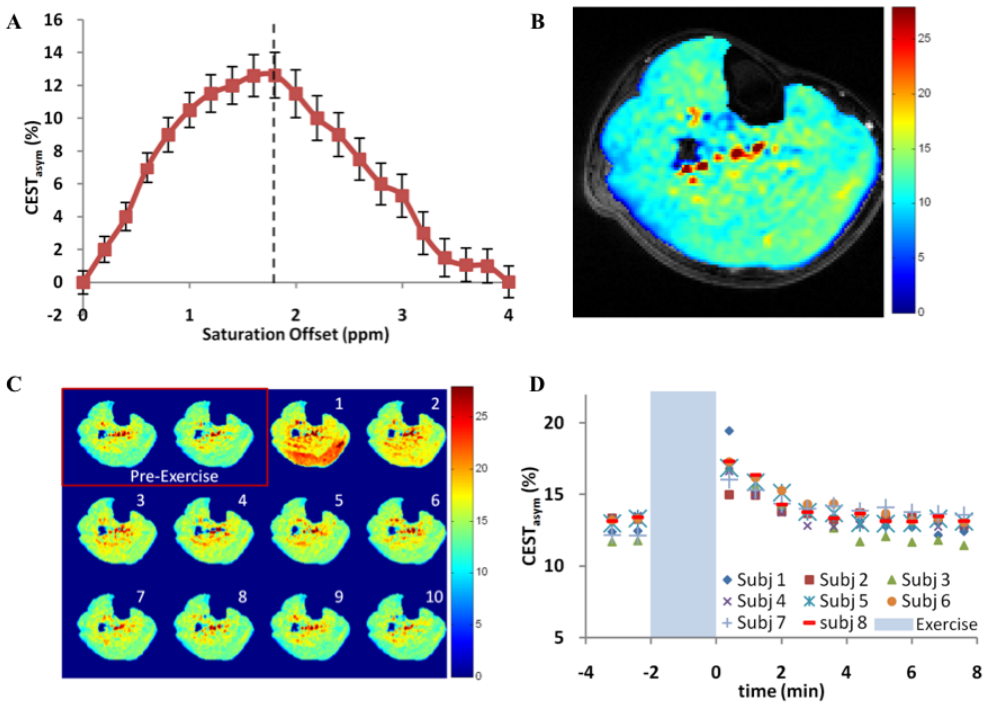

Figure 2.7 CrCEST application in healthy skeletal muscle. A) CrCEST asymmetry plot showing a peak at 1.8ppm; B) resting-state CrCEST image showing uniform contrast over the whole muscle region, demonstrating the enhanced spatial resolution of CEST; C) baseline CEST maps from one subject followed by post-exercise images acquired with a temporal resolution of 48s; D) $CrCEST_{asym}$ (%) plotted for 8 healthy subjects, showing an increase in creatine immediately after exercise followed by a decrease to baseline. *(Reprinted with permission (Kogan, Haris et al. 2014).)*

The results from the CEST experiments were compared to the results from ^{31}P MRS, performed on the same subjects in a separate bout of exercise, using the same paradigm. Creatine recovery over 8 minutes, measured by CrCEST, was strongly correlated to PCr recovery measured with ^{31}P MRS. The recovery times of Cr (measured by CEST) and PCr (measured by ^{31}P MRS) showed good agreement (**Figure 2.8**). At 7T, 0.84% $CrCEST_{asym}$ was reported per mM Cr. An exciting finding was the ability of CrCEST to

distinguish between specific muscle group utilization while exercising. Plantar flexion exercise primarily causes utilization of the soleus muscle and the medial (MG) and lateral (LG) heads of the gastrocnemius muscles. Following exercise, creatine changes were observed primarily in the gastrocnemius and soleus muscles, depending on individual subject utilization. The CrCEST technique was able to distinguish between varying levels of muscle utilization between subjects. Other muscle groups, primarily the tibialis anterior (AT), did not show a significant increase in Cr post exercise. Less than a 1% increase in $CrCEST_{asym}$ was observed in that muscle in the majority of subjects. This demonstrated the precise spatial resolution of CEST. From this pilot study in healthy subjects, it was determined that this method of observing the CK reaction *in vivo* has excellent spatial resolution, which is an important improvement over ^{31}P MRS.

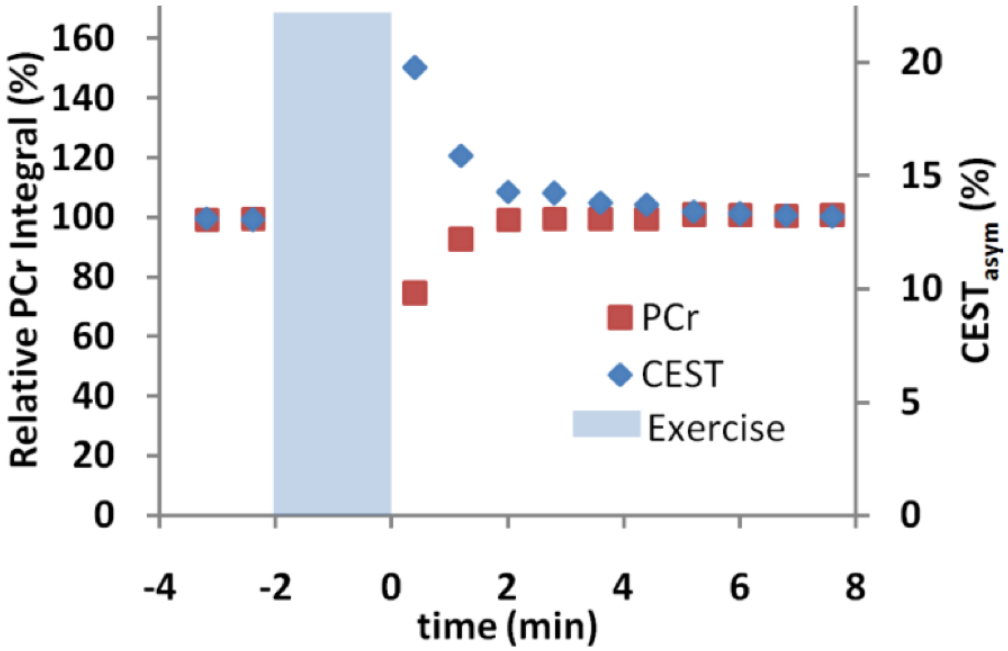

Figure 2.8 CrCEST vs. ^{31}P MRS. The signal from creatine measured by CEST in skeletal muscle pre- and post-exercise showed good agreement with the results from ^{31}P MRS measurements of PCr with the same exercise paradigm. *(Reprinted with permission (Kogan, Haris et al. 2014).)*

In addition to the benefits of spatial resolution, the anticipated enhanced sensitivity was indeed observed in *in vivo* CrCEST compared to spectroscopy. As noted previously, ^{31}P has low sensitivity, due to the lower gyromagnetic ratio of ^{31}P (17.235 MHz/T) compared to that of ^{1}H (42.576 MHz/T) which leads to a receptivity of ^{31}P that is only 0.066 that of ^{1}H (Levitt 2008). The water of muscle tissue has a proton concentration of 82.5 M. Based on the 0.84% CEST observed per mM Cr, 1 mM Cr signal leads to ~700 mM change in

water. Therefore, CrCEST has over three orders of magnitude higher sensitivity than ^{31}P MRS.

In **Section 2.2.1**, we noted that phantom experiments showed no contribution from ATP, ADP, and PCr to the CrCEST effect at 1.8 ppm. During the 7T exercise study, there was no observed change in pH, T_2, or MTR, and the CEST effects from other CK reaction metabolites were negligible. Based on this initial work, it was concluded that the CrCEST technique *in vivo* provides an accurate measure of the changes in muscle Cr concentration following exercise (Kogan, Haris et al. 2013).

2.2.3 Implementation of in vivo CrCEST at clinical-strength field

As noted in Chapter 1, there are numerous disease states that could benefit from study of noninvasive molecular imaging techniques. Despite the impressive results at high field (7T), in order for the CrCEST imaging technique to be applicable to widespread patient populations, it also needed validation at clinical-strength fields (3T) (Kogan, Haris et al. 2014). There were several challenges in translating CrCEST from 7T to 3T. At lower fields, the chemical shift ($\Delta\omega$) between Cr amine protons and free water protons is decreased (~540 Hz at 7T vs. ~225 Hz at 3T). This means that at 3T, the saturation pulse is necessarily applied closer to the water resonance than it would be at 7T. The result is increased direct saturation of bulk water. Increased direct water saturation confounds the CEST measurement and also leads to a loss of SNR in the CEST images. To mitigate direct water saturation, a lower B_1 is required for optimal CEST, but consequently decreases the labile proton saturation efficiency, and decreases the overall $CrCEST_{asym}$.

Despite these drawbacks, CrCEST is possible at a lower field thanks to the exchange rate of Cr amine protons, which still falls in the slow-intermediate regime at 3T. The dependence of the change in CrCEST on the change in creatine concentration following exercise at 3T (0.45% $CrCEST_{asym}$/mM Cr) is approximately half of that observed at 7T (0.84% $CrCEST_{asym}$/mM Cr). The T_2 relaxation times in muscle are longer at 3T, (T_2 (3T) = 29.3 msec, T_2 (7T)=23.0 msec) (Jordan, Saranathan et al. 2013). This somewhat lessens the SNR lost due to increased direct water saturation at 3T.

There are also advantages to CrCEST imaging at 3T, including the shorter T_1 relaxation times at 3T than at 7T. This allows for increased temporal resolution, since the time necessary to allow for complete longitudinal relaxation between saturation pulses (SHOT TR) is directly correlated to the T_1. Temporal resolution is an important consideration when applying CrCEST to studies of creatine kinetics, which have a time course on the order of 30 seconds to a few minutes following exercise (Argov and Bank 1991). When implementing the CrCEST sequence at 3T, the TR was minimized to optimize the temporal resolution while maintaining adequate SNR, and we were able to achieve a temporal resolution of 24s.

Similar to the experiments performed at 7T, changes in CrCEST in the calf muscles of healthy human volunteers were mapped at 3T following plantar flexion exercises (Kogan, Haris et al. 2014) (**Figure 2.9)**.

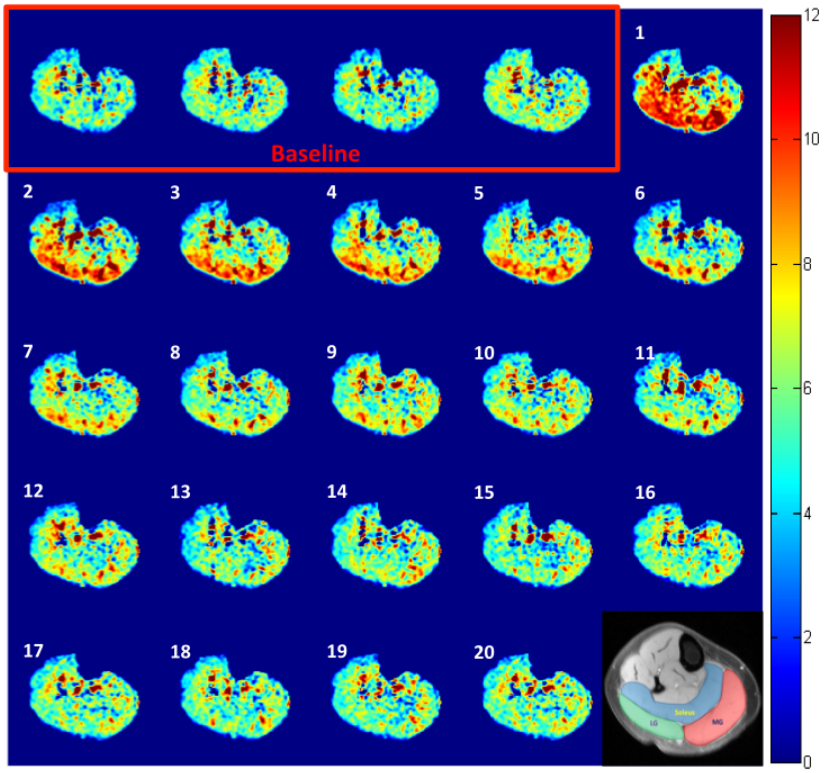

Figure 2.9 CrCEST in skeletal muscle at 3T. The baseline, resting $CrCEST_{asym}$ and post-exercise maps acquired with a temporal resolution of 24s demonstrate the feasibility of CrCEST at lower field strengths. *(Reprinted with permission (Kogan, Haris et al. 2014).)*

Creatine metabolism is vital not just in skeletal muscle, but also in cardiac muscle and in the brain. The next two sections will summarize some of the initial work that is currently underway to develop the CrCEST technique for application in those tissue types.

2.2.4 Application of CrCEST in imaging of myocardial metabolism

Myocardial metabolism can be disrupted due to an event such as cardiac ischemia or infarction, making it another desirable candidate for CrCEST. CrCEST imaging and spectroscopy were first performed on non-infarcted, excised, lamb heart tissue.[30]. *Ex vivo* tissue was used in order to optimize the imaging parameters for myocardial tissue and total Cr concentration was measured using ^{1}H MRS. The Cr concentration was validated using the perchloric acid (PCA) extraction method, in which a positive correlation was observed between the imaging method and the biochemical method. For this tissue, the mean sensitivity (n = 26) of CrCEST is 0.8% CrCEST contrast per 1 mM of Cr at 37 °C. For a comparison of infarcted tissue to non-infarcted tissue, CrCEST maps were acquired from *ex vivo* swine myocardial tissue. Infarcted tissue has lower CrCEST contrast (4.7 ±1.2%) than non-infarcted tissue (10.4 ±2.0%) (**Figure 2.10**).

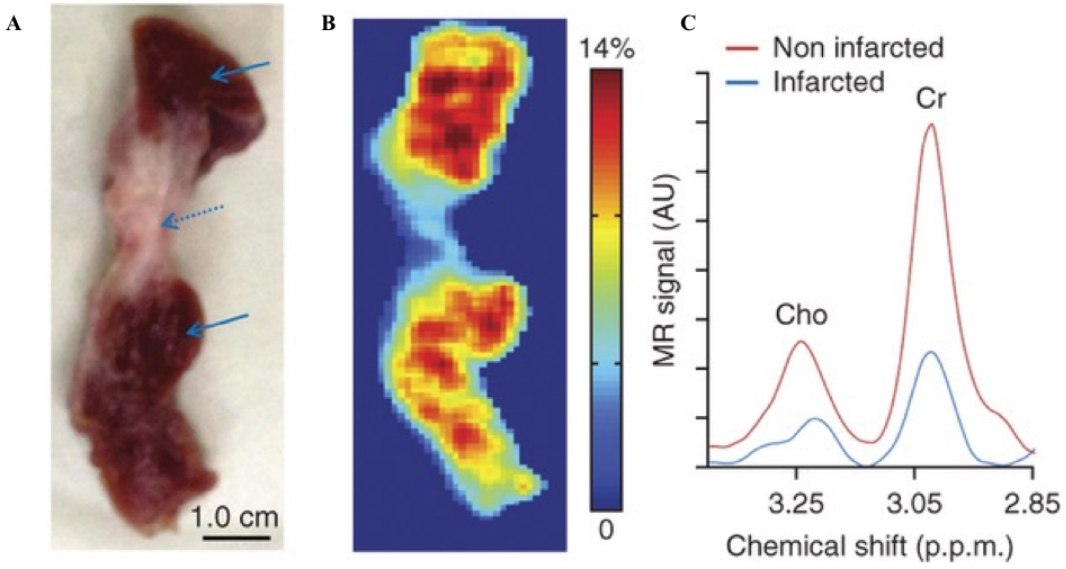

Figure 2.10 Ex vivo CrCEST of noninfarcted and infarcted myocardial tissue from swine.

A) an infarcted region (shown with a dotted arrow) is clearly visible in the *ex vivo* tissue; B) CEST maps overlaid onto an anatomical image show lower creatine in the infarcted region; C) ^{1}H MRS of creatine and choline validate the CEST results, showing lower creatine signal in the infarcted area. *(Reprinted with permission (Haris, Singh et al. 2014).)*

In vivo CrCEST for myocardial imaging was performed on swine and sheep with infarctions, using healthy animals as a control (**Figure 2.11**) (Haris, Singh et al. 2014). CrCEST maps from two healthy swine displayed uniform CrCEST contrast in myocardium. Swine and sheep with infarcted myocardia had lower CrCEST contrast in the infarcted regions compared to the normal myocardial regions. CrCEST imaging gave consistent regional (infarcted vs. non-infarcted) contrast values across all animals studied.

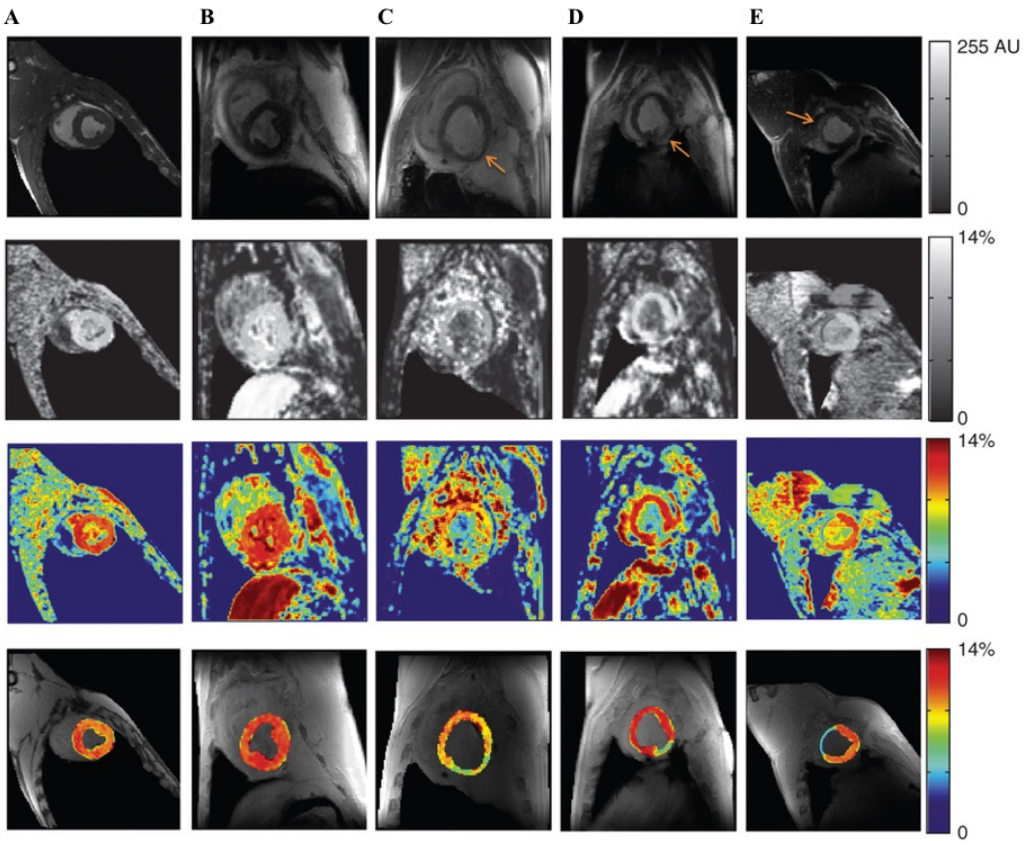

Figure 2.11 In vivo CrCEST data. A, B) the first two columns show normal swine hearts; C, D) two infarcted sheep hearts; E) one infarcted swine heart. Row 1: anatomical CEST-weighted images of the left ventricle, gray scale; row 2: CrCEST maps; row 3: color-coded CrCEST maps; row 4: overlaid color CrCEST maps. *(Reprinted with permission (Haris, Singh et al. 2014).)*

In myocardial imaging, there may be changes in CrCEST in the ischemic and infarcted regions of myocardium due to changes in T_2, MTR, and water content. In these tissues, there is the potential for an increase in water content. This leads to a reduction in Cr concentration and hence CrCEST. However, there is also a decrease in MTR and an increase in water T_2, which would cause an increased CrCEST. Thus, the effects of

changes in water content, MTR, and T_2 compete with each other, and appear to have no appreciable contribution to the $CrCEST_{asym}$.

As mentioned in Chapter 1, CrCEST contrast may also be affected by pH. The CrCEST contrast in infarcted regions of myocardium may be underestimated, because infarcted tissue is expected to have a pH between 6.5 and 7.0. Consequently, the lower CrCEST contrast observed in the infarcted myocardium may be the result of an integrated effect of both lower exchange rate resulting from the decreased pH and lower Cr concentration compared to those in healthy tissue. Thus, although pH may influence the magnitude of CrCEST, it would only enhance the capability of CrCEST in discriminating between healthy and infarcted myocardium (Haris, Singh et al. 2014).

2.2.5 CrCEST application in brain imaging

CrCEST also has the potential to be used for study of creatine levels in the brain (Singh, Haris et al. 2011). There is increasing evidence for creatine depletion in the brain of those with inborn errors of metabolism (IEM), which leads to clinical features of movement disorders, epilepsy and autism (Nasrallah, Feki et al. 2010). ^{1}H MRS shows low total creatine (tCr) concentration in the brain of those with known creatine deficiency syndromes (Nouioua, Cheillan et al. 2013). The improved spatial resolution of CrCEST compared to conventional spectroscopy techniques makes it an ideal tool for studying these disorders. Recent work has shown CEST imaging of brain creatine in a rat brain tumor model (Cai, Singh et al. 2015) that characterized the multiple exchangeable components through a simplified Z-spectral fitting method. The CEST peak observed at +2ppm was reduced in brain tumor tissue compared to normal tissue (**Figure 2.12**), and

continued to decrease with tumor progression. The 2ppm CEST peak also correlated with ^{1}H MRS-derived concentrations of creatine. This noninvasive way to look at Cr levels in the brain may aid in future developments for imaging of cancer and other brain diseases in which creatine metabolism is disrupted.

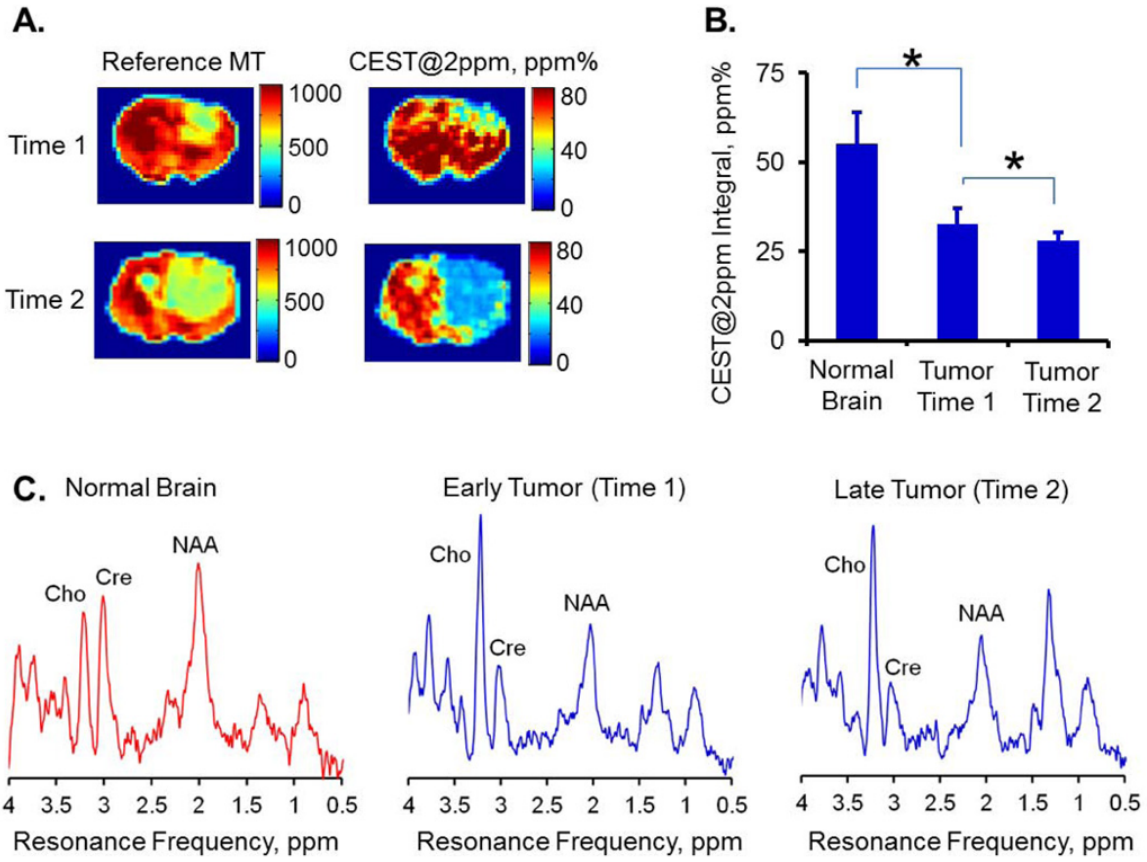

Figure 2.12 CrCEST of a rat brain tumor model. A, B) in the brain tumor region, the CEST signal at 2ppm was decreased compared with normal brain tissue and further reduced with tumor progression; C) ^{1}H MRS results show a similar trend for the creatine change (Cho=choline, Cre=creatine, NAA=N-acetylaspartic acid.). *(Reprinted with permission (Cai et al. NMR in biomed. 2015).)*

2.3 Preliminary Reproducibility Study

One of the primary goals of this dissertation was to build upon the work described in the previous sections. The studies in healthy humans indicated that CrCEST could be used to study the CK reaction *in vivo*, but an important step for biomarker development is application to a disease state. As a preliminary step to establish this technique as a method for examining metabolic dysfunction, an attempt was made to standardize the exercise protocol, fit recovery times and calculate time constants, and report on reproducibility. A small reproducibility study was performed on five subjects at 3T. Before adapting this technique for more widespread clinical use, a significant effort must be made to further establish reproducibility. A large-scale, well-controlled reproducibility study will be the subject of future work.

2.3.1 Methods

The pilot reproducibility study was performed on a 3T whole-body scanner (Siemens Prisma, Siemens Medical Systems, Erlangen, Germany), with a 15-ch knee coil.

Imaging parameters.

Imaging parameters consisted of the optimized CEST parameters for creatine at 3T, as determined by Kogan *et al*. (Kogan, Haris et al. 2013), and TR=5.6ms, TE=2.7ms, FOV=160x160mm^2, matrix size=128x128, B_{1rms}=2.25μT, flip angle=10°, slice thickness=10mm,t_{sat}=500ms, SHOT TR=5s.

MRI setup.

For the CrCEST studies described in the next few sections, the MRI setup was generally the following: subjects were placed feet-first, supine into the magnet with the knee coil

placed around the right calf, centering the widest part of the calf muscle at the center of the coil (**Figure 2.13**).

Figure 2.13 Coil positioning around the calf muscle for CrCEST imaging. The right foot was placed into a custom-built foot pedal, operated by a pneumatically controlled piston with constant pressure (set at 7.5 psi for all subjects). A 3-plane, localized image was acquired to determine optimal slice positioning, with the preferred slice containing the largest possible portion of the gastrocnemius muscles (Figure 2.14), determined from the axial image. *(Reprinted with permission (Kogan, Haris et al. 2014).)*

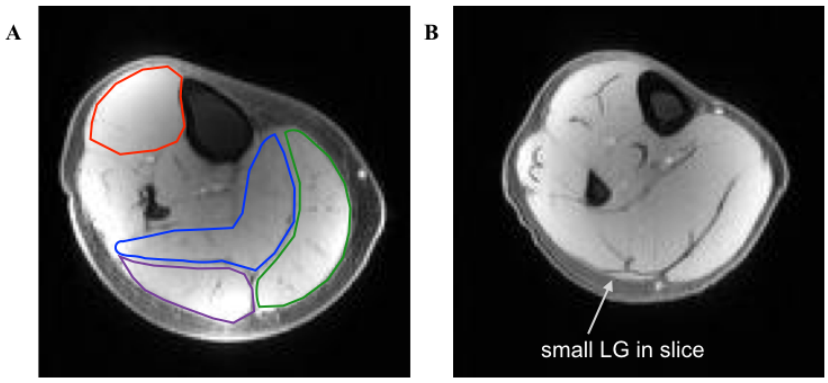

Figure 2.14 Anatomical, axial calf muscle image. A) optimal slice positioning with large areas of the soleus and gastrocnemius muscles. The anterior tibialis (AT) is outlined in red, the soleus (Sol) in blue, the medial gastrocnemius (MG) in green, and the lateral gastrocnemius (LG) in purple; B) poor slice positioning with a very small lateral gastrocnemius area visible. The plantar flexion exercise used in this study targets activation of the gastrocnemius muscles.

Building an MRI-compatible ergometer

For this study, and the subsequent clinical study in Chapter 3, a new MRI-compatible ergometer was built by Allen Bonner and Michael Carman at the University of Pennsylvania Research Instrumentation Shop (3620 Hamilton Walk, Room 75, Philadelphia, PA 19104 USA), with assistance from the author. This ergometer was updated from the previous version used in the initial 7T and 3T studies from **Sections 2.2.2** and **2.2.3** to include a piston made of aluminum, rather than stainless steel, in order to ensure MRI safety during the clinical study, as well as reduce any possible risk of artifact. The parts used to build the ergometer, a picture of the ergometer, as well as a schematic for the cylinder, are described and shown below.

The base of the ergometer was made out of white PVC purchased from MSC Industrial Supply (75 Maxess Road, Melville, NY 11747 USA). For reference, the MSC Part # is 93633188, and the material is Type I White PVC, with ½ inch thickness. The foot pedal was also built out of the same PVC. To accommodate the affected patient population who may have particular constrictions on leg/foot positioning, a new design feature was added to this ergometer (**Figure 2.15**) that allowed for adjustable leg positioning via a sliding mechanism on the custom base.

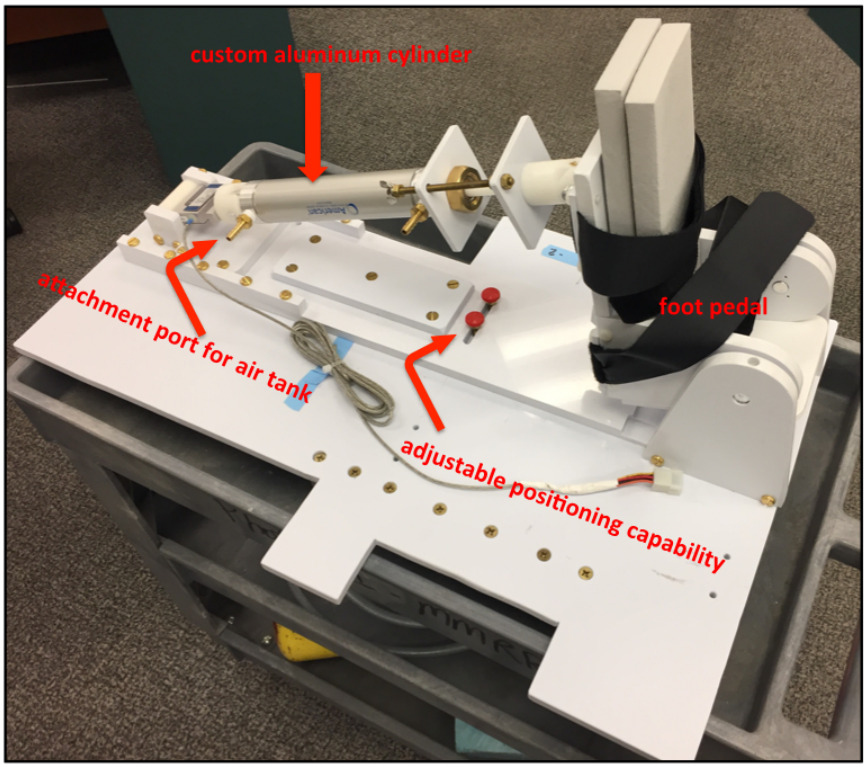

Figure 2.15 Custom-built MRI-compatible ergometer.

As mentioned, the ergometer used in studies by Kogan et al. contained a stainless steel pneumatic cylinder used to pressurize the foot pedal; in the new ergometer we worked with American Cylinder Co., Inc (481 Governors Highway, Peotone, Illinois 60468) to build a custom cylinder out of aluminum. This custom, round-body air cylinder consisted of a pivot-mounted, double-acting 1 ½" bore with a 6" stroke and was based on the cylinder available from McMaster-Carr (200 New Canton Way, Robbinsville NJ 08691-2343 USA) Part #6498K678 (**Figure 2.16**).

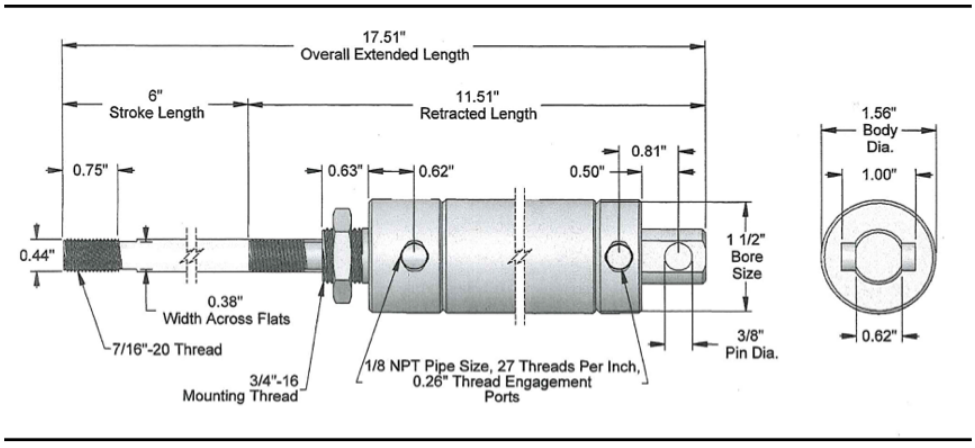

Figure 2.16 Schematic for pneumatic air cylinder.

The cylinder was attached to the PVC base with brass and nylon nuts/washers/screws from McMaster-Carr (Part #s: 98853A029, 92676A029, 92446A542, 93465A542, 92174A675, 9273K653, and 95606A130). The ergometer cylinder was connected to a pressured air tank (**Figure 2.17**) via ¼" (inner diameter) PVC tubing available from Kuriyama of America, Inc. (360 E. State Parkway Schaumburg, IL 60173-5335 USA),

part #: K3130-04X100, CLEARBRAID® K3130 Series BF Heavy Wall PVC Hose. The air tank was MRI-safe, equipped with an MRI-safe regulator (Part #AI USPEAMRI, Part # WESM1-950-PG), obtained from AirGas (Greater Philadelphia Metro Area, 850 April Hill Way, Harleysville PA 19438 USA) allowed for adjustable pressure; for the CrCEST clinical study this was kept at 7.5psi.

Figure 2.17 Air cylinder and pressure gauge.

Subjects.

Five healthy individual male subjects (age 25-40) were scanned on two separate days within 1 week. For this initial study of reproducibility, care was not taken to standardize

important clinical factors including fasting status, previous exercise, or time of day. A tightly controlled and standardized clinical study is presented in Chapter 3.

Imaging protocol.

Subjects were imaged at rest for two minutes in order to establish baseline CrCEST. They were then instructed to perform two minutes of plantar flexion at the rate of 45 flexions/minute, guided by a metronome to indicate when to push the pedal. Given the diameter of the piston (1.5in) and the pressure (7.5psi), we estimated the work/s for each flexion to be ~3.5watts. Obtaining precise work measurements in-magnet, over the course of dynamic exercise, will be the focus of future work. Following cessation of exercise, CrCEST images were acquired every 30s for a total of 8 minutes. The CEST contrast was calculated with in-house MATLAB routines as will be described in the next section. For every timepoint, the corresponding CrCEST image was overlaid onto an anatomical image. The individual muscle groups (anterior tibialis, soleus, medial gastrocnemius, and lateral gastrocnemius) were manually segmented in order to determine the CrCEST signal in each muscle. Time constants for recovery from each individual muscle group were then calculated from the segmented regions of interest (ROIs). We assessed the degree of agreement between i) resting, pre-exercise CrCEST % asymmetry (in medial gastrocnemius, lateral gastrocnemius, and soleus) and ii) post-exercise τCr, which was calculated from each individual muscle group and fit to an exponential decay. For preliminary reproducibility studies, the within-subject coefficient of variation between Day 1 and Day 2 measurements was calculated for each participant. All statistical

analyses were conducted using R (version 3.1.3), and statistical significance was taken as two-sided p-value of < 0.05.

CrCEST Post-processing

During this project, a graphical-user interface (GUI) for processing CrCEST exercise data was developed by Neil Wilson, a post-doctoral researcher in the Reddy lab with functionality input and initial testing from the author. This development was a vital part of the project, as it allowed data to be processed quickly and with minimal user input, thus limiting user bias or error. The GUI encompasses the MATLAB routines as written by Dr. Hariharan in the Reddy lab for analysis by Kogan *et al*., but incorporates a more sophisticated data-sorting routine (**Figure 2.18**) (Wilson 2016).

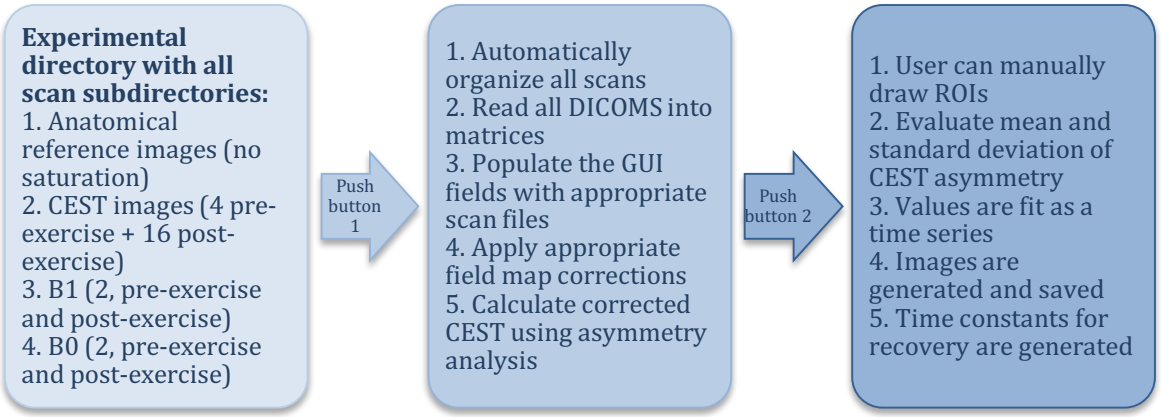

Figure 2.18 Flowchart for the GUI processing application.

Briefly, the GUI first organizes all the scans from the experiment, saved in DICOM

(Digital Imaging and Communications in Medicine) format, when the user selects the experimental directory in which each scan subdirectory exists. The subdirectories include a series of CEST-weighted images with saturation acquired symmetrically around 0 ppm (in the case of CrCEST: ±1.5-1.8-2.1 ppm), a series used to generate field maps, a series used to generate B_1+ maps, and a reference series with no saturation. Each series of scans is acquired both pre-exercise and post-exercise (in the case of CrCEST experiments). The individual scan subdirectories are automatically organized and populated (**Figure 2.19**).

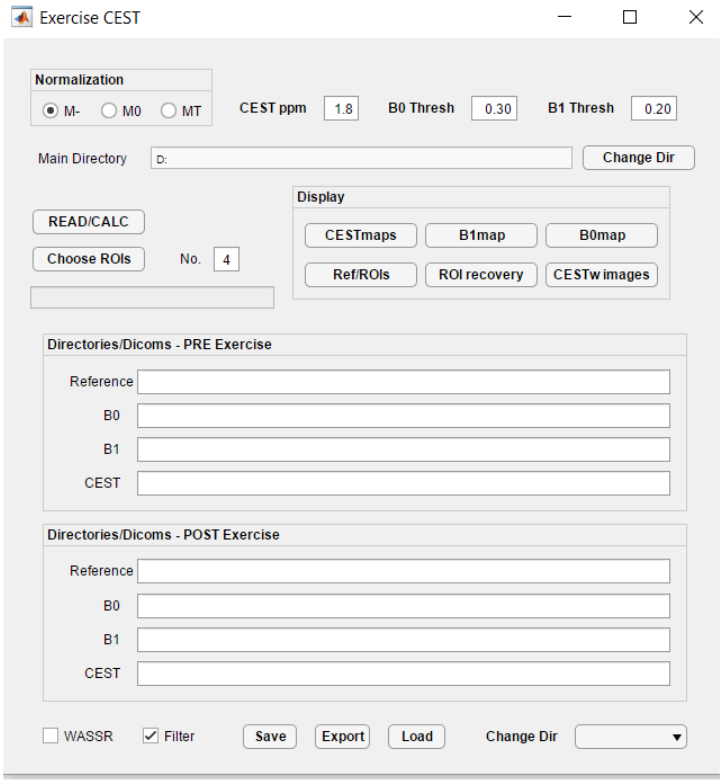

Figure 2.19 GUI interface for processing CrCEST exercise data.

With a single button push, all DICOMS are read into matrices, appropriate field map corrections are applied, and then both raw and corrected CEST maps are calculated using asymmetry analysis (**Figure 2.20**). B_0 correction is applied to the CEST maps by interpolating a partial z-spectrum of the CEST-weighted images, shifting the interpolated spectrum based on the measured inhomogeneity, and evaluating at the desired offset. B_1 inhomogeneity can then be normalized either with user-provided calibration parameters or assuming a linear dependence.

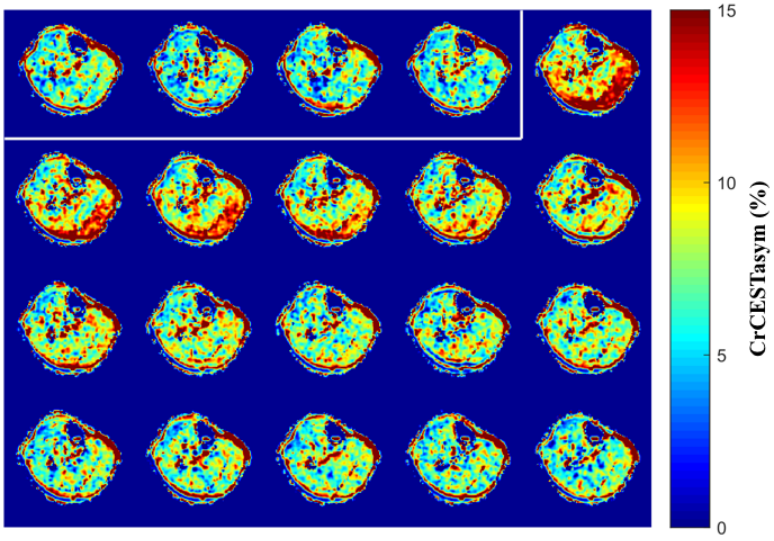

Figure 2.20 GUI image output. The GUI generates the CEST maps for the four baseline scans (inside the white box), and for the sixteen post-exercise scans acquired for this CrCEST experiment at 3T. The pixel intensity represents the CEST signal. An increase is observed in the gastrocnemius muscles of this subject following plantar flexion exercise.

A second button allows the user to manually draw ROIs on the reference images. From the individual ROIs (in the case of CrCEST in muscle, the four muscle groups referenced

above: AT, Sol, MG, and LG) the mean and standard deviation of the CEST asymmetry is evaluated in each before fitting those values as a time series (**Figure 2.21**).

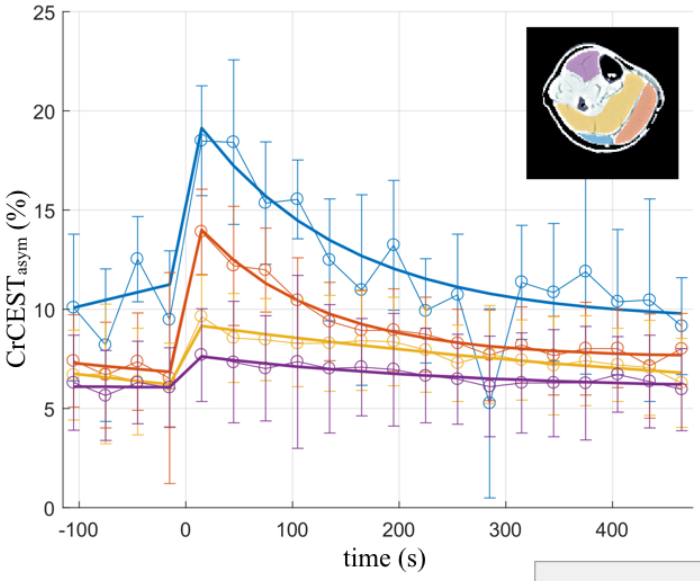

	LG	MG	Sol	TA
Increase	10.8237	7.3324	4.8732	1.8016
Recovery	137.6292	111.6101	658.3736	249.7269
Baseline	9.4266	7.5791	4.3965	5.9368
BiasSlope	0.0130	-0.0049	-0.0060	-2.4978e-04
Baseline	11.4461	6.7692	6.1252	6.0805
Voxels Post	149	698	1423	495
Voxels Pre	149	698	1423	495

Figure 2.21 GUI ROI calculation output. With the GUI, the user can manually draw regions of interest (ROIs), from which the average $CEST_{asym}$ is calculated separately for every acquired image. The values for each time point from each ROI are fit to a decaying exponential to calculate the time constant for creatine recovery. The second output box shows the initial baseline CrCEST values, the increase above baseline, the recovery time constant (s), and number of voxels included in the ROI.

With the GUI application, high quality CEST images as well as intermediate images such as B_0/B_1 field maps can be generated and saved in a variety of formats. This application allows for fast post-processing of clinical data.

2.3.2 Results

Results of the preliminary reproducibility study of CrCEST-based measures are shown in **Figures 2.22** and **2.23**. In 5 healthy individuals who underwent 3T CrCEST imaging on two separate days within one week, the mean within-subject coefficient of variation (COV) for resting CrCEST % asymmetry, an index of free creatine concentration, was 3.4%±1.4% (SEM) in lateral gastrocnemius, 8.2±1.8% in medial gastrocnemius, and 4.5±1.4% in soleus. All participants engaged the lateral gastrocnemius in exercise, and most engaged medial gastrocnemius, thus post-exercise τCr results are shown for these two muscle groups. Mean within-subject COV for τCr was 16.0±7.0% (SEM) in lateral gastrocnemius and 13.5±6.1% in medial gastrocnemius.

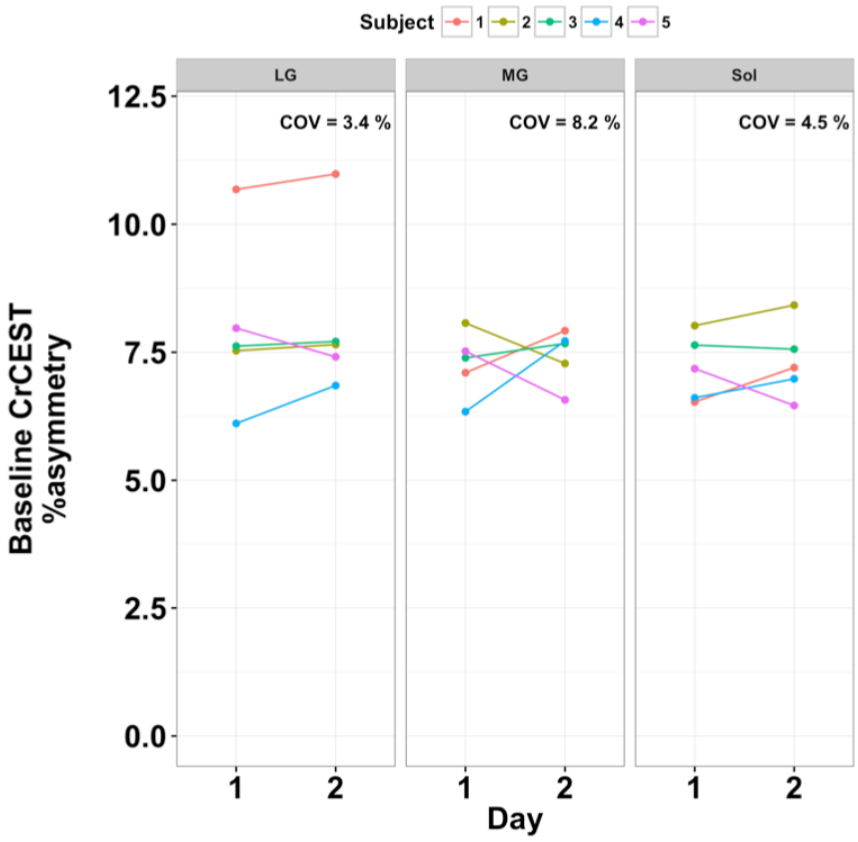

Figure 2.22 Reproducibility of baseline CrCEST % asymmetry, an index of free creatine concentration. For each of five subjects (shown in different colors), CrCEST measurements were obtained on a 3T MRI scanner on each of two different days, separated by less than one week. The degree of agreement between individual measurements and summary within-participant coefficient of variation (COV) estimates for these measurements are shown. LG = lateral gastrocenmius; MG = medial gastrocnemius; Sol = soleus.

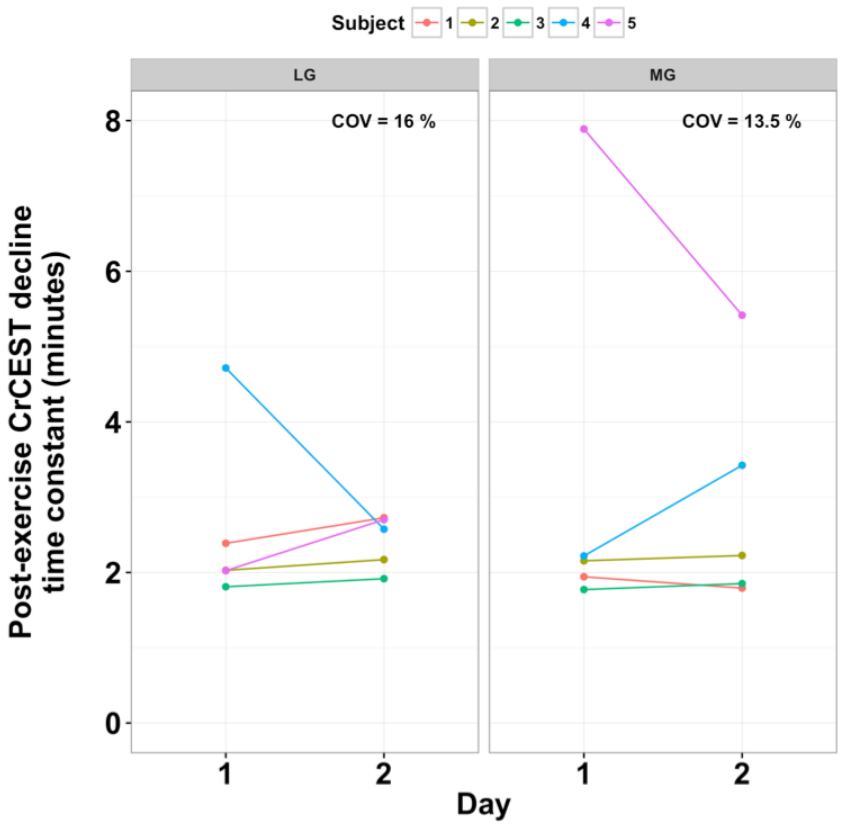

Figure 2.23 Reproducibility of post-exercise CrCEST decline exponential time constant (τCr), an index of free creatine concentration. For each of five subjects (shown in different colors), CrCEST measurements were obtained on a 3T MRI scanner on each of two different days, separated by less than one week. The degree of agreement between individual measurements and summary within-participant coefficient of variation (COV) estimates for these measurements are shown. LG = lateral gastrocenmius; MG = medial gastrocnemius; Sol = soleus.

2.3.3 Discussion

This pilot study was performed at 3T because MRI scanners at this field strength are more widely available, and thus may be used for future, larger studies and/or adapted for clinical use. As this study reflected a sample of convenience, it did not include standardized clinical factors including fasting status, previous exercise, or time of day.

For this reason, the resulting reproducibility estimates represent the lower bound of what would be achievable with careful standardization of pre-analytic factors in future CrCEST studies. Even without pre-analytic standardization of clinical factors and with the "low" MRI field strength (compared to 7T), we observed that a reasonable degree of consistency is achievable. A complete assessment of the reproducibility of CrCEST-based measures obtained at 7T of *in vivo* creatine metabolism would be beneficial in future before implementing multi-site studies, and will be the subject of future work.

2.4 Summary

This chapter has reviewed the development and application of CrCEST for studying muscle energetics *in vivo*. We have presented the original work from the Reddy lab to determine the exchange rates of creatine amino groups and locate their chemical shift with high-resolution NMR, and the demonstration that creatine can be imaged with the CEST technique in phantoms, without significant contribution from other associated metabolites. We have shown that it is feasible to establish CrCEST-derived measures of OXPHOS capacity in healthy human skeletal muscle, as well as preliminary applications in other key metabolic tissues, myocardium and brain. Together, these studies demonstrate the utility of the creatine CEST technique for studying metabolism in vivo, with high spatial resolution and enhanced sensitivity compared to traditional spectroscopic methods. For this dissertation work, we built upon those initial studies by: building a new ergometer with the specific needs of research subjects in mind (adjustability, comfort); developed the GUI for streamlined data processing including calculation of time constants of recovery; performing the reproducibility study to

demonstrate feasibility in translating the CrCEST technique to a larger clinical study. The next chapter will focus on the implementation of CrCEST in a clinical study of OXPHOS capacity in patients with mitochondrial dysfunction.

Chapter 3 - Application of CrCEST for measuring impaired muscle oxidative phosphorylation *in vivo*

3.1 Introduction

It is evident from the discussion in the previous chapters that mitochondrial dysfunction would have a wide-reaching and damaging effect on cells. Perhaps unsurprisingly, mitochondrial dysfunction is linked to many disease states. The first section of this chapter will review mitochondrial impairment in common diseases and specific disorders, beginning with a discussion of the mitochondrial genome. The rest of the chapter will focus our efforts to apply CrCEST to detect mitochondrial impairment in a population affected by mitochondrial dysfunction.

3.2 The mitochondrial genome and mutations that disrupt OXPHOS

In an effort to understand mitochondrial involvement across many pathophysiological conditions, the mitochondrial genome has become the subject of intense research, especially as inheritable diseases show more and more links to defects in mitochondrial, rather than nuclear DNA (Wallace 2005). In humans, the mitochondrial DNA (mtDNA) encodes for 13 polypeptides that are core components of the respiratory complexes that perform OXPHOS (summarized in **Table 3-1**):

Table 3-1 Respiratory complexes encoded for by mtDNA

Complex	# subunits encoded by mtDNA	Polypeptides encoded by mtDNA
I	7	ND1-4, 4L, 5 and 6
III	1	Cytochrome b
IV	3	COI-III
V	2	ATP6, 8

These complexes that have mtDNA-encoded polypeptides are the complexes that transport protons (Wallace 2010). The importance of OXPHOS is highlighted by that fact—the major components must coevolve to preserve OXPHOS function, and are all maintained on a single piece of DNA. All 13 of the mtDNA-encoded protein genes are translated on the mitochondrial ribosomes. Mitochondrial DNA also contains the genes for the 12S and 16S RNAs, and 22 tRNAs that are needed for protein synthesis (Wallace 2005). The majority of the genes (~1500, ~80 of which are for OXPHOS) of the mitochondrial genome are actually contained in the nuclear DNA (nDNA), and are translated on the cytosolic ribosomes before being imported into the mitochondria. Interestingly, Complex II is encoded for by nuclear DNA (nDNA) along with the rest of the mitochondrial proteins, including the mitochondrial DNA polymerase (POLG) subunits, and the RNA polymerase components and transcriptions factors (Friedman and Nunnari 2014). Mitochondrial metabolic enzymes and mitochondrial ribosomal proteins are also encoded for by nDNA.

Mitochondrial DNA is only inherited maternally, as the mtDNA in each cell's cytoplasm are transmitted through the oocyte's cytoplasm during fertilization. Often, mitochondrial dysfunction is due to mutated mtDNA. Mitochondrial DNA has a very high mutation rate (Schriner, Ogburn et al. 2000). This is due in part to the ROS production within the mitochondria. It is also a function of species survival mechanisms, which only invest enough energy in maintaining mtDNA long enough for the species to reproduce (Wallace 2007). When an mtDNA mutation first occurs, there's a mix of wild-type and mutant DNA present within the cell (heteroplasmy). When the cell goes on to divide, the daughter cell receives a random distribution of both the wild-type and mutant mtDNA. That means that over time, there can be an increase in the mutant mtDNA or in wild-type DNA until the genotype is fully mutant or wild-type. If the mutant mtDNA is in the majority, then mitochondrial dysfunction occurs with disease becoming progressively worse. Because the distribution of mtDNA is random during cell division, this means that both inheritance and expression of mtDNA mutations is highly variable. This, along with the fact that the total mitochondrial genome is encoded for by both mtDNA and nDNA, makes the overall genetics incredibly complicated (Wallace 2013). Likewise, the genetics of mitochondrial diseases are extremely complex, and a complete description is outside the scope of this work. However, we will discuss some of the common pathways and mechanisms of mitochondrial damage. A more complete discussion can be found in several reviews (Wallace 2013, Wallace 2013, Wallace 2015). Here, we will discuss the

types of mutations that can occur and provide brief descriptions of the resultant disorders (Wallace 1992).

3.2.1 Missense mutations

A missense mutation occurs when there is an amino acid substitution, and have been observed in most of the respiratory enzyme complex genes. These are largely associated with neurological and ophthalmological disorders. Commonly known phenotypes include Neurogenic muscle weakness, Ataxia, and Retinitis Pigmentosa (NARP), and Leber's Hereditary Optic Neuropathy (LHON). NARP is the result of a T→G transversion at np 8993, causing a leucine→ arginine at amino acid 156 in ATPase6 (Holt, Harding et al. 1990). This disease has a wide range of symptoms including ataxia, seizures, dementia, neuropathy, retinitis pigmentosa, and muscle weakness. LHON has several associated mtDNA mutations, and 50% of affected patients have a missense mutation at np 11778 causing an arginine→histidine at amino acid 340 on the ND4 protein (Wallace 1992). Several other missense mutations can occur, including in Complex I (ND1,2,4 and 5) and Complex III (cytochrome b) genes. The consequence of these mutations is inhibition of the electron transport chain (Wallace 1992). This causes blindness in affected patients from damage to the optic nerve, and can also cause cardiac conduction defects (Newman, Lott et al. 1991, Wall and Newman 1991).

3.2.3 Insertion-deletion mutations

Mitochondrial DNA deletions can cause ocular myopathy and Pearson Syndrome (Rotig, Cormier et al. 1990). These usually consist of a single mtDNA deletion, but the position and size can vary widely amongst patients. Most are spontaneous, rather than hereditary,

indicating developmental mutations. The deletions extend to the sequences required to initiate replication (Larsson, Holme et al. 1990). Ocular myopathy can include a wide range of symptoms: ophthalmoplegia, ptosis, and mitochondrial myopathy (chronic external ophthalmoplegia (CPEO), retinitis pigmentosa, lactic acidosis, hearing loss, ataxia, heart conduction defects, and dementia (Kearn-Sayre Syndrome or KSS) (Shanske, Moraes et al. 1990). mtDNA with deletion mutations replicate quicker than normal DNA, meaning that over time the deleted mtDNA is enriched (Wallace 1989). These diseases progress with age as the proportion of deletions increases. An interesting note about ocular myopathy patients is that muscle biopsies for cytochrome c oxidase show that activity varies from positive to negative along the length of individual muscle fibers. High concentrations of deleted mtDNA is found in cytochrome c oxidase-negative regions, with low levels of mRNA for the deleted genes (Shoubridge, Karpati et al. 1990).

3.2.4 Copy number mutations

Mitochondrial DNA depletion can cause lethal infantile respiratory failure, lactic acidosis, and muscle, liver, and kidney failure. Levels as low as 2% of normal mtDNA levels have been observed in lethal cases of mitochondrial myopathy (Moraes, Shanske et al. 1991).

3.2.5 Biogenesis mutations

Most biogenesis mutations are tRNA mutations, causing abnormal mitochondria and mitochondrial myopathy, which will be the subject of Chapter 3. tRNA mutations cause syndromes include: Myoclonic Epilepsy and Ragged-Red Fiber Disease (MERRF);

Mitochondrial Encephalomyopathy, Lactic Acidosis, and Stroke (MELAS); and Maternally Inherited Myopathy and Cardiomyopathy (MMC).

MERFF is a hereditary disease caused by mutations in mtDNA at np 8344, that changes a loop in $tRNA^{Lys}$ leading to reduced mitochondrial protein synthesis. It is associated with pleiotropic OXPPHOS defects in Complexes I and IV, which have a large proportion of mitochondrially-encoded subunits. General symptoms include myoclonic epilepsy and mitochondrial myopathy. More severe symptoms can include hearing loss, dementia, cardiomyopathy, renal dysfunction, and respiratory failure (Shoffner, Lott et al. 1991). OXPHOS capacity in MERFF patients is partially correlated with the percentage of mutant mtDNA. Enzyme levels in MERFF patients fall as they age, meaning that an affected individual could have normal phenotype at a young age when the initial OXPHOS defects are above tissue expression thresholds. Once aging has caused an expression below threshold, clinic symptoms are then observed. This explains why many mtDNA mutations manifest later in life and progressively worsen.

MELAS primarily results from a mutation at np 3243 that changes a loop in $tRNA^{Leu(UUR)}$, thereby inactivating the transcriptional terminator, and reducing efficiency of translation by changing the ratio of mitochondrial rRNA and mRNA transcripts (Goto, Nonaka et al. 1990, Penn, Lee et al. 1992). It leads to Complex I defects. Symptoms include stroke-like episodes and mitochondrial myopathy. Like MERFF, effects of MELAS worsen with age.

MMC is due to a mutation at np 3260, also in $tRNA^{Leu(UUR)}$, in the stem of the anticodon loop. This creates an OXPHOS defect in both Complex I and IV.

3.3 Mitochondrial involvement in other disorders

3.3.1 Mitochondrial impairment in cancer

As discussed in Chapter 1, cancer cells utilize aerobic glycolysis preferentially over mitochondrial oxidative metabolism. Mitochondrial biology is being increasingly targeted in the search for new cancer therapies. The importance of mitochondria in so many key biological processes means that any disruption to mitochondrial function could contribute to the change from normal cell to rapidly proliferating cell. Mutations in mitochondria DNA have been observed in cancer cells, leading to altered mitochondrial metabolism that can give rise to cancer cell adaptability. For example, there are now well-established defects in the genes for succinate dehydrogenase (SDH), respiratory complex II, associated with cancer (Jackson, Nuoffer et al. 2014).

Though Warburg initially predicted that cancer cell reliance on aerobic glycolysis was due to mitochondrial defect, we now understand that intact mitochondrial function is necessary for cancer cells to grow rapidly and spread. Certain cancer cell signaling pathways affect mitochondrial function by shifting metabolism from oxidative to glycolytic, which enables cancer cells to shuttle nutrients toward anabolic processes. Transcription factors activated in cancer can alter mitochondrial function such that substrates are provided to the TCA cycle for producing increased citrate, which

contributes to lipid biogenesis and protein modifications, further allowing cells to grow and proliferate. Reactive oxygen species are also involved in cancer progression as reduced mitochondrial function drives increased lactate production that is then used as fuel for the oxidative metabolism, providing the energy for tumor growth. There is extensive research on the link between mitochondria function and cancer, and so development of noninvasive techniques for measuring mitochondrial function is clearly beneficial to the field of cancer research.

3.3.2 Mitochondrial impairment in neurodegenerative disease and aging

In neurodegenerative diseases such as Alzheimer's, there is evidence of impaired mitochondrial OXPHOS, and mtDNA rearrangements have been found in brain tissue. Mitochondrial reactive oxygen species play an important role in aging and degenerative diseases. An increased rate of ROS production ultimately causes cell loss, like neuronal degeneration, associated with age-related disease. Although there is a wide array of clinical features between individual neurodegenerative disorders, impaired mitochondrial energy metabolism is a convincing link, considering that neurons are highly dependent on oxidative energy metabolism (Coskun, Wyrembak et al. 2012).

3.3.3 Mitochondria in cardiovascular disease and diabetes

Impaired mitochondrial function has clear consequences for cardiac tissue, as cardiomyocytes have huge concentrations of mitochondria due to their intense energy demands. Mitochondria and disruptions to bioenergetics are implicated in cardiovascular disease. Mitochondrial function has also been investigated in the context of type 2 diabetes. Diabetes mellitus is a chronic disease wherein the body develops resistance to

insulin, and consequently has elevated levels of glucose in the blood. Studies of diabetes in skeletal muscle have shown that there is reduced glucose uptake into the muscle that contributes to insulin resistance when fatty acid intermediates interfere with insulin signaling (Kelley, He et al. 2002). This eventually leads to reduced glucose transporter in the muscle cells. Ultimately, this means that there is reduced fat oxidative capacity and mitochondrial metabolism. This is supported by the observation that there is a reduction in some OXPHOS-protein encoding genes within diabetic skeletal muscle. There is also evidence of mitochondrial dysfunction in cardiac tissue of type 2 diabetes patients. There is an increased risk to diabetes patients of developing heart failure (Schrauwen-Hinderling, Kooi et al. 2016).

The widespread occurrence of mitochondrial dysfunction in a variety of disease states provides motivation to study it *in vivo*. Although the CrCEST technique is novel and still requires further work to become a sophisticated method for clinical use, the goal for this dissertation was to demonstrate initial feasibility for using CrCEST to identify mitochondrial impairment *in vivo*.

3.4 ^{31}P MRS and mitochondrial impairment

Before moving on to discuss CrCEST in a clinical population, we will briefly review the current "gold standard" of ^{31}P MRS for assessing mitochondrial function in disease states. In individuals with clinical mitochondrial diseases, ^{31}P MRS studies have shown deficient OXPHOS capacity, i.e., rate of mitochondrial ATP production, as evidenced by a delay in PCr recovery post-exercise (Arnold, Taylor et al. 1985, Matthews, Allaire et al. 1991, Penn, Lee et al. 1992, Chance and Bank 1995). ^{31}P MRS has been validated using

multiple *in vitro* techniques, including measurement of state III respiration in isolated mitochondria (Lanza, Bhagra et al. 2011). ^{31}P MRS can also demonstrate the pro-mitochondrial effect of exercise training (Kent-Braun, McCully et al. 1990). This method has been adapted for use in diverse subjects, and has also yielded insights with respect to insulin sensitivity, growth, and exercise capacity in children (Fleischman, Kron et al. 2009, McCormack, McCarthy et al. 2011, McCormack, McCarthy et al. 2013). Several limitations for ^{31}P MRS were discussed in Chapter 2. One of the most impactful limitations is that ^{31}P MRS has poor spatial resolution. In genetic or acquired defects of muscle OXPHOS, where muscle fiber type is closely coupled to metabolism and function (Shoffner, Lott et al. 1991, Proctor, Sinning et al. 1995, Zierath and Hawley 2004, Horiuchi, Fadel et al. 2013), it would clearly be advantageous to measure OXPHOS from individual muscle groups. With the current ^{31}P MRS technology (Parasoglou, Xia et al. 2013), (as of this writing), this would require multiple bouts of exercise to obtain separate voxels for each muscle group. It would therefore require wait times in between each round of exercise to ensure full recovery. The time that would be necessary for such a paradigm clearly isn't feasible within a clinical MRI timeframe, especially in subjects suffering from mitochondrial disease, which often includes exercise intolerance (Andreu, Hanna et al. 1999). In addition to study of primary mitochondrial dysfunction ^{31}P MRS studies have shown a decreased PCr/ATP ratio, a marker of cardiac energy status, in cardiac studies of diabetes. As diabetes, cardiovascular disease, and associated clinical features are some of the costliest burdens on healthcare systems, it is imperative to continue developing techniques for assessing diabetic mitochondrial function *in vivo*. ^{31}P

MRS has shown delayed recovery in PCr after exercise in diabetic skeletal muscle (Bajpeyi, Pasarica et al. 2011), indicating that the CrCEST technique would be a good candidate for future work in areas of research that extend beyond primary mitochondrial disease.

3.5 Clinical MRI Study

3.5.1 Motivation

In Section 3.2, we reviewed the systemic defects in mitochondrial bioenergetics that occur in primary mitochondrial disorders, as well as in various age-related human disorders, including diabetes mellitus, cardiovascular disease, neurodegenerative diseases, and cancer (Wallace 2013). Energy deficiency is most apparent in tissues with large energy demand, including exercising skeletal muscle. As we saw in Chapter 2, with CEST the creatine content can be simultaneously measured in every muscle of a leg *in vivo* (Kogan, Haris et al. 2013, Kogan, Haris et al. 2014). The capacity of mitochondrial OXPHOS is reflected in the exponential time constant for the decline in Cr post-exercise (τCr), which corresponds inversely to the exponential time constant for the recovery of PCr post-exercise (τPCr) observed with ^{31}P-MRS. The previous studies were carried out in healthy volunteers, and so the next step was to perform these experiments in subjects with known mitochondrial dysfunction. **The objective of this proof-of-principle study was to determine whether CrCEST-derived measurements of post-exercise exponential decline in free creatine were prolonged in individuals with primary genetic-based mitochondrial diseases, as compared to matched healthy volunteers** (DeBrosse, Nanga et al. 2016). By demonstrating the feasibility of this technique in

affected individuals, we sought to highlight the utility of CrCEST as a longitudinal biomarker of *in vivo* tissue OXPHOS capacity in patient populations.

3.5.2 Methods

Design and Subjects. Individuals ranging in age from 18-65 years were recruited for this study. They all had a clinical diagnosis of a disorder of the mitochondrial respiratory chain. We prioritized eligible subjects with disorders confirmed to be caused by pathogenic mtDNA or nDNA mutations, affecting subunits or assembly of mitochondrial respiratory chain complexes and are associated with known clinical/pathological features. These disorders included chronic progressive external ophthalmoplegia (CPEO), Kearns–Sayre syndrome, mitochondrial encephalomyopathy, lactic acidosis and stroke-like episodes (MELAS), mitochondrial encephalopathy and ragged red fibers (MERRF), neuropathy, ataxia and retinitis pigmentosa (NARP) or Leigh syndrome (Stacpoole, deGrauw et al. 2012). Individuals affected with Friedreich's ataxia were also studied. Friedreich's ataxia is a mitochondrial disease in which ATP production is reduced due to GAA triplet repeat expansions in frataxin, a mitochondrial protein involved in the formation of iron sulfur clusters necessary for respiratory chain complex function (Kaplan 1999). Finally, individuals were studied who had genetic deficiency of isoforms of succinate dehydrogenase (SDH), respiratory chain complex II (Jackson, Nuoffer et al. 2014, Alston, Ceccatelli Berti et al. 2015).

Although collectively these subjects are heterogeneous with respect to their specific molecular diagnoses, the functional consequence of their defects is expected to include a deficiency in skeletal muscle OXPHOS capacity. Because multiple studies have used ^{31}P-

MRS to demonstrate impaired skeletal muscle OXPHOS in individuals with type 2 diabetes mellitus (Scheuermann-Freestone, Madsen et al. 2003), individuals with diabetes mellitus were excluded, to avoid confounding results. In order to verify diabetes status, fasting blood glucose hemoglobin A1c was measured on the day of the study. Healthy, non-diabetic volunteers were recruited to generate a cohort that was balanced compared to the group of affected individuals with respect to age, sex, and body mass index (BMI). Thirty-one subjects were enrolled, 1 was excluded because of a pigmented tattoo, 2 were claustrophobic and 1 failed to remain still, thus data are presented on 27 subjects with available MRI data.

Additional Metrics. Height and weight were measured according to standard procedures. Blood specimens were collected after an overnight fast and processed using standard techniques for glucose, lipid panel, and hemoglobin A1c (HgbA1c). Several validated instruments were used to measure important potential covariates affecting mitochondrial function, including self-reported physical activity, using the Chronic Renal Insufficiency Cohort (CRIC) Physical Activity Questionnaire (Feldman, Appel et al. 2003), mitochondrial disease severity, using the Newcastle Mitochondrial Disease Adult Scale (NMDAS) (Bates, Hollingsworth et al. 2013), and physical function and overall health, using the NIH Patient-Reported Outcomes Measurement Information System (PROMIS) Global Health and Physical Function Scales (Barile, Reeve et al. 2013). Subjects were sedentary from the moment they arrived on the morning of the visit prior to the MRI scan. All were also instructed to refrain from intensive exercise for at least 24 hours prior

to the MRI. All MRI scans were performed in the early afternoon, approximately 4 hours after a standardized breakfast.

Magnetic resonance imaging and magnetic resonance spectroscopy. CrCEST images were acquired on a 7T whole body scanner (Siemens Medical Systems, Erlangen, Germany). Imaging experiments were performed using a 28-channel ^{1}H knee coil. The MRI setup was as described in Chapter 2: subjects were placed feet-first, in the supine position, into the magnet with the knee coil placed around the right calf, centering the widest part of the calf muscle at the center of the coil (**Figure 2.11**). The right foot was placed into a custom-built, MR-compatible ergometer consisting of a foot pedal connected to a pneumatically controlled piston set at constant pressure (**Figure 2.13**). Anatomical, axial images were acquired of the right calf in all subjects to find the optimal slice positioning and to be used in post-processing for segmentation (**Figure 2.12**). Subjects were imaged at rest for two minutes in order to establish baseline CrCEST. CrCEST imaging parameters were as follows: saturation pulse: 500 ms, $B1_{rms}$ = 123 Hz (2.9μT), slice thickness = 10 mm, flip angle = 10°, TR = 6.0 ms, TE = 2.9 ms, field of view = 160 x 160 mm^2, matrix size = 128 x 128, SHOT TR=5s. Four baseline images were acquired over 2 minutes with a temporal resolution of 30s, followed by 2 minutes of mild plantar flexion exercise. Exercise was performed in the magnet using the ergometer, with pressure held constant at 7.5 psi for all subjects. The subjects were instructed to fully depress the ergometer pedal at a constant rate of 90 flexions over two minutes (1 flexion every ~1.3s), with an average work/s of ~3.5 watts per flexion. Adherence was assured by 1) verbally coaching the exercise with aid of a metronome to keep accurate

pace, and 2) visually confirming pedal depression *via* a direct read-out of a dynamometer. For this study, we did not attempt to vary exercise intensity according to each participant's capacity. Rather, percentage change in CrCEST in response to this light, standardized exercise workload was an important outcome of interest assessed in affected individuals as compared to controls. To test for the potential effects of differential exercise intensity on τCr, percentage change in CrCEST was included as a covariate in statistical models.

Immediately after exercise, 8 minutes of CrCEST images were acquired with the same 30s resolution (16 consecutive images). Image processing was performed using in-house MATLAB scripts and a processing GUI (described in the next section). WASSR (Kim, Gillen et al. 2009) maps to correct B_0 inhomogeneities, and B_1 maps were acquired pre- and post-exercise, and used to generate corrected CrCEST images as described for the previous muscle study in healthy subjects. As described in Chapter 2, CrCEST contrast was computed by subtracting the normalized magnetization signal at the Cr amine proton frequency (Δω = +1.8 ppm), from the magnetization at the corresponding reference frequency on the opposite side of the water resonance (-Δω). CrCEST changes in individual muscle groups pre- and post-exercise were determined by overlaying CrCEST maps onto manually segmented anatomic images. τCr was calculated using a MATLAB fitting routine ('nlinfit') by fitting the CrCEST contrast decay post-exercise from each segmented muscle to a single exponential of the form $Cr(t) = a(1) * e^{\frac{-t}{a(2)}} + a(3)$ where a(1), a(2), and a(3) are constants and t=time.

^{31}P MRS was performed with a 7-cm diameter ^{1}H/^{31}P dual tuned surface coil using an un-localized free induction decay (FID) sequence with the following parameters: number of points = 512, averages = 5, and TR = 2.4 s, with 4 "dummy scans" per acquisition, in order to obtain similar time resolution to the CrCEST image acquisition (21.6s vs. 30s). ^{31}P MRS spectra were phased and baseline corrected and fitted using nonlinear least squares method with Lorentzian functions. τPCr was determined by calculating the area under the curve for the PCr peak from every FID post-exercise, and fitting the recovery to a single exponential equation of the form $PCr(t) = a(1) * (1 - e^{\frac{-t}{a(2)}}) + a(3)$ where a(1), a(2), and a(3) are constants and t=time. The intracellular pH was calculated as described by McCormack *et al*. for both pre- and post-exercise by comparing the chemical shift difference between the PCr peak and the Pi peak using $pH = 6.85 + log[(\partial - 3.56)/(5.64 - \partial)]$ (McCormack, McCarthy et al. 2011).

Statistics. Clinical characteristics were summarized with standard descriptive statistics and compared between affected and unaffected individuals using parametric or non-parametric methods, as appropriate given the variable distributions. Pearson's correlation coefficient was used to measure the correlation between continuous variables. τCr was log-transformed due to non-normal distribution, and linear mixed effects regression analyses were performed to assess the effect of mitochondrial disease status on τCr measured over time, adjusted for other clinical covariates in separate statistical models. These statistical models account for within-subject correlation due to repeated measures by including a subject-specific random effect. In each model, mitochondrial disease status and muscle group analyzed are included as fixed effects along with others as

follows: in Model 1) no additional fixed effects, i.e., mitochondrial disease status and muscle group alone; in Model 2) mitochondrial disease status, muscle group, resting CrCEST, and percent change in CrCEST; in Model 3) mitochondrial disease status, muscle group, and total self-reported total physical activity (MET-hours per week); and in Model 4) mitochondrial disease status, muscle group, age, and gender.

The independent effects of clinical covariates on log-transformed resting CrCEST were also assessed using mixed-effects regression analysis. Included in these models were: between-subject variability (random effect), mitochondrial disease status, and muscle group (fixed effects) and, as additional fixed effects, as follows: Model 1) no additional factors, i.e., mitochondrial disease status and muscle group alone; in Model 2) mitochondrial disease status, muscle group and, total physical activity (MET-hours per week); and in Model 3) mitochondrial disease status, muscle group, age, and gender. All of the clinical covariates were considered as fixed effects in separate models as shown to avoid over-fitting given the sample size and number of observations in this study.

For physical activity, total physical activity (MET-hours per week) was chosen because of the statistically significant differences observed between affected individuals and healthy volunteers on this covariate. Aikaike Information Criterion (AIC) and Bayesian Information Criterion (BIC) values are calculated for each model to permit goodness-of-fit comparisons. Sensitivity analyses were performed by analyzing subsets of participants with established genetic diagnoses (i.e., excluding the 2/13 individuals with variants of uncertain significance), and also the subset of subjects not taking creatine (i.e., excluding

the 3/13 subjects with mitochondrial disease who were taking supplemental creatine), to assess for any potential associated source of bias.

For analyses of the association between habitual intentional exercise, collected via validated instrument, with imaging parameters, non-parametric correlation analyses were performed on non-normally distributed variables, stratified by i) group (all participants, participants with mitochondrial disease, participants without mitochondrial disease); ii) imaging technique (CrCEST, ^{31}P MRS), and iii) parameter type (baseline, post-exercise decline or recovery time constant). Both nominal and Bonferroni-adjusted statistical significance thresholds are shown. Since we observed an association between intentional exercise and both baseline and post-exercise CrCEST values, we also performed a sensitivity analysis, repeating mixed-effects regression analyses with intentional exercise (MET-hours per week) in place of total physical activity (MET-hours per week) in the models to determine the independence of effects. For preliminary reproducibility studies, the within-subject coefficient of variation between Day 1 and Day 2 measurements was calculated for each participant. All analyses were conducted using R (version 3.1.3), and statistical significance was taken as two-sided p-value of < 0.05.

Study approval. This cross-sectional, observational study enrolling both cases and controls was performed under an approved Institutional Review Board protocol of the University of Pennsylvania (www.clinicaltrials.gov: NCT02154711) and was conducted according to the Declaration of Helsinki. Written, informed consent was obtained from all participants prior to their inclusion in the study.

3.5.3 Results

Subject characteristics (n=27). Characteristics are summarized in **Table 3-2**. The two groups were well-matched with respect to age, sex, and body mass index (BMI). Some affected individuals were non-ambulatory, as reflected in overall group differences in weekly physical activity (MET-hours, p=0.049). Self-reported physical activity (**A**) is estimated over the 4 weeks prior to the study. A higher NMDAS score (**B**) indicates more severe disease. Symptoms were estimated by the subject over the 4 weeks prior to the study. Although the NMDAS scale has not been validated in healthy adults, we administered it here to indicate the degree of comparable symptom burden. A higher NIH PROMIS physical function score (**C**) indicates better physical function. A higher NIH PROMIS global health score (**D**) indicates better overall health. All statistically significant differences are shown in bold text. IQI = interquartile interval; MET = metabolic-equivalent (*p<0.05, **p<0.01, ***p<0.001 for difference between subjects with mitochondrial disease versus healthy volunteers by two-sample t-test, Wilcoxon rank sum test, or chi-square test, as appropriate).

Table 3-2 Subject characteristics

	Mitochondrial Disease (n=13)	Healthy Volunteers (n=14)
Sex (% female, n)	62 (8)	57 (8)
Age (years)	42.1 ± 12.9	45.5 ± 13.7
Body Mass Index (kg/m^2)	26.5 ± 6.7	25.9 ± 4.7
Underweight, <18.5 (%, n)	8 (1)	0 (0)
Normal weight, 18.5 – 24.9 (%, n)	38 (5)	43 (6)
Overweight, 25 – 30 (%, n)	31 (4)	43 (6)
Obese, >30 (%, n)	23 (3)	14 (2)
Self-reported Population Ancestry (% white, n)	92 (12)	100 (14)
Laboratory Studies		
HgbA1c (%)	5.00 ± 0.28	5.22 ± 0.30
Glucose (mg/dL)	85 ± 8	90 ± 9
Cholesterol, total (mg/dL)	190 ± 36	188 ± 43
Triglycerides (mg/dL)	116 ± 56	121 ± 75
High-density Lipoprotein (HDL, mg/dL)	52 ± 12	52 ± 10
Low-density Lipoprotein (LDL, mg/dL)	115 ± 26	112 ± 38
Self-reported Physical Activity[A]		
Total (hrs per wk)	7.3 ± 4.5	9.3 ± 3.3
Total (MET-hrs per wk)	**16.4 ± 11.8***	**25.4 ± 10.5**

	Mitochondrial Disease (n=13)	Healthy Volunteers (n=14)
Moderate-heavy activity, >3 METs) (hrs per week)	**0.9 ± 1.3***	**2.5 ± 1.9**
Moderate-heavy activity, >3 METs (MET- hrs per week)	**4.8 ± 6.4***	**11.2 ± 8.3**
Intentional exercise (hrs per wk)	**0.7 ± 0.8***	**1.5 ± 0.9**
Intentional exercise (MET-hrs per week)	4.0 ± 4.9	7.2 ± 3.8
Newcastle Mitochondrial Disease Adult Scale[B]		
0, asymptomatic (%, n)	**8 (1)***	**38 (5)**
1 – 5, mild (%, n)	**38 (5)***	**64 (9)**
6 – 20, moderate (%, n)	**46 (6)***	**0**
>20, severe (%, n)	**8 (1)***	**0**
NIH PROMIS Physical Function Scale[C]	**41.8 ± 7.6*****	**56.8 ± 2.9**
NIH PROMIS Global Health Scale[D]	**32.8 ± 4.2*****	**39.5 ± 3.0**

Results of CrCEST imaging, including: resting-state CrCEST values, % change post-exercise, and τCr; and ^{31}P MRS measurements of: baseline ratio of PCr to inorganic phosphate (PCr/Pi), % change of PCr, pH, and τPCr, are provided in **Table 3-3**. Not all subjects completed ^{31}P MRS imaging given time constraints (1), as CrCEST was prioritized (n=11 mitochondrial disease subjects, n=12 control subjects). No attempt was made to exclude any outlier values for this summary table. Means are presented ±SD except where indicated in cases of non-normal variable distributions, in which case

medians ±IQI are shown. The Shapiro-Wilk test was used to assess normality of distribution except a normal distribution was assumed for normalized scales. All statistically significant differences are shown in bold text. IQI = interquartile interval; MET = metabolic-equivalent (*p<0.05, **p<0.01, ***p<0.001 for difference between subjects with mitochondrial disease versus healthy volunteers by two-sample t-test, Wilcoxon rank sum test, or chi-square test, as appropriate).

Table 3-3 Creatine CEST imaging results

	Mitochondrial Disease (n=13)	**Healthy Volunteers (n=14)**
Resting CrCEST (% asymmetry, index of free creatine concentration)		
Medial gastrocnemius (median, IQI)	11.5 (11.1 – 12.4)	12.1 (11.7 – 12.7)
Lateral gastrocnemius (median, IQI)	11.5 (11.0 – 12.1)	11.5 (11.0 – 14.0)
Soleus (median, IQI)	12.3 (11.7 – 13.5)	12.4 (11.7 – 13.2)
% change in CrCEST with exercise (% change from baseline)		
Medial gastrocnemius	32.9 ± 15.6	23.7 ± 15.3
Lateral gastrocnemius	37.8 ± 22.7	29.9 ± 20.1
Soleus	21.2 ± 11.1	17.4 ± 9.6
τCr (in minutes)		
Medial gastrocnemius (median, IQI)	**2.2* (1.7 – 2.9)**	**1.4 (0.8 – 1.7)**
Lateral gastrocnemius (median, IQI)	2.0 (1.2 – 3.6)	1.4 (0.6 – 2.0)
Soleus (median, IQI)	2.1 (1.7 – 3.7)	1.7 (1.1 – 2.7)
^{31}Phosphorus-Magnetic Resonance Spectroscopy Parameters[1]		

	Mitochondrial Disease (n=13)	Healthy Volunteers (n=14)
Baseline PCr/Pi ratio	8.5 ± 2.2	9.3 ± 2.1
% change in PCr with exercise (% from baseline)	22.8 ± 11.2	16.2 ± 15.9
Resting pH	7.09 ± 0.04	7.08 ± 0.04
End-exercise pH	**6.99 ± 0.05***	**7.04 ± 0.06**
τPCr (in minutes; median, IQI)	1.10 (0.87 – 1.83)	0.77 (0.69 – 1.40)

Diagnostic details for individuals with mitochondrial disease (n=13) are provided in **Table 3-4**. Subjects had clinical and/or biochemical features consistent with disorders of the mitochondrial respiratory chain, and molecular diagnoses as noted. In 2/13 subjects, the identified mutations were variants of uncertain significance (VUS), with causality as yet to be established.

Table 3-4 Diagnoses in individuals with mitochondrial respiratory chain diseases

Diagnoses (n=13)
Chronic progressive external ophthalmoplegia-plus: ***C10ORF12*** (c.1110C>G; p.F370L), 1 subject; mtDNA deletions on muscle biopsy, 2 subjects
MFN2 (c.1699A>G; p.M567V)
POLG (c.2209G>C; p.E441G); m.13064T>C (***ND5)***
MELAS: m.3288A>G (tRNA-Leu)

Diagnoses (n=13)
MELAS-like: m.1630A>G (tRNA-Val)
GJB1 (c.14G>T; p.G5V); VUS
SYNE1 (c.1162G>A; p.D388N, c.7066C>T; p.L2356F); VUS
Friedreich Ataxia: ***FXN*** GAA triplet expansions (2 subjects; triple expansion lengths 454/777 and 525/1050 for these, respectively)
SDHD (c.209G>T; pR70M)
SDHB (c.600G>T; pW200C)

Physical activity, which is expected to impact muscle OXPHOS capacity, was included as a covariate in mixed-effects regression models (**Table 3-5**). Each of the models include the subject from which the measurement was obtained (as a random effect) and the clinical covariates shown (as fixed effects). For all models, n=26 subjects contributing a total of 74 muscle-specific post-exercise CrCEST recovery estimates (i.e., if subjects exercised more than one muscle group, then more than one post-exercise recovery time constant could be calculated); the mixed effects modeling strategy accounts statistically for the effects of obtaining multiple measurements per subject. Coefficients are represented as standardized β values, with their corresponding p values; statistically significant results are shown in bold text. Aikaike Information Criterion (AIC) and Bayesian Information Criterion (BIC) values are calculated for each model to permit goodness-of-fit comparisons (NS = not significant; AIC = Aikaike Information Criterion; BIC = Bayesian Information Criterion).

Table 3-5 Mixed effects regression models of log-transformed post-exercise CrCEST decline time constant (τCr, in minutes)

	Model 1 standard-ized β (p-value)	Model 2 standard-ized β (p-value)	Model 3 standard-ized β (p-value)	Model 4 standard-ized β (p-value)
Mitochondrial disease status	**0.32 (0.017)**	**0.26 (0.045)**	**0.40 (0.007)**	**0.32 (0.020)**
Muscle group				
Lateral gastrocnemius (reference)	-	-	-	-
Medial gastrocnemius	0.06 (NS)	0.09 (NS)	0.06 (NS)	0.05 (NS)
Soleus	0.14 (NS)	0.22 (NS)	0.15 (NS)	0.14 (NS)
CrCEST parameters				
Baseline CrCEST	-	-0.03 (NS)	-	-
% change CrCEST with exercise	-	0.21 (NS)	-	-
Total physical activity (MET-hours/wk)	-	-	0.19 (NS)	-
Age	-	-	-	0.002 (NS)
Sex	-	-	-	0.09 (NS)
AIC	224	236	231	236
BIC	238	254	248	254

Exponential time constant for the decline in Cr post-exercise (τCr). **Figure 3.1** shows representative images of resting CrCEST levels (panels A and E), and τCr (panels B and F). **Figure 3.1C-D and G-H** shows the corresponding post-exercise CrCEST and PCr

profiles. Overall, subjects in both groups demonstrated a measurable muscle group-specific increase (range 17.4% to 32.9%) in CrCEST signal after exercise. τCr was not normally distributed.

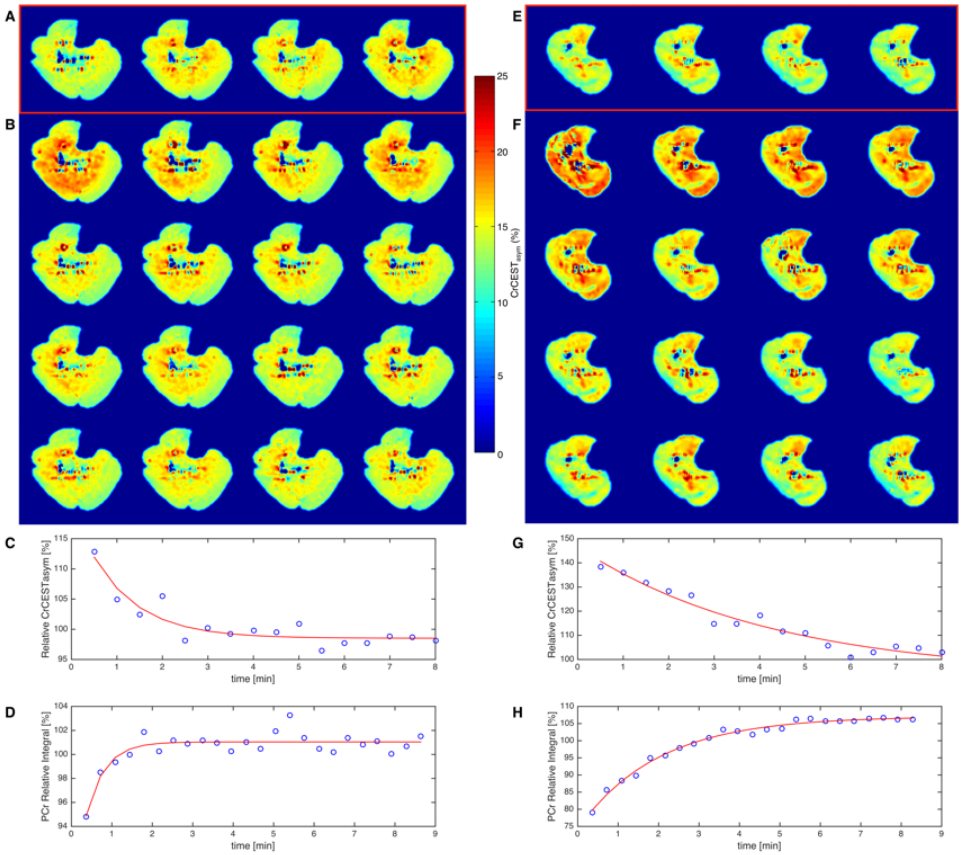

Figure 3.1 Example resting and post-exercise CrCEST recovery images and summary curves. A-D (left) is from a heathy 21-year-old female, and Figure 3.1E-H (right) is from a 21-year-old female with an mtDNA mutation, m.1630G>A (tRNA-Val) with hearing impairment, short stature, and stroke(Glatz, D'Aco et al. 2011). Panels 1A and 1E show the sequential resting CrCEST images (one image every 30 seconds at rest), overlaid on the manually segmented, anatomical axial calf muscle image, for the healthy and affected individuals, respectively. The images encompass the muscle region of the right calf. The intensity of the color in each image, as shown on the color bar, is in proportion to the CrCEST % assymetry signal, reflecting the amount of free creatine. Resting CrCEST appears lower in the affected individual as well (e.g., in soleus, CrCEST asymmetry is 11.1% in the affected individual versus 13.2% in healthy individual). Panels 3.1B and 3.1F show the sequential post-exercise images (one image every 30 seconds after cessation of exercise) in the healthy and affected individuals, respectively.

Both subjects exercised, as indicated by the increase in free creatine, although the specific muscle groups used differ, and the % change in CrCEST for the same exercise was higher in the affected individual (e.g., in the soleus, 28% in the affected individual versus 10% in the healthy control). By ~2 minutes post-exercise, the healthy volunteer's CrCEST image resembles the baseline image, but in the affected individual, τCr is prolonged (e.g., in the soleus, 5.9 minutes in the affected individual versus 1.1 minutes in the healthy control). Panels 3.1C and 3.1G show the post-exercise CrCEST signal recovery summarized over the anatomic region corresponding to the approximate area of the surface ^{31}P-MRS coil. Panels 3.1D and 3.1H show the post-exercise PCr signal recovery in this same anatomic region. In both modalities, prolonged post-exercise recovery is observed in the affected individual relative to the healthy individual. *(Reprinted with permission (DeBrosse et al. 2016).)*

Non-parametric bivariate analysis of the medial gastrocnemius (MG) (**Table 3-3**) showed a significant difference between affected individuals and controls in τCr ($p=0.026$). Other muscle groups were less consistently exercised in all subjects, and results for τCr were in a similar direction, but did not achieve statistical significance. Mixed-effects regression models of τCr (log-transformed given non-normal distribution, **Table 3-5**) demonstrated a statistically significant effect of mitochondrial disease in all models. None of the other clinical covariates examined showed a statistically significant effect. **Figure 3.2** is a box plot for post-exercise CrCEST exponential time constants (τCr), which are longer in individuals with mitochondrial diseases, though an overlap is observed even after adjustment for covariates. Log-transformed τCr values were used in statistical modeling. Mean model-derived estimates illustrate the longer τCr for individuals with mitochondrial diseases as compared to controls ($p=0.017$ in Model 1).

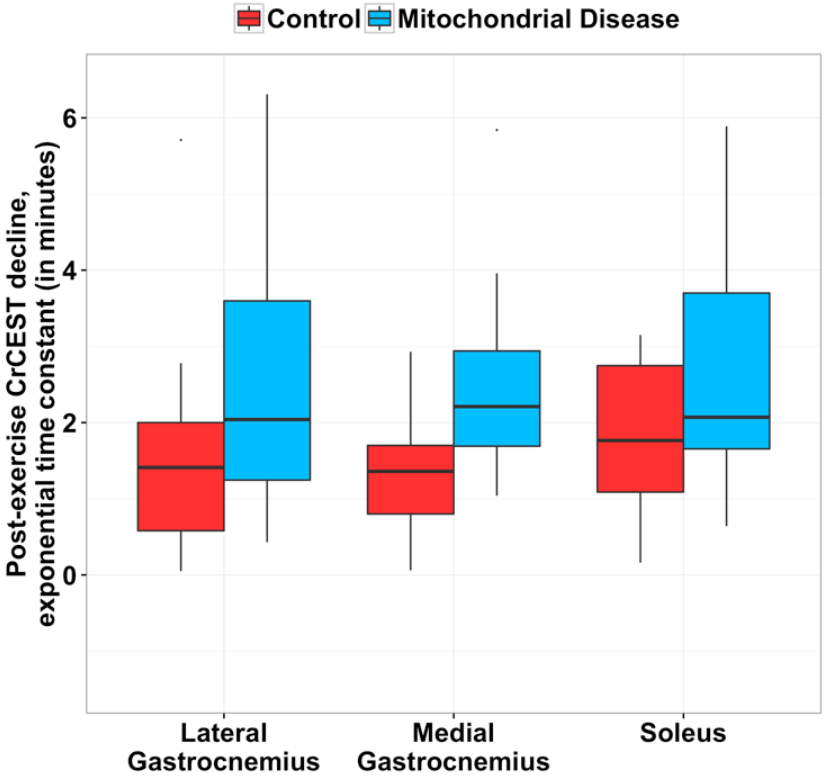

Figure 3.2 ***Box plots for post-exercise CrCEST exponential time constant (τCr), an index of skeletal muscle OXPHOS capacity (red = control, blue = mitochondrial disease).*** The horizontal line corresponds to the median, the lower and upper margins of the boxes correspond to the 25%ile and the 75%ile, respectively, and whiskers show 1.5 x the inter-quartile interval (IQI). The distribution of τCr is not normal so non-parametric statistics are shown here. Log-transformed τCr values were used in statistical modeling. A prolonged τCr values corresponds to less OXPHOS capacity. Mitochondrial disease increases τCr by 0.32 SDs (p=0.017). The range of values shown results in part from the inter-subject variability of the which muscle groups were engaged in exercise and to what extent. *(Reprinted with permission (DeBrosse et al. 2016).)*

Resting CrCEST. Resting CrCEST, an index of free creatine concentration, showed no statistically significant differences between affected and unaffected individuals (**Table 3.3** and **Table 3-6**). In **Table 3-6**, each of the models include the subject from which the

measurement was obtained (as a random effect) and the clinical covariates shown (as fixed effects). For all models, n=27 subjects contributing a total of 84 muscle-specific post-exercise CrCEST recovery estimates (i.e., if subjects exercised more than one muscle group, then more than one post-exercise recovery time constant could be calculated); the mixed effects modeling strategy accounts statistically for the effects of obtaining multiple measurements per subject. Coefficients are represented as standardized values, with their corresponding p values; statistically significant results are shown in bold text. Aikaike Information Criterion (AIC) and Bayesian Information Criterion (BIC) values are calculated for each model to permit goodness-of-fit comparisons (NS = not significant; AIC = Aikaike Information Criterion; BIC = Bayesian Information Criterion).

Table 3-6 Mixed effects regression models of log-transformed resting CrCEST (% asymmetry)

	Model 1 standard-ized β (p-value)	**Model 2 standard-ized β (p-value)**	**Model 3 standard-ized β (p-value)**
Mitochondrial disease status	-0.16 (NS)	-0.07 (NS)	-0.17 (NS)
Muscle group			
Lateral gastrocnemius (reference)	-	-	-
Medial gastrocnemius	0.06 (NS)	0.06 (NS)	0.06 (NS)
Soleus	**0.35 (0.0029)**	**0.35 (0.0028)**	**0.35 (0.0031)**
Total physical activity (MET-hours/wk)	-	0.23 (0.07)	-

	Model 1 standard-ized β (p-value)	Model 2 standard-ized β (p-value)	Model 3 standard-ized β (p-value)
Age	-	-	-0.11 (NS)
Sex	-	-	0.01 (NS)
AIC	-72	-62	-52
BIC	-57	-45	-33

With respect to muscle group, resting CrCEST, as reflected in % CrCEST asymmetry per unit muscle area, was highest in soleus as compared to either lateral gastrocnemius (LG) (p=0.0058) or MG (p=0.030) by post-hoc Tukey testing in Model 1, with similar results in Models 2 and 3. A positive association was observed between self-reported total physical activity (MET-hours per week) and a higher resting CrCEST, but this result did not reach statistical significance in the multivariable models (standardized β=0.23, p=0.070). Several subjects with mitochondrial myopathy had very low levels of CrCEST, hence the large variance in signal, but overall we did not observe a statistically significant difference between affected individuals and unaffected volunteers in resting CrCEST.

^{31}P MRS. Four subjects (2 of 13 mitochondrial disease, 2 of 14 healthy controls) completed only CrCEST imaging, and not ^{31}P MRS. These participants elected not to re-enter the scanner for the second same-day study. To examine the association between ^{31}P MRS and CrCEST measurements in the remaining participants, a CrCEST region of interest was defined corresponding to the leg area (including portions of multiple muscle

groups) assessed by the ^{31}P MRS surface coil. A positive within-subject association was observed between log-transformed τPCr and log-transformed τCr (Pearson's correlation coefficient=0.43, p=0.046) (**Figure 3.3**).

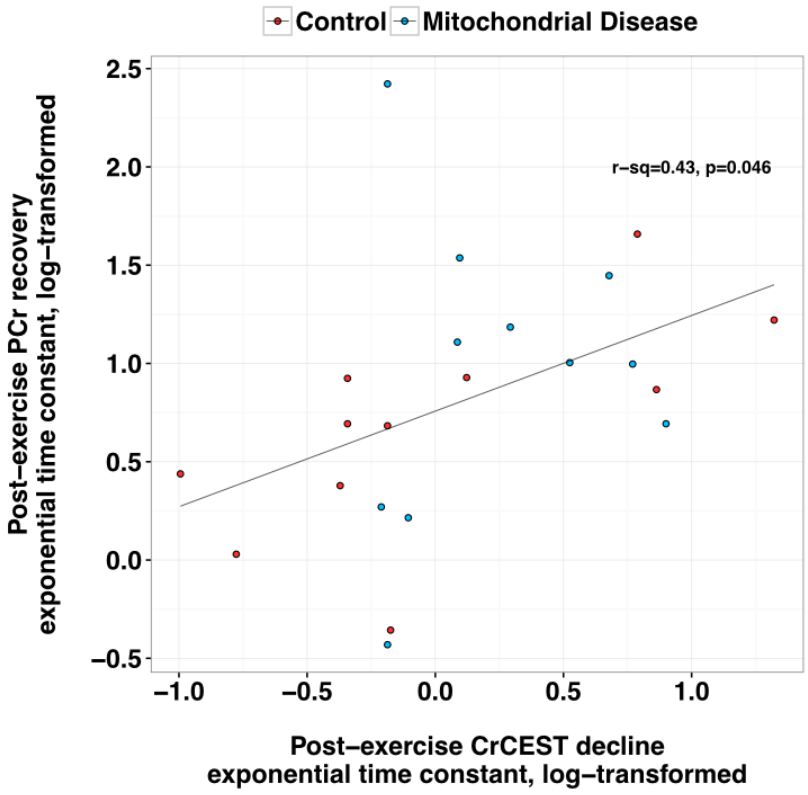

Figure 3.3 τPCr/τCr correlation. Correlation between the recovery time constants for PCr derived from spectroscopy and Cr derived from CEST.

Within-subject log-transformed resting PCr/Pi was also positively associated with log-transformed resting CrCEST (Pearson's correlation coefficient=0.44, p=0.023). In addition, prior studies with ^{31}P MRS (Tarnopolsky and Parise 1999) have posited that reduced creatine transport into muscle and lower resting creatine may be related to post-

exercise PCr recovery. Indeed, we found that lower resting CrCEST (log-transformed) was associated with prolonged τPCr (log-transformed), with Pearson's correlation coefficient -0.42, p=0.046. While resting pH did not differ between mitochondrial disease subjects and unaffected controls, post-exercise pH in the affected group was slightly lower: 6.99 versus 7.04 ($p<0.05$; Table 1). This likely reflects the exercise-induced increased % change in Cr or PCr in affected individuals, though the latter changes are highly variable and do not reach statistical significance at the group level.

Anatomic Variation. **Figure 3.4** shows images from the right leg of a 60-year-old man with chronic progressive external ophthalmoplegia due to a pathogenic autosomal dominant mutation in *C10ORF2* (c.1110C>G; p.F370L).

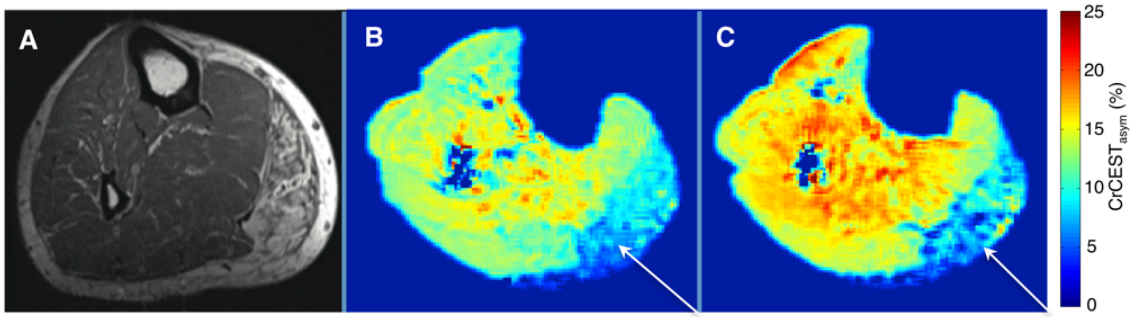

Figure 3.4 Example of muscle group-specific metabolic variation captured by CrCEST. Images from the right leg of a 60-year-old subject with chronic progressive external ophthalmoplegia due to a mutation in C10ORF12 (c.1110C>G; p.F370L). Panel 3.4A is from a 1.5-Tesla clinical image, and shows nearly complete fatty replacement of the MG. In Panel 3.4B, the corresponding area is indicated with a white arrow on a resting CrCEST image obtained at 7.0-Tesla. The intensity of the color in each image, as shown on the color bar, is in proportion to the CrCEST % assymetry signal reflecting the amount of free creatine. In Panel 3.4B, resting CrCEST signal is much lower in the MG than in other muscle groups. Post-exercise, there is no increase in CrCEST signal in this

region (Panel 3.4C, white arrow). These images illustrate the advantage of performing muscle group-specific measurements in individuals with mitochondrial diseases, given the anatomic variation that can occur in metabolic derangement (Zierath and Hawley 2004). *(Reprinted with permission (DeBrosse et al. 2016).)*

Sensitivity Analyses. Main analyses were repeated while excluding specific subsets of participants to ensure the robustness of the main findings. Exclusion of either participants with "non-classic" mitochondrial diseases, including those with SDH mutations (2 of 13) and sequence variants of uncertain significance (2 of 13), or participants taking supplemental creatine (n=3) did not substantially alter the finding of prolonged τCr in affected individuals (effect of mitochondrial disease, standardized $\beta = 0.27$, $p=0.060$ and $\beta = 0.32$, $p=0.027$, respectively).

Intentional Exercise. **Figure 3.5** is a correlogram showing the relationships between intentional exercise, baseline CrCEST or PCr/P_i, and post-exercise τCr or τPCr. Non-parametric bivariate correlation analyses were performed for these non-normally distributed outcomes. To allow for the possibility of muscle group differences in response to habitual intentional exercise, muscle groups were analyzed separately.

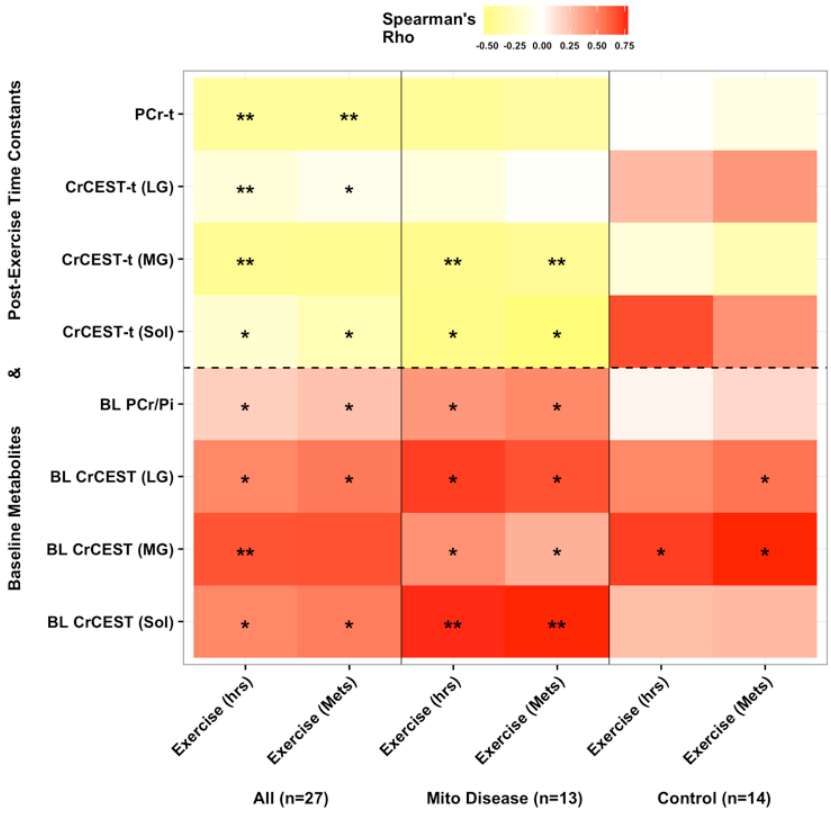

Figure 3.5 Correlogram of the association between intentional exercise) and measured imaging parameters (expressed either as hours per week, reflecting time spent exercising, or Mets per week, reflecting both time and intensity spent exercising) and measured imaging parameters. The results of non-parametric correlation analyses are shown for all participants (first group of two columns), for participants with mitochondrial disease (second group of two columns), and for control participants (third group of two columns). Groups are separated by horizontal black lines. Four of the rows indicate baseline (i.e., pre-exercise) metabolite concentration: baseline CrCEST in the soleus, medial gastrocnemius, and lateral gastrocnemius, and PCr/P_i in the region of interest captured by ^{31}P MRS. A higher resting CrCEST or PCr/P_i value suggests more bioenergetic capacity at rest. Four of the rows indicate post-exercise exponential time constants for return to baseline of CrCEST in soleus, medial gastrocnemius, and lateral gastrocnemius, and PCr in the region of interest captured by ^{31}P MRS. A longer post-exercise time constant to return to baseline suggests decreased OXPHOS capacity. The two types of imaging assessment (baseline, post-exercise) are separated by the dashed horizontal black line. As indicated by the color bar, positive associations are shown in red, and negative associations in yellow. The degree of statistical significance is given by the asterisk; one asterisk indicates nominal p value < 0.05; two asterisks indicates Bonferroni p value < 0.05 (adjusted for the 16 comparisons

shown for each group). BL = baseline; Sol=soleus; MG=medial gastrocnemius; LG=lateral gastrocnemius. *(Reprinted with permission (DeBrosse et al. 2016).)*

Overall, more habitual intentional exercise, whether measured in hours per week (reflecting time spent exercising) or MET-hours per week (reflecting both time and intensity of exercise) was associated with higher resting bioenergetic capacity, represented either by CrCEST or PCr/P_i. This positive association between habitual intentional exercise and resting CrCEST persisted after statistical correction for multiple testing in the medial gastrocnemius. In all of the muscle groups tested, and using both imaging modalities, more habitual intentional exercise was associated with shorter post-exercise return of metabolites (free Cr, PCr) to baseline, suggestive of more robust OXPHOS capacity.

In individuals with mitochondrial disease, there was a positive association between habitual exercise and baseline CrCEST, particularly in the soleus. Also, there was a positive association between habitual exercise and more rapid decline of CrCEST post-exercise, suggestive of greater OXPHOS capacity, particularly in medial gastrocnemius. In control participants, we observed a nominal association between between habitual exercise and resting CrCEST in two muscle groups, but we did not detect an association between usual habitual exercise and imaging estimates of OXPHOS capacity. Finally, given the observed associations of imaging parameters with intentional exercise, we repeated mixed effects regression analyses of the effects of covariates on τCr and resting CrCEST with intentional exercise (MET-hours per week) in place of total physical activity (MET-hours per week), results in **Table 3-6**.

Table 3-7 Mixed effects regression models including the association of intentional exercise with (Model 1) log-transformed post-exercise CrCEST decline time constant (τCr, in minutes)*, an index of skeletal muscle OXPHOS capacity, where prolonged τCr suggests lower OXPHOS capacity and (Model 2) log-transformed resting CrCEST (% asymmetry), an index of free creatine concentration, where higher CrCEST may reflect greater bioenergetic capacity at rest.*

	Model 1 standardized β (p-value)	**Model 2 standardized β (p-value)**
Outcome	**τCr**	**CrCEST**
Mitochondrial disease status	**0.32 (0.027)**	-0.08 (NS)
Muscle group		
Lateral gastrocnemius (reference)	-	-
Medial gastrocnemius	0.05 (NS)	0.06 (NS)
Soleus	0.14 (NS)	**0.35 (0.0027)**
Intentional Exercise (MET-hours/wk)	-0.004 (NS)	0.23 (0.064)

**Each of the models include the subject from which the measurement was obtained (as a random effect) and the clinical covariates shown (as fixed effects). For Model 1, n=26 subjects contributing a total of 74 muscle-specific post-exercise CrCEST recovery estimates were included (i.e., if subjects exercised more than one muscle group, then more than one post-exercise recovery time constant could be calculated); the mixed effects modeling strategy accounts statistically for the effects of obtaining multiple measurements per subject. For Model 2, n=27 subjects contributing a total of 84 muscle-specific CrCEST measurements were included; the mixed effects modeling strategy accounts statistically for the effects of obtaining multiple measurements per subject. Coefficients are represented as standardized β values, with their corresponding p values;

statistically significant results are shown in bold text. NS = not significant; AIC = Aikaike Information Criterion; BIC = Bayesian Information Criterion.

The independent association of mitochondrial disease status with prolonged τCr was confirmed even when habitual intentional exercise was included in the model in place of total physical activity (for effect of mitochondrial disease, standardized β=0.32, p=0.027). Intentional exercise was independently associated with higher resting CrCEST, but this association did not achieve statistical significance (for effect of habitual intentional exercise, standardized β=0.23, p=0.064).

Effects of age on CrCEST? Due to decreased oxidative capacity in muscle tissue with age (Boffoli, Scacco et al. 1994, Wei, Lu et al. 1998, Conley, Jubrias et al. 2000) we looked for a correlation with age and CrCEST signal in resting muscle, expected to be inversely related (i.e., less signal correlates to less [Cr] in older muscle), and for age and τCr of recovery, expected to be proportionally related (i.e., younger muscle recovers more quickly). Although there is some muscle-group specific association (**Figures 3.6 and 3.7**) with resting CrCEST and τCr, the small sample, as well as the age distribution precluded any statistically significant findings.

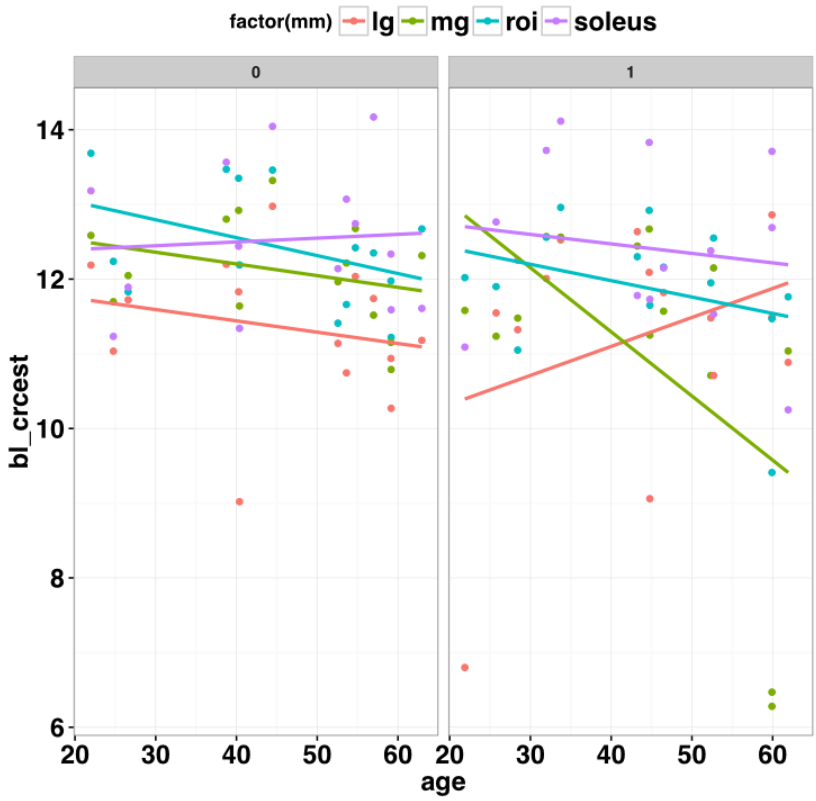

Figure 3.6 Resting-state CrCEST vs. age. The baseline, resting-state CrCEST values (in %, denoted "bl_crcest") were plotted vs. age of controls (0) and affected subjects (1). While some association between resting CrCEST and certain muscle groups and age is observed, no statistical significance was reached.

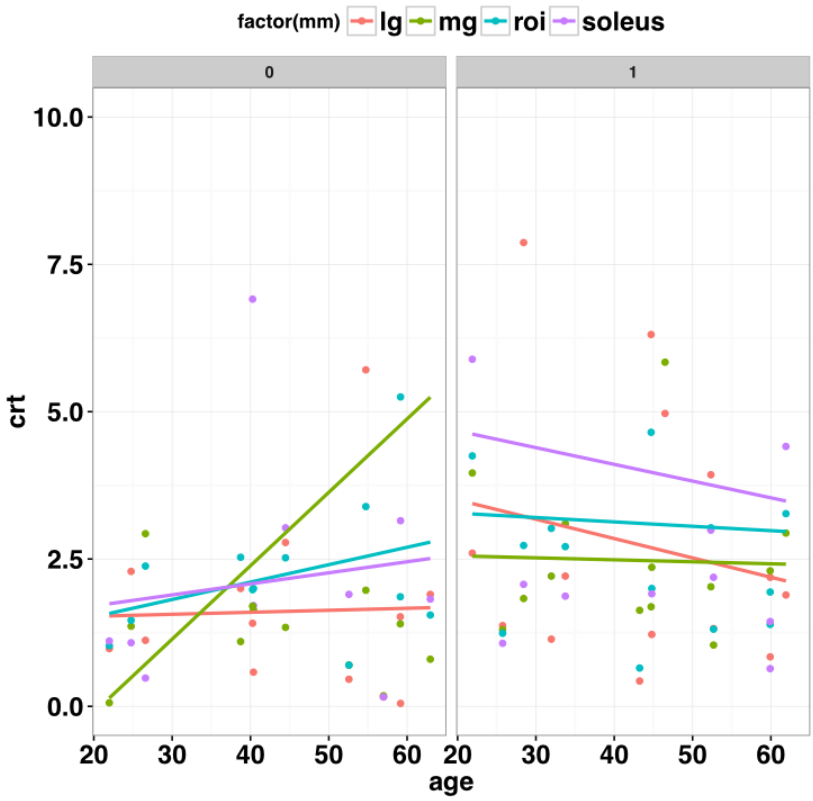

Figure 3.7 ***The τCr values*** **(in min, denoted "crt")** ***plotted vs. age of controls (0) and affected subjects (1).*** While some association between τCr and certain muscle groups and age is observed in the control group, no statistical significance was reached. A small number of recovery time constants that were greater than 10min were excluded from this analysis.

3.5.4 Discussion

From the clinical study described above, we have determined that incorporating CrCEST in the imaging-based investigation of OXPHOS capacity in individuals with primary mitochondrial disorders yields several benefits. As noted in the introduction for this chapter, the CrCEST technique provides a measurement of free creatine, while spectroscopic methods such as ^{31}P MRS and proton (^{1}H) MRS can only measure PCr and

total creatine (tCr), respectively. The ability to measure free creatine is useful both in static measurements of resting-state skeletal muscle, as well as in dynamic exercise studies. As research into mitochondrial and other metabolic diseases expands, there may be increased need for the CrCEST technique. For example, resting levels of free creatine may be altered in subjects with neuromuscular diseases who could potentially have reduced creatine transport into muscle (Tarnopolsky and Parise 1999, Tarnopolsky, Parshad et al. 2001). Or, as Cr monohydrate supplements are often used for therapeutic purposes in mitochondrial disorders (Parikh, Saneto et al. 2009), it may prove useful in future studies to estimate free creatine with CrCEST as a potential factor influencing clinical response to treatment. While we did observe low levels of resting creatine, as measured by CrCEST, in several subjects with mitochondrial myopathy, the overall group difference between affected and unaffected individuals overall did not reach statistical significance. The subjects' self-reported physical activity (MET-hours per week) appeared to be positively associated with resting CrCEST levels, but the association did not reach statistical significance in mixed effects regression analyses including all muscle groups (standardized β=0.23, p=0.070, **Table 3.7**). In bivariate correlation analyses of individual muscle groups (**Figure 3.5**), subjects' habitual intentional exercise was positively associated with higher levels of resting CrCEST and more rapid return of CrCEST to baseline post-exercise in the medial gastrocnemius. A positive association between exercise and CrCEST parameters was also evident in mitochondrial disease patients analyzed separately.

In Chapter 2, we made the case that another major advantage of CrCEST is its high spatial resolution, which provides muscle group-specific estimates of relative free creatine concentrations. The capacity to make muscle group-specific measurements is critical in studies of metabolic disorders, because different muscle groups may have distinct metabolic and contractile properties, including both mitochondrial density and the relative ratio of type I oxidative fibers to type II glycolytic fibers (Zierath and Hawley 2004). Differences in muscle fiber type may contribute to metabolic disease; there is some evidence that the ratio of glycolytic/oxidative enzyme activities is related to insulin resistance in obese patients and some diabetic populations (Simoneau, Colberg et al. 1995, Simoneau and Kelley 1997). The data for all subjects at rest indicates that soleus has a higher CrCEST % asymmetry, suggesting that this muscle has a higher concentration of free creatine than either the medial or lateral gastrocnemius. This finding might be expected given the higher proportion of oxidative fibers in soleus in previous, biopsy-based studies (Johnson, Polgar et al. 1973, Trappe, Trappe et al. 2001). Muscle groups may respond differently to genetic or acquired mitochondrial impairment, as illustrated in **Figure 3.4**. In this subject, who had fatty replacement specific to the medial gastrocnemius muscle, we also observed very low resting-state CrCEST in the medial gastrocnemius, and no subsequent increase following exercise. CrCEST may prove a useful tool to mechanistically investigate response of specific muscle groups to exercise therapy. The nuances of this subject's muscle composition may have been missed had they participated only in a spectroscopy study.

After dynamic exercise, τCr (representing the decline in CrCEST post-exercise) was **prolonged** in affected subjects. Prolonged τCr reflects decreased skeletal muscle OXPHOS capacity in individuals with primary mitochondrial diseases relative to the cohort of healthy volunteers. This statistically significant difference persisted even after accounting for other clinical covariates that could affect OXPHOS capacity. The benefits of CrCEST's high spatial resolution were again evident in the exercise component of the study, as the method provided information about all muscle groups in the exercising limb. Historically, in ^{31}P MRS exercise studies, specific muscles were targeted if the entire exercising limb could not be included in the area assessed by the coil. Unfortunately, if a particular subject did not utilize the targeted muscles, no recovery time constant could be calculated. Individuals with muscle diseases may need to use additional or alternate muscle groups to complete an exercise task. With the CrCEST technique, post-exercise recovery time constants can be calculated for each muscle group that is deployed.

It is interesting to note that although there were directionally consistent group-specific differences between τCr and τPCr obtained from the two separate bouts of exercise (**Figure 3.3**), and a positive within-subject correlation between τCr and τPCr, τCr values tended to be longer in this study. We speculate that this could be attributed in part to the differences in modalities, in which the surface coil used for ^{31}P-MRS provides an unlocalized signal, whereas the volume coil used for CrCEST imaging enables exact slice selection. An intensive comparison of the two methods, in which slices for CrCEST are chosen based on the excitation profile of the surface coil, will be the focus of a future study. We have also speculated that the increased blood flow after exercise, which could

change the water content in the muscle tissue, could also affect the measurement of the CEST signal. The effects of protocol design and other factors on τCr will also be the focus of future investigation. Nonetheless, the results of our initial study further illustrate several benefits of including CrCEST in studies of skeletal muscle metabolism. CrCEST may ultimately provide insight into the aspects of phosphocreatine shuttle that cannot be studied with ^{31}P MRS alone. Indeed, as has been previously suggested, the capacity to estimate resting creatine levels is also important in subjects with mitochondrial myopathies who may have altered creatine transport into muscle (Tarnopolsky and Parise 1999).

Exercise, particularly at high intensity, is one of the most potent signals for mitochondrial biogenesis (Little, Gillen et al. 2011, Little, Safdar et al. 2011). Imaging studies of PCr metabolism have been used to measure the effects of exercise on bioenergetic capacity(Kent-Braun, McCully et al. 1990). To enrich our interpretation of CrCEST imaging findings, we performed detailed analyses of the association between habitual intentional exercise, captured by the validated physical activity data collection instrument (Feldman, Appel et al. 2003), and the imaging parameters measured. In bivariate analyses, we demonstrated a muscle-group specific, positive association between habitual intentional exercise and both resting CrCEST and post-exercise CrCEST return to baseline. In multivariate analyses where mitochondrial disease diagnosis was also included in the statistical model, the independent effects of intentional exercise did not reach statistical significance, likely the result of the larger effect of disease status. However, when participants with mitochondrial disease were analyzed separately, a

positive association between intentional exercise and both resting CrCEST and τCr was observed. This result has a basis in both clinical and epidemiologic observations. Most physicians recommend exercise therapy for individuals with mitochondrial disorders (Parikh, Goldstein et al. 2014), on the basis of evidence of clinical benefit in mitochondrial disease (Murphy, Blakely et al. 2008, Jeppesen, Duno et al. 2009) and myriad other conditions, e.g., (Ricardo, Anderson et al. 2015). The optimal exercise therapy for individuals with metabolic myopathy remains the focus of ongoing study. Intriguingly, the preferred exercise strategy may be genotype-specific. For example, resistance training may decrease mutation burden in individuals with mitochondrial DNA deletions (Tarnopolsky 2014). We did not detect a strong statistically significant association between exercise and CrCEST parameters in control participants, perhaps related to small sample size and their overall higher level of function. Much remains to be learned, and CrCEST imaging may facilitate future research into how the nature of the intentional exercise may itself affect the chronic adaptation to training in skeletal muscle (Cochran, Percival et al. 2014). In addition, CrCEST imaging may be used to explore age- and muscle-group specific effects of exercise (Larsen, Callahan et al. 2012).

It must be noted that in this cross-sectional study, a causal relationship between exercise and imaging results cannot be established. An alternative explanation for our findings could be that individuals with mitochondrial myopathy who have higher resting CrCEST and more rapid return to baseline of CrCEST post-exercise are also more able to engage in intentional exercise. However, we found that affected individuals with mild disease (NMDAS total score less than 6) engaged in an average of 1.7 MET-hours of activity per

week, versus 6.1 MET-hours per week in those with moderate or severe disease (p=0.10 for two-sample t-test). That more severely affected individuals in our study may engage in more habitual exercise presents an intriguing possibility: individuals with worse disease who exercise may have better preserved physiology and function, and greater capacity to participate in many activities, including an exercise-based research protocol. A future exercise intervention study could explore this interesting question in detail.

We concluded that this study had several important strengths and limitations. One strength is that the study groups were balanced with respect to age, sex and, adiposity (BMI). Our experimental protocol minimized several factors thought to impact muscle OXPHOS capacity (pre-testing meal, pre-study exercise, and time of day). Other covariates were measured, including self-reported physical activity. Because some affected subjects were non-ambulatory, they had inherently lower physical activity than otherwise matched controls, which is a potential limitation to the study. We observed a range of %CrCEST change in study participants after exercise with our study paradigm, which required the same number of flexions and standardized resistance for each subject. For this initial proof-of-concept study, variation in %CrCEST change in response to light exercise was one focus of investigation. However, to address this potential source of variance in τCr measurements, %CrCEST was included in statistical models as a covariate. Future work would be further strengthened by setting exercise parameters in accordance with individual work capacity, and including the work performed by each subject as a covariate (Cree-Green, Newcomer et al. 2014, Sleigh, Lupson et al. 2016). In addition, it would be useful to validate techniques for individualizing exercise intensity

so as to standardize % change in CrCEST across participants of different abilities and levels of fitness when τCr is prioritized as the main outcome. While we have attempted to account for appropriate covariates in this population, it is important to note that other populations may have additional factors that need consideration; for example, recovery in patients with vascular disease could be influenced by blood flow, etc. Another potential limitation of the present study is that we used self-reported exercise data for analyses. However, physical activity as assessed using the same instrument has been associated with mortality in a separate study of individuals with chronic illness (kidney disease) (Ricardo, Anderson et al. 2015), thus we expect a reasonable degree of correspondence between our results with both imaging parameters and clinical outcomes.

Future studies may also incorporate an investigation of the relationship between τCr and the results of muscle biopsy studies. However, in the present study, most of the affected participants had not undergone invasive muscle biopsy for clinical purposes. Muscle biopsy had not been recommended because the clinical features, together molecular genetic testing results, were sufficient to establish the diagnosis of mitochondrial disease. We therefore did not see appropriate cause to perform invasive biopsy testing requiring general anesthetic, which may be poorly tolerated in individuals with mitochondrial disease. Affected individuals in this study with "classical" mitochondrial disease syndromes (CPEO-plus, MELAS, MELAS-like, Friedrich's Ataxia (FA)) and related genetic defects (mutations in *C10orf12, POLG, MFN2, FXN*) had clinical evidence of impaired muscle mitochondrial function. Deficits in mitochondrial electron transport chain activity via *ex vivo* skeletal muscle biopsy studies have been identified previously

in each of these mitochondrial disease syndromes. For example, the gene *C10orf12* encodes Twinkle, a helicase that is critical for mitochondrial DNA replication (Spelbrink, Li et al. 2001). Mutations in *C10orf12,* as well as the mitochondrial replicase, *POLG,* are associated with mitochondrial DNA depletion and/or deletions with muscle biopsy findings typically involving multiple respiratory chain complex enzyme deficiency and immunohistochemical evidence of cytochrome oxidase (Complex IV) deficient muscle fibers (Zierz, Joshi et al. 2015). In individuals with myopathy related to MELAS, skeletal muscle biopsy may demonstrate the presence of ragged red fibers, indicative of mitochondrial proliferation (Milone, Klassen et al. 2013). Seminal studies are additionally reviewed in (Dimauro, Bonilla et al. 1985). In FA, abnormal muscle OXPHOS capacity is related to mitochondrial iron overload; decreased OXPHOS capacity in FA has been demonstrated by skeletal muscle biopsy (Bayot, Santos et al. 2011) as well as ^{31}P-MRS (Lodi, Cooper et al. 1999). Mutations in "non-classical" mitochondrial disease genes, including succinate dehydrogenase (SDHx) subunit genes have been also associated with reduced OXPHOS capacity in muscle (Alston, Davison et al. 2012, Alston, Ceccatelli Berti et al. 2015) although the clinical association is less clear. For this reason, in this study we performed sensitivity analyses on the effects of excluding individuals with SDHx mutations and individuals with novel gene variants of uncertain significance with respect to mitochondrial disease on our main analysis.

3.6 Summary

In this small clinical study, we demonstrated persistent differences in post-exercise CrCEST decline exponential time constant as compared to healthy volunteers. Heterogeneity of clinical and molecular diagnoses in affected subjects is a source of biological variance. Despite this heterogeneity, we still observed a statistically significant effect of disease status on post-exercise τCr. This result shows that CrCEST imaging can identify decreased OXPHOS capacity in a genetically heterogeneous population whose molecular gene defects are likely to share a common pathophysiology involving decreased OXPHOS capacity (Bates, Hollingsworth et al. 2013). These studies demonstrate that non-invasive CrCEST imaging can be used to quantitatively monitor physiologic changes after exercise, including both creatine content and metabolic capacity, in individuals with mitochondrial diseases. Optimally, CrCEST will be used to complement existing ^{31}P MRS-based assessments to perform a more complete, comprehensive assessment of the phosphocreatine shuttle function in individuals with mitochondrial disorders. This work lays a foundation to develop CrCEST as a potential non-invasive imaging-based biomarker of OXPHOS capacity that may be useful in the diagnosis, long-term monitoring, and/or evaluation of response to clinical treatments in individuals with diverse types of mitochondrial diseases.

Chapter 4 - Development of Lactate CEST and its applications for monitoring glycolysis *in vivo*

4.1 Introduction

In the preceding chapters, we discussed the CEST imaging technique in context of metabolic disorders, focusing on creatine as a marker of mitochondrial function. This chapter will shift focus to lactate, which is another vital metabolite and particularly relevant to cancer. Changes in lactate metabolism are associated with a wide variety of diseases besides cancer (Waterhouse 1974), such as cardiac failure (Chiolero, Revelly et al. 2000), liver disease (Jeppesen, Mortensen et al. 2013), diabetes mellitus (Misbin, Green et al. 1998), and neurologic disorders such as epilepsy (Folbergrova and Kunz 2012). We will discuss our motivation for developing lactate CEST, the development process using phantoms, and some initial applications *in vivo*.

4.1.1 Lactate metabolism

In the human body, lactate (a hydroxycarboxylic acid) is derived from glucose, which is metabolized via glycolysis or the pentose phosphate pathway. In glycolysis, glucose is first converted into pyruvate and then into lactate by lactate dehydrogenase (LDH). This occurs in the cytosol and has a corresponding oxidation of NADH to produce NAD+. This reaction is reversible; the reverse direction oxidizes lactate back to pyruvate while generating NADH from the reduction of NAD+. In the pentose phosphate pathway, glucose is metabolized to form NADPH and ribose-5-phosphate. As discussed in Chapter 1, NADPH is necessary for synthesizing fatty acids. Lactate can also be formed from alanine by the enzyme glutamate pyruvate transaminase (GPT), which catalyzes the conversion of alanine and α–ketoglutarate into pyruvate and glutamate, respectively

(Adeva, Gonzalez-Lucan et al. 2013). This process occurs both in the cytoplasm and in the mitochondrial network. Once pyruvate is formed through this reaction, it can be reduced to lactate by LDH. Oxidation of pyruvate to CO_2 to generate energy is required for the oxidative metabolism process detailed in Chapter 1. Defects in the mitochondrial respiratory chain (or in the TCA cycle) inhibit ATP synthesis from substrates like pyruvate. This causes cells to become dependent on glycolysis instead, which doesn't require oxygen to generate ATP, and produces lactate as the end product (Gladden 2004).

4.1.2 Lactate in skeletal and cardiac muscle

In resting skeletal muscle, lactate generally maintains a concentration of ~3 mM, compared to ~1mM in blood (Gaitanos, Williams et al. 1993). Skeletal muscle produces and consumes lactate. When muscle is exercised, lactate concentration increases and is released into the bloodstream. With high-intensity exercise, lactate levels in the blood are increased when skeletal muscle oxygen is consumed leading to utilization of glycolysis and a subsequent rapid rise in lactate, which is washed out into the blood. Large increase in lactate concentration is referred to as hyperlactatemia, which the body responds to by uptake of lactate by other tissues, for example, non-exercising muscles. In subjects who undergo endurance training, lactate production in muscles is eventually reduced, leading to enhanced oxidative efficiency of the mitochondrial respiratory chain (Bergman, Wolfel et al. 1999, Steiner, Murphy et al. 2011). When tissues become hypoxic, which can occur for a variety of reasons including heart disease, skeletal muscles respond to any amount of activity with a dramatic increase in lactate production. Lactate may also regulate substrate utilization in myocardial tissue, as there is correlation between levels of lactate

in blood and the cardiac lactate extraction in healthy subjects undergoing moderate exercise. In addition to the importance of lactate in healthy muscle metabolism, in some of the mitochondrial disorders described in chapter 3, like MELAS, there is a clinical feature of lactic acidosis.

4.1.3 Lactate in cancer

As a result of the Warburg effect, tumors exhibit up-regulated lactate dehydrogenase (LDH), leading to increased levels of lactate (Fantin, St-Pierre et al. 2006). The enzyme responsible for lactate production, LDH, has become a target for cancer therapy. In tumors, when oxygen is absent or in short supply (hypoxia), LDH converts pyruvate to lactate (Potter, Newport et al. 2016). Even in the presence of sufficient oxygen, tumor cells derive their energy from glycolysis (Warburg effect) leading to increased production of lactic acid (Heiden, Cantley et al. 2009, Dang 2010, Hirschey, DeBerardinis et al. 2015). As discussed in Chapter 1, this seems to benefit the cancer cells by allowing them to divert more substrates into anabolic processes required for continued cell growth and proliferation. Several studies have shown that tumor lactate levels correlate with increased metastasis, tumor recurrence, and poor outcome (Walenta, Wetterling et al. 2000, Brizel, Schroeder et al. 2001). Lactate also plays a role in promoting tumor inflammation and can function as a signaling molecule that stimulates tumor angiogenesis (Doherty and Cleveland 2013). Non-invasive measurement of lactate is of tremendous significance to the study of metabolic defects in a wide range of pathologies.

4.1.4 in vivo measurement of lactate

Currently there are two major methods employed in measuring lactate *in vivo*. One is traditional magnetic resonance spectroscopy (MRS; both ^{1}H and ^{13}C) (Gribbestad, Petersen et al. 1994, DeBerardinis, Mancuso et al. 2007), which has been used to measure both static lactate levels and dynamic changes. However, these are limited by inadequate sensitivity and spatial resolution. The other method involves ^{13}C-labeled pyruvate infusion and dynamic nuclear polarization (DNP), which provides greater than 10,000 fold signal enhancement compared to conventional MRS (Golman, in't Zandt et al. 2006, Golman, in't Zandt et al. 2006, Day, Kettunen et al. 2007). Despite its high sensitivity, this method only probes fast kinetics (<1min) of lactate turnover from ^{13}C-labeled pyruvate, and it requires special equipment and complex modeling for data analysis (Nelson, Kurhanewicz et al. 2013, Walker-Samuel, Ramasawmy et al. 2013). There is a clear need for development of new tools for noninvasive imaging of lactate *in vivo*.

In the context of cancer imaging, CEST has been previously used to image hydroxyl protons from glucose (Chan, McMahon et al. 2012, Wang, Weygand et al. 2016). Glucose serves as fuel for proliferating cancer cells, and higher glucose uptake is observed in certain tumor types than in healthy tissue, and so it was hypothesized that an infusion of glucose into tumor tissue would create an increase in CEST contrast. This method utilizes standard proton MRI and requires neither ^{13}C labeled pyruvate nor DNP polarization. However, in some recent studies it was speculated that the observed increase in CEST signal after glucose injection into tumor tissue could be due to combined CEST

effect from glucose and other byproducts of glucose metabolism, like lactate, which also have exchangeable hydroxyl protons (Wang, Weygand et al. 2016).

No previous studies had demonstrated the ability of CEST to image endogenous hydroxyl protons of lactate *in vivo*. Recent work from Zhang *et al*. has shown that lactate can be imaged *in vitro* and *in vivo* by means of a paramagnetic shift agent, but this requires the injection of the contrast agent (Zhang, Martins et al. 2017). In this chapter, we will describe the method based on *endogenous* **lac**tate chemical exchange saturation transfer (C**EST**) to image lactate as **LATEST** (DeBrosse, Nanga et al. 2016). First, we identified the chemical shift of lactate hydroxyl protons through high-resolution NMR, and then demonstrated the CEST effect from those protons in lactate phantoms. We determined optimal CEST saturation parameters for lactate imaging. Then, we examined the pH and concentration dependence of the LATEST contrast in phantoms. The feasibility of measuring LATEST *in vivo* was demonstrated in a lymphoma tumor model and in human skeletal muscle. Dynamic changes in LATEST were observed in tumors pre- and post-infusion of pyruvate and in exercising human skeletal muscle. LATEST measurements were compared to lactate measured with multiple quantum filtered proton magnetic resonance spectroscopy (SEL-MQC ^{1}H-MRS) (He, Shungu et al. 1995).

4.2 Methods

Systems

- High-resolution 1-D ^{1}H NMR phantom experiments were performed on a vertical bore Bruker Avance DMX 400 MHz spectrometer (Bruker Corporation, Germany), equipped with a 5mm PABBI proton probe.

- MRI phantom experiments and human skeletal muscle studies were performed on whole body 7T whole-body MRI scanner (Siemens, Erlangen, Germany) with a 28-channel QED knee RF coil.
- Additional MRI phantom experiments and animal experiments were performed on a 9.4T, 30cm horizontal bore magnet (Agilent, USA) interfaced to a Varian console, with a 20mm volume coil (M2M Imaging, USA), and a custom-built surface coil/loop coil.

4.2.1 Phantom studies

NMR experiments at 9.4T (vertical bore). For the high-resolution NMR experiments at 9.4T (vertical bore), 15M sodium lactate was prepared in PBS buffer at pH = 7.1. A phantom was made by placing a ~0.5mL of the 15M solution into a 5mm glass NMR tube. For NMR experiments, a sealed capillary containing a mixture of D_2O (for lock) and 10 mM tetramethylsilane (TMS) (for reference) was inserted into the sample tubes. The spectral parameters used were 2 dummy acquisitions followed by 24 acquisitions (pulse sequence: 'zz30.sw'), 65536 TD (real+imaginary), 6775 Hz sweep width, and a relaxation delay of 4s. Temperature was varied from 4°C to 37°C. For post-processing, the 1D-^{1}H NMR spectra were processed using Spin Works (version 4.0.0, Copyright ©2013, Kirk Marat, University of Manitoba). All the spectra were referenced to TMS. The exchange rate was determined by obtaining T_2 values from lactate phantoms (0, 10, 20, 30, and 50mM) at 25°C and from the calculated relaxivity (Ordidge, Connelly et al. 1986), and using the chemical shift of lactate obtained from the unsuppressed water spectrum at 4°C (~0.8ppm).

Phantom experiments at 7T. For the 7T MRI phantom experiments, sodium L-lactate (Sigma Aldrich, USA) solutions were prepared phosphate-buffered saline (PBS) at pH 7. First, a 50mM sample of sodium lactate in 300mL of PBS was prepared, and a phantom was prepared by placing the ~1.5mL of the solution into a 10mm glass NMR tube. This phantom was used for optimization of CEST parameters, including B_1 strength and pulse duration. The original 50mM solution was subsequently used to make serial dilutions for the concentration-dependent study: 30mM, 20mM, and 10mM. The 30mM sample was used for a pH-dependent study; the pH was adjusted to 7.4, 7, 6.8, and then 6.5, using 1N NaOH and HCl. Phantoms were prepared in 10mm NMR tubes for all concentrations and pH values. 7T MRI phantom studies were performed at both 25°C and 37°C. For initial imaging at 37°C, the individual 10mm-tube phantoms were sealed and then heated in a water bath to 37°C, before being placed into custom-made, plastic tube (volume =280mL) with slots cut into the top to hold the tubes in place. This large tube was filled with water (37°C) so that the phantoms were surrounded by water and the temperature could be maintained for ~1 hr. This large phantom setup allows for multiple samples to be imaged simultaneously, and was placed upright inside the knee coil for imaging experiments. The temperature of the samples was measured before and after imaging. The imaging parameters for 7T phantom experiments using a 28-channel ^{1}H knee coil were: slice thickness = 10mm, GRE flip angle =5°, GRE readout TR = 5.6ms, TE = 2.7ms, FOV = 130 x 130mm^2, SHOT TR = 12s, matrix size = 128 x 128. A B_1 titration

(0.36 μT to 1.44 μT in steps of 0.36 μT) was performed at three different durations (3s, 4s, and 5s), to determine optimal CEST saturation parameters.

Phantom experiments at 9.4T (horizontal bore). For the concentration dependent study at 9.4T, phantoms with 10, 20, 30 and 50 mM sodium lactate (Sigma Aldrich, USA) concentration in phosphate buffered saline (PBS) were prepared at pH 7.0 and placed in individual 15mm glass NMR tubes. For the pH-dependent study, 30mM lactate samples were again initially prepared in PBS at pH 7, and pH was adjusted to 6.0, and 6.5 using 1N HCl, and adjusted to pH 7.5 with NaOH. As the 9.4T is intended for animal imaging experiments, it has a small horizontal bore coil that cannot accommodate the multi-sample phantom that we used at 7T. For the 9.4T imaging experiments, we performed individual experiments for each sample, taking care to avoid air bubbles when the samples were turned horizontally. Each sample was pre-heated in a water bath. During the imaging experiments, the temperature was maintained at 37°C by blowing a warm air directed at the tube and monitored using a thermocouple attached to the NMR tube. Accurate temperature was recorded throughout the duration of the experiments. The B_1 strength and pulse duration for LATEST contrast at the horizontal bore 9.4T was optimized using a 50 mM sample of sodium lactate (pH 7.0) in PBS. Saturation pulses of varying B_{1rms} (1.18 μT to 4.11 μT in steps of 0.59 μT) were acquired from -1.5ppm to +1.5ppm in steps of 0.1 ppm. CEST imaging was performed using a custom-programmed, segmented radiofrequency GRE readout pulse sequence, with a frequency selective continuous wave saturation preparation pulse. The sequence consists of an 8s delay, followed by a 5s saturation pulse, with 780ms total centric phase encode readout

(128 segments, 6.1ms each). The imaging parameters were: slice thickness = 5 mm, GRE flip angle = 5°, GRE readout TR = 5.6 ms, TE = 2.7 ms, Field of view = 25 × 25 mm^2, matrix size = 128 × 128, and one saturation pulse at a root mean square B_1 (B_{1rms}) of 100 Hz (2.34 μT). B_0 correction was done by acquiring WASSR(Kim, Gillen et al. 2009) images at 0.24 μT from -1 to +1 ppm in steps of 0.1 ppm, using the same parameters as CEST. Z-spectra were plotted using the normalized image intensity as a function of the resonance offset of the saturation pulse.

4.2.2 Animal studies

The Institutional Animal Care and Use Committees (IACUC) of the University of Pennsylvania approved experimental protocols, and all experiments were carried out in accordance with approved IACUC guidelines.

Lymphoma tumor model: Preparation of lymphoma xenografts. Male athymic nude mice (n=4) (01B74) 4-6 weeks of age were obtained from the National Cancer Institute, Frederick, MD, USA. The mice were housed in microisolator cages and had access to water and autoclaved mouse chow *ad libitum*.

The tumor cells used in this study were diffuse large B-cell lymphoma cells from the WSU-DLCL2 cell line, and were kindly provided by Drs Mohammad and Al-Katib (Wayne State University, Detroit, MI, USA). The cells were grown as described in detail by Al-Katib *et al.* (Mohammad, Wall et al. 2000): briefly, the cells were "maintained in RPMI 1640 containing 10% heat-inactivated fetal bovine serum, 1% l-glutamine, 100

units/ml penicillin G, and 100ug/ml streptomycin. The cells were incubated in a humidified 5% Co2 atmosphere at 37°C."

Cells were implanted subcutaneously into the right thigh of 4-6-week-old male athymic nude mice (01B74) 4-6 weeks (National Cancer Institute) by injecting ten million WSU-DLCL2 cells in 0.1mL Hanks' Balanced Salt Solution (without calcium or magnesium; Invitrogen/Gibco, Carlsbad, CA, USA). Lymphoma xenografts were allowed to grow until the tumor volume reached ~500 mm^3. The tumor dimensions were measured with calipers in three orthogonal directions, and the volume was calculated using the equation, $V= \pi(a\times b\times c)/6$, where a, b, and c are the length, width, and depth of the tumor.

Lymphoma tumor model: Imaging and spectroscopy. For imaging and spectroscopy experiments at 9.4T (horizontal bore) of the lymphoma tumor mice, we used a custom-built single frequency (^1H) slotted tube resonator (inner diameter = 13 mm, outer diameter = 15 mm, depth = 16.5 mm).

The mice were anaesthetized and maintained under 1% isoflurane in 100% oxygen, supplied at 1 L/min for the duration of the experiment, which did not exceed three hours per IACUC guidelines. The animal body temperature was maintained at 37 ± 1°C with the air generated and blowing through a heater (SA Instruments, Inc., Stony Brook, NY). Respiration and body temperature were continuously monitored using a MRI-compatible small animal monitor system (SA Instruments, Inc., Stony Brook, NY). CEST imaging was performed as described for phantoms at 9.4T with the following sequence parameters: field of view = 25 × 25 mm^2, slice thickness = 3 mm, flip angle = 15°, TR =

6.2 ms, TE = 2.9 ms, matrix size = 128 × 128. CEST images were collected with B_{1rms} = 1.17 μT for frequencies ranging from -1.5 ppm to + 1.5 ppm from bulk water in step size of 0.1 ppm. B_1 and WASSR B_0 field maps were also acquired and used to correct the CEST maps as described previously (Kogan, Haris et al. 2013).

Following acquisition of the baseline CEST images, sodium pyruvate (300 mM) was delivered through a tail vein catheter (26 Gauge, I.V. Catheters FEP, Tyco Healthcare, Tyco International Ltd., Schaffhausen, Switzerland) at a variable rate using a syringe pump (Harvard Apparatus, Holliston, MA, USA) using the following protocol: (10ml/hr, 1min; 3ml/hr, 4min; 2.5ml/hr, 2min; 2.0ml/hr, 2min; 1.5ml/hr, 2min; 1.0ml/hr, 2min; 0.5ml/hr, 57min) making a constant blood pyruvate concentration of 13 mM during the experiment. CEST images were then acquired after the infusion.

Tumor lactate was also measured using HADAMARD SEL-MQC ^{1}H-MRS (He, Shungu et al. 1995, Pickup, Lee et al. 2008) in separate experimental sessions. For lactate measurements following pyruvate infusion, tumors were positioned in a home-built, single-frequency (^{1}H), slotted-tube resonator (inner diameter, 13 mm; outer diameter, 15 mm; depth, 16.5 mm). A slice-selective double-frequency Hadamard-selective multiple quantum coherence transfer pulse sequence was used to detect lactate and to filter out overlapping lipid signals. The acquisition parameters were as follows: sweep width = 4 kHz; 2048 data points; TR = 8 s; 128 scans. Since there is no published lactate visibility data on this tumor model we have chosen to correlate the lactate peak amplitude values with the LATEST results.

9L brain tumor model in rats. LATEST was also implemented to probe the lactate dehydrogenase (LDH) activity *in vivo* in a rat glioma model. Syngeneic female Fisher F344/NCR rats were used to generate the model. MRI experiments were performed on the 9.4T MRI scanner on rats that had been injected with 9L cells intracranially 3 weeks prior. During the imaging experiments, tumor-bearing rats were maintained under 1-1.5% isourane in O_2, supplied at 1 L/min. Throughout the experiment, the body temperature was maintained at 37º C. T_2 weighted imaging was performed on the brain to locate the tumor region in coronal slices. For these experiments, the LATEST sequence parameters were: slice thickness=2 mm, GRE flip angle=5º, GRE readout TR=5.6 ms, TE=2.7 ms, FOV=30×30 mm, matrix size=128×128, number of averages=4. LATEST images from 0 to ±1.5 ppm (step size 0.25 ppm) were collected at 1.17 μT saturation pulse power (B_1) and saturation duration of 4s. B_0 correction on the LATEST images was performed by acquiring WASSR images at 0.24 μT from -1 to +1 ppm in steps of 0.1 ppm. LATEST maps were computed using the method described above. Following the acquisition of the baseline CEST signal, sodium pyruvate (300 mM) was delivered through a tail vein at a rate of 100uL/min via a syringe pump. Following the 15-min infusion of pyruvate (for a total volume of 1.5mL), the CEST acquisitions were performed over a period of 90 minutes.

4.2.3 Human imaging

All human studies were performed under the approved Institutional Review Board (IRB) protocol of the University of Pennsylvania. The studies were carried out in accordance

with approved IRB guidelines. Written informed consent was obtained from all subjects after explanation of the study protocol.

Lactate CEST imaging was performed on the right calf muscle of 5 healthy male subjects (ages 21-35) on a Siemens 7T whole body scanner using a 28-channel ^{1}H knee coil. The coil was positioned around the calf muscle as described for the CrCEST experiments in Chapter 2. Two baseline CEST images, as well as WASSR (Kim, Gillen et al. 2009) B_0 and B_1 field maps were acquired pre-exercise (Kogan, Haris et al. 2013, Kogan, Haris et al. 2014). For this study, WASSR images to correct for B_0 inhomogeneities were collected from -1 to +1 ppm with a step size of 0.05 ppm and saturation pulse train amplitude, (B_{1rms} = 0.29 μT) and 3000-ms duration using the same sequence as used for CEST imaging and identical readout parameters as described in Chapter 3.

Each CEST image was collected using a saturation pulse consisting of a 3s long saturation pulse of a series of 99.6-ms Hanning windowed saturation pulses (B_{1rms} = 0.73μT). The parameters for CEST imaging were: slice thickness =10mm, SHOT TR=6s, TR=6.1 ms, TE=2.9ms, FOV = 140x140 mm^2, matrix size 128x128. CEST images were acquired from 0 - ±0.8 ppm, in steps of 0.1ppm. Like in the CrCEST experiments from Chapter 2, plantar flexion exercise was performed in-magnet with the magnetic resonance compatible, pneumatically-controlled foot pedal. However, for the LATEST experiments, the pressure was held constant at 9 psi for all subjects, requiring more force to depress the foot pedal. Unlike the mild exercise in the CrCEST experiments, the subjects in this study were instructed to exercise until exhaustion, which was approximately 3.5 minutes of intense exercise, with subjects indicating when they could not perform further flexions.

Immediately post-exercise, the center frequency was recorded and, if required, was "reset" in order to ensure accurate pulse saturation at the correct resonance for LATEST. An anatomical reference image with no saturation was also acquired after checking the center frequency, to allow for muscle segmentation even if motion had occurred between the pre-exercise and post-exercise slice positions. This took approximately 60-85 seconds for every subject. Immediately following the reference image acquisition, 10 sequential sets of CEST images were acquired with a time resolution of 1.8 minutes, and so the first post-exercise CEST image finished acquiring at ~3 min post-cessation of exercise. Finally, B_1 and WASSR maps were again acquired at the end of exercise for correction of the post-exercise CEST images.

Lactate spectroscopy was acquired using image selection using inversion spectroscopy (ISIS) (Ordidge, Connelly et al. 1986) localization followed by a selective multiple quantum coherence (MCQ) editing sequence (Pickup, Lee et al. 2008). Spectroscopy was performed on 3 human subjects (ages 24-65), with the same exercise paradigm. A voxel of 30x80x40mm was placed over the gastrocnemius muscle. Pre-exercise, spectra were acquired for 96 seconds. After the subjects performed the intense, in-magnet exercise, spectra were acquired for a total of 20 minutes, 48s. For quantification purposes, both water spectra and lactate spectra were acquired from the same voxel. The details of the lactate-editing spectroscopy sequence can be found in He *et al*. For these experiments the spectroscopy parameters were: TR=3s, TE=165.6ms, dummy scans=4, water averages=8, lactate edited spectra averages=8*n, n=2 for pre-exercise, n=50 for post-exercise.

4.2.4 Post processing Methods

As described in Chapter 2, CEST asymmetry was calculated using Equation 1.25 where M_0 is the magnetization obtained with saturation at -20ppm, M_{sat} ($\pm\Delta\omega$) are the magnetizations obtained with saturation at a '+' and '–' offset to the water resonance with a $\Delta\omega$ equivalent to the resonance offset of the exchanging spins.

Because the –OH protons of lactate resonate ~0.4ppm away from water, an interpolation routine of the z-spectrum from ±1.2ppm with a stepsize of 0.005ppm was implemented to correct B_0 inhomogeneities.

LATEST B_0 correction. Previous CEST methods have typically been developed for metabolites with resonance frequencies >0.5ppm away from the large bulk water peak, like creatine or glutamate as discussed in the previous chapters. For those metabolites, typically we acquire partial z-spectra for a small set of saturation offset frequencies around +/- CEST offset of interest. Two separate polynomial fits following spline interpolations on the positive and negative frequencies were sufficient for correction of B_0 inhomogeneities. As demonstrated in this work, the hydroxyl proton of lactate resonates ~0.4ppm downfield from water. In this case, a more robust method for B_0 correction is required in post-processing. First an under-sampled raw full z-spectrum (including 0 ppm) is created from each image pixel. Then, a cubic spline interpolation is used to create a finely sampled z-spectrum (x100). Using the B_0 values for each pixel, the z-spectrum is then shifted based on the B_0 value: the spectrum is shifted to the left for negative values, or to the right for positive values. From the shifted spectrum, we can

then calculate the CEST values at the saturation offset of interest (~0.4ppm for the lactate hydroxyl proton).

From the MQC-filtered spectroscopy data, lactate concentration was calculated using the ratio of lactate integrals and water spectra from the same volume, accounting for lactate visibility from double-quantum spectroscopy, and the efficiency factor of the editing.

Lactate quantification from ISIS localized Sel-MQC edited spectra. Lactate concentration was derived from spectroscopy using Sel-MQC filtering, as described in the Methods. In order to quantify the lactate concentration, an ISIS-localized water peak was acquired before the Sel-MQC. The concentration of lactate was obtained using a simple formula:

[lactate] = estimated free water concentration in muscle * (lactate integral/water integral) * c1;

c1 is a correction factor, which is given by the following equation:

$$c1 = 2.0 * \frac{2}{n} * \frac{1.0}{\cos(\pi J t)} * \frac{1}{0.2e^{-\frac{TE(ms)}{144}}} + 0.8 * e^{-TE(ms)/37}$$

(Equation 4.1)

where 'n' is the number of spins (n=3 for lactate), 't' is the echo position offset relative to (1/2J) and the previously reported double exponential T_2 decay of lactate rat skeletal muscle (Jouvensal, Carlier et al. 1997) , in which 80% of the signal has a T_2 of 37ms, and 20% has a T_2 of 144ms.

4.3 Results

4.3.1 Phantom studies

The first requirement for this project was determining if the lactate hydroxyl (-OH) could be imaged using CEST. First, we identified the chemical shift of the hydroxyl proton resonance by 1D ^{1}H NMR. We performed a temperature-dependent study on a 15M lactate solution prepared in phosphate-buffered saline, varying the temperature from 4°C to 37°C (**Figure 4.1**).

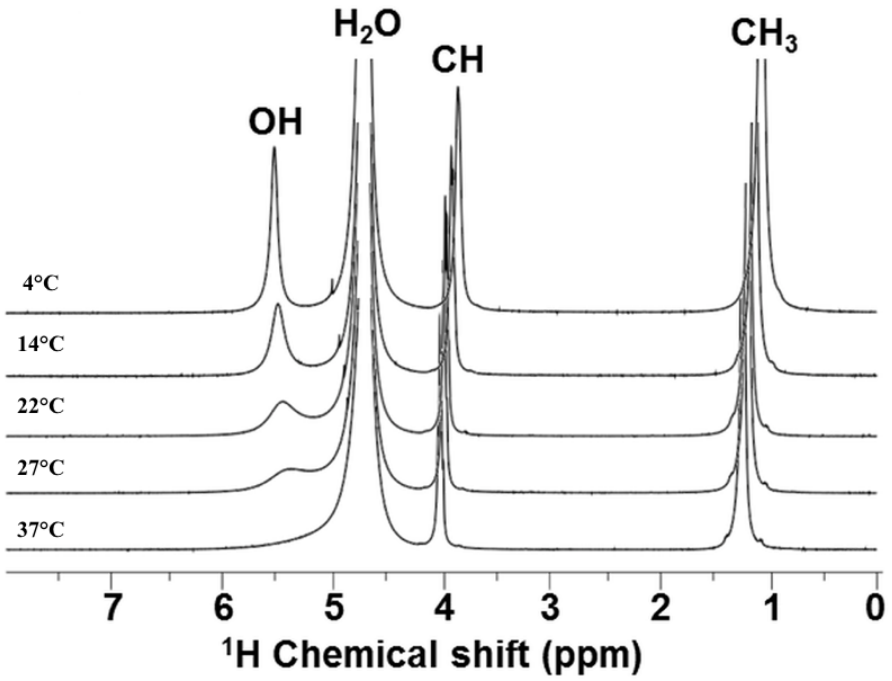

Figure 4.1 Determination of lactate –OH resonance. High-resolution 1D-^{1}H NMR spectra of 15M sodium lactate (in PBS buffer at pH 7.1 ± 0.1) at varying temperatures

acquired with Bruker Avance DMX 400 MHz spectrometer equipped with a 5mm PABBI proton probe. *(Reprinted with permission (DeBrosse, Nanga et al. 2016).)*

At 4°C, we observed a sharp –OH peak at ~0.8ppm (relative to the water peak at 4.7ppm). As we changed the temperature from 4°C to 27°C, we still observed the –OH peak, although the peak position varied from ~0.8 to 0.4 ppm. At 37°C, the –OH resonance was not clearly visible by ^{1}H NMR, owing to the significant exchange broadening and proximity to the water resonance.

When we acquired a full z-spectrum (±1.5ppm) of 50mM lactate solution at 7T, it did not exhibit any sharp features (**Figure 4.2A**).

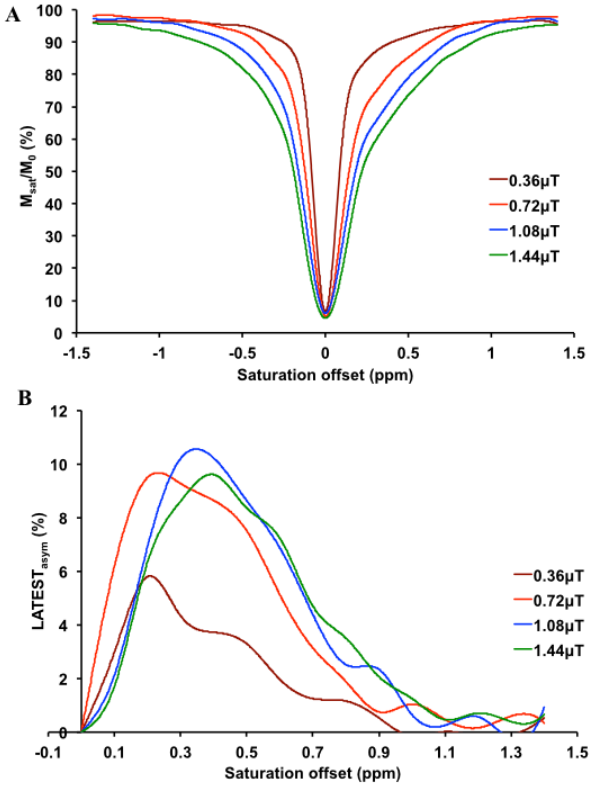

Figure 4.2 Initial phantom experiments on 50mM lactate solution at 7T: titration of B_1 pulse power. These experiments demonstrated the feasibility of measuring lactate with CEST, despite the lack of a sharp peak in the z-spectrum. Clear resonance is observed at ~0.4ppm at room temperature in the asymmetry plot.

The peak is masked in the z-spectrum by the overwhelming water signal. However, when we plotted the corresponding CEST asymmetry, which subtracts the water peak, we observed the lactate –OH resonance centered at ~0.4ppm. We then acquired another set of z-spectra on the 50mM sample, using a 5s saturation pulse duration while titrating the B_1 (**Figure 4.2B**). From this, maximum lactate CEST signal was observed with B_{1rms} =~1.08μT. The CEST asymmetry value of lactate ("$LATEST_{asym}$") for subsequent experiments was calculated at 0.4ppm. With the B_{1rms} = ~1.08 μT, we observed ~10% $LATEST_{asym}$ at 0.4ppm (**Figure 4.3**).

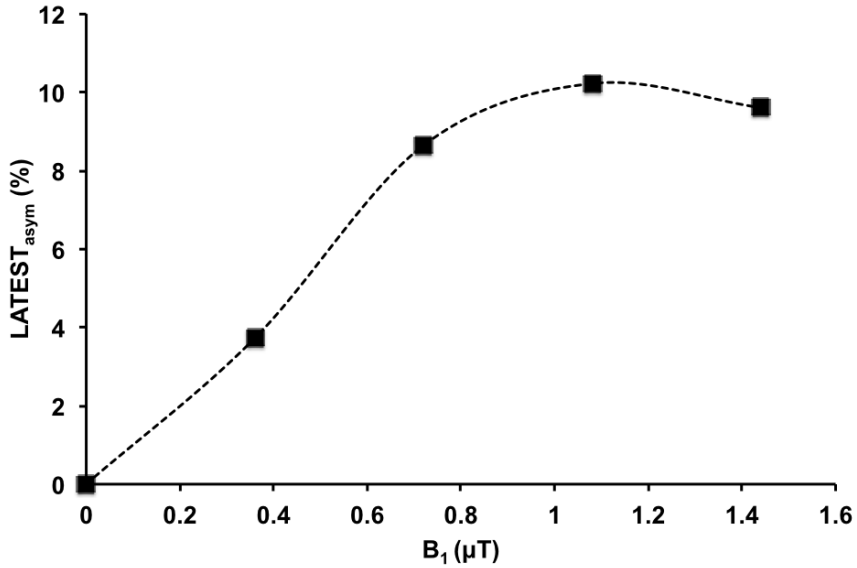

Figure 4.3 B_1 dependence of LATEST in phantoms at 7T.

Using the optimal B_{1rms}, we then performed a titration of the pulse duration (**Figure 4.4**), where the optimal $LATEST_{asym}$ was obtained with 5s.

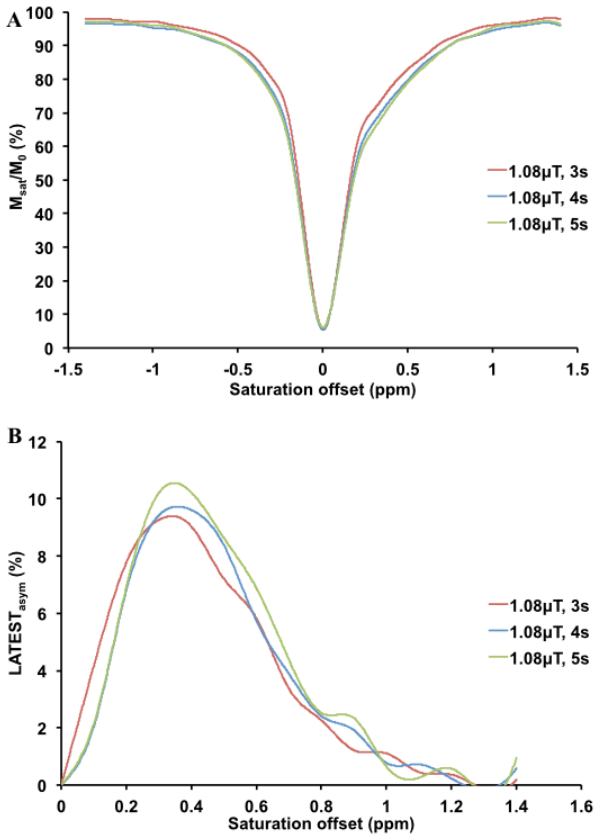

Figure 4.4 Initial phantom experiments on 50mM lactate solution at 7T: titration of B_1 pulse duration. In phantoms at room temperature, a long pulse of 5s provided maximum LATEST contrast.

After establishing the optimal CEST phantom parameters on the 50mM sample, we looked at the concentration dependence of LATEST, by calculating the $LATEST_{asym}$ (**Figure 4.5A**), and then plotting the $LATEST_{asym}$% at 0.4ppm vs. concentration. At 7T (25°C), using a 5s saturation length with ~1.08 μT B_{1rms} we calculated a concentration dependence of ~0.25% CEST/mM (**Figure 4.5b**).

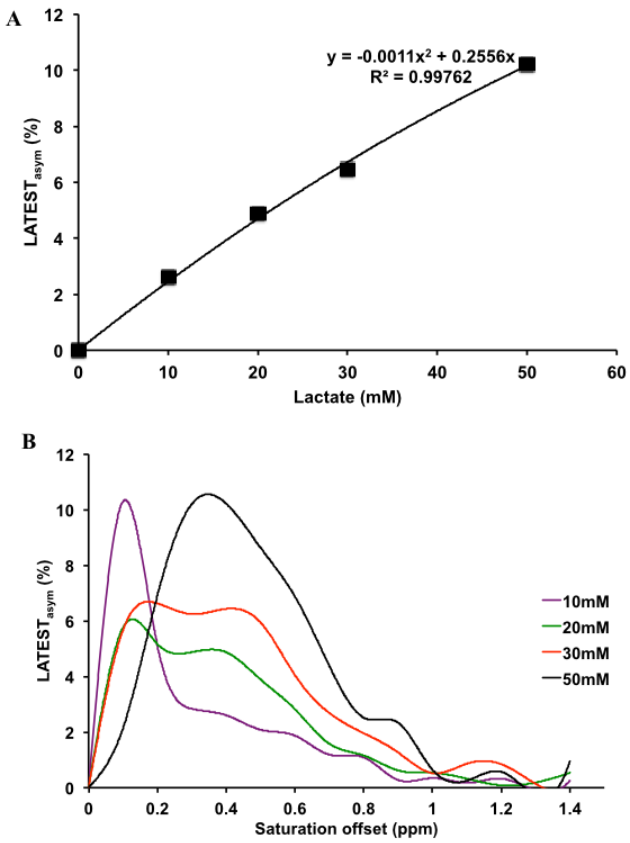

Figure 4.5 Concentration dependence of LATEST at 7T.

We also performed a pH-dependent experiment, varying the pH of the 30mM sample and again calculating the $LATEST_{asym}$ % at 0.4ppm and plotting vs. pH value (**Figure 4.6**). We observed a maximum LATEST signal at approximately pH=6.8 - 7.

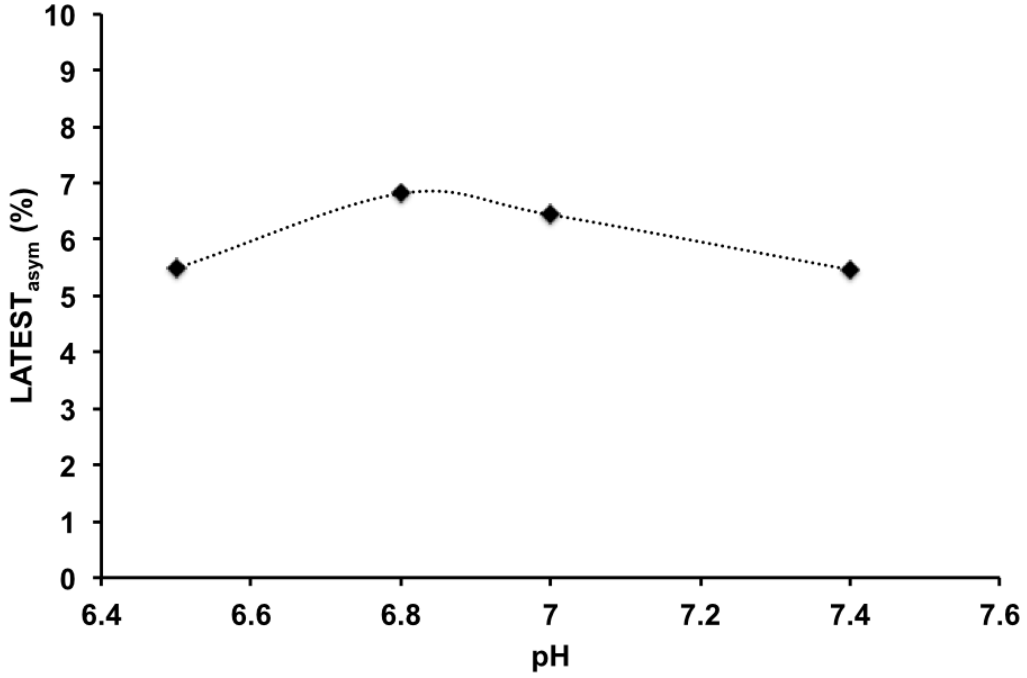

Figure 4.6 pH dependence of LATEST at 7T. Initial pH studies indicated that the maximum LATEST contrast was achieved with a pH of ~6.8, with decreasing contrast associated with either increased or decreased pH.

These initial experiments were all performed at room temperature (25°C) in order to establish the feasibility of imaging lactate with CEST, and to optimize the CEST parameters. As described in the Methods section, at 7T we used a custom-made large phantom holder placed inside a 28-ch knee coil. This phantom setup is useful for imaging multiple samples at once, and can also be used for experiments at physiological temperature (37°C) by pre-heating the samples. However, this setup only allowed for ~1 hr of consistently maintained heated temperature before we noted a drop. For this reason,

we performed some initial CEST imaging of the 50mM sample at 37°C at 7T, before moving the phantom study to 9.4T. At 37°C, we performed another B_1-dependent experiment, using a 5s pulse duration, and compared the 25°C data, and determined that the optimal B_{1rms} for physiological-temperature phantoms was ~1.44 μT (**Figure 4.7**). Based on the experimental signal-to-noise ratio (SNR), we determined that this method had sufficient sensitivity to detect 2 to 3 mM lactate.

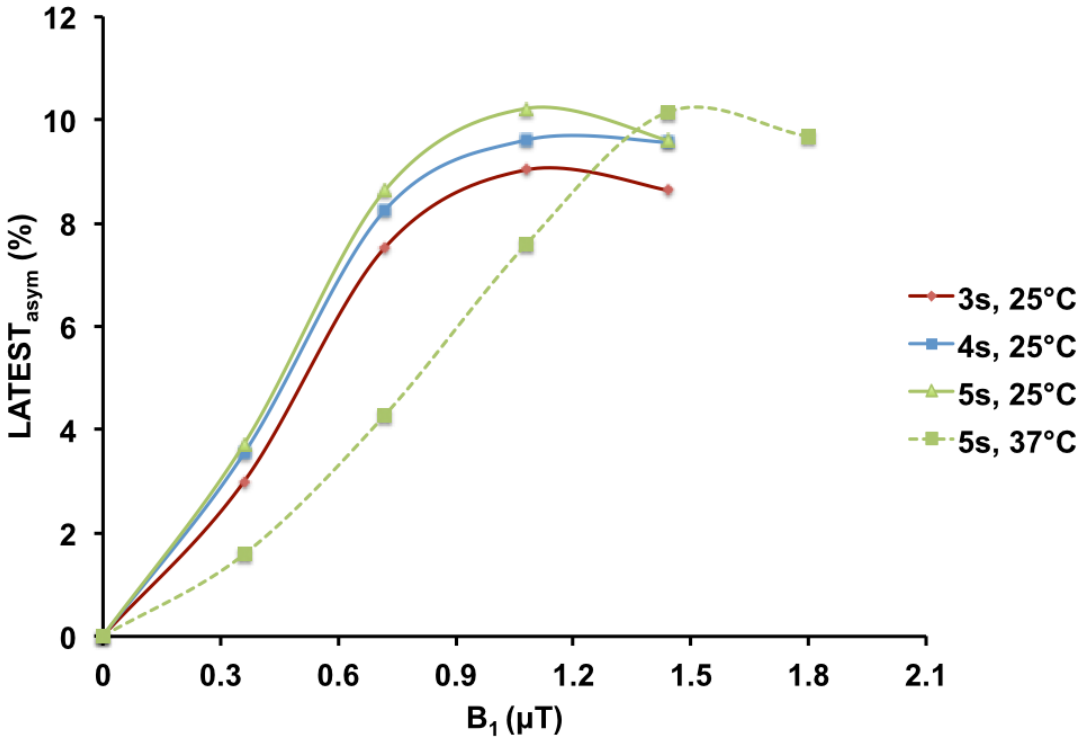

Figure 4.7 Phantom temperature dependence at 7T, acquired on a 50mM lactate phantom. With increasing temperature, the pulse power for optimal LATEST contrast is increased.

After establishing that CEST of lactate phantoms was feasible at 7T, we continued our phantom experiments at 9.4T. In addition to validating the method at 9.4T, we expected that by moving to a higher field where the chemical shift difference is larger, we would avoid some of the effects of direct saturation (DS) to the lactate CEST signal that we observed at 7T. With our experimental setup at 9.4T, we were able to maintain the temperature for extended periods of time, as described in the Methods, allowing for more thorough data collection.

As anticipated, the z-spectrum of 50 mM sodium lactate obtained at 9.4T did not exhibit any sharp features at 37°C (**Figure 4.8A**). However, the CEST asymmetry plot exhibited resonance centered between ~0.3 to 0.5 ppm (**Figure 4.8B)**. For the 50mM phantom, we generated a representative CEST map at 0.4ppm by overlaying the $LATEST_{asym}$ signal (~14%) onto the proton reference image (**Figure 4.8C)**.

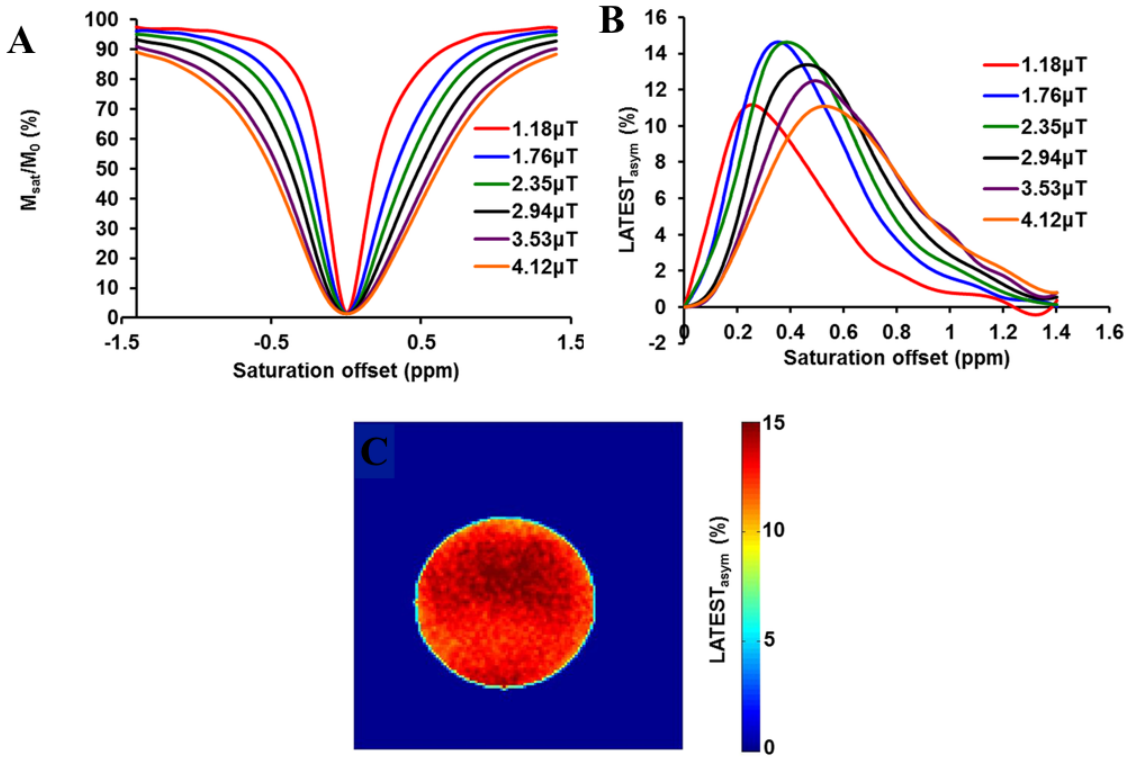

Figure 4.8 Characterization of LATEST at 9.4T. (A) Z-spectrum, (B) asymmetry plot, and (C) CEST map for 50mM lactate at 9.4T, pH 7, at 37°C with B_{1rms} titrated from 1.18μT – 4.12μT, with a saturation duration of 5s. *(Reprinted with permission (DeBrosse, Nanga et al. 2016).)*

Optimal LATEST parameters in phantoms at 9.4T were B_{1rms}= 2.35μT, with a 5s duration (**Figure 4.9A**). A concentration-dependent experiment showed that, at neutral pH and 37°C, lactate exhibits ~0.4% CEST/mM at 9.4T (**Figure 4.9B,C)**. The pH dependence of 30mM lactate at 9.4T showed maximum LATEST signal at pH=7 (**Figure 4.9D,E**). At both lower and higher pH, a decrease in LATEST asymmetry at 0.4ppm was observed.

The exchange rate (k) estimated from lactate phantoms (pH 7) at 25°C is ~350±50s^{-1} and at 37°C is ~550±50^{s-1}. Using the chemical shift determined by the high-resolution NMR experiments, 0.8ppm, the Δω at 7T is ~1000rad/s, and at 9.4T is ~2000rad/s. Therefore, the lactate chemical exchange rate is in the slow to intermediate condition (Δω ≥ k) and meets the requirement for observing the CEST effect for field strengths greater than 3T.

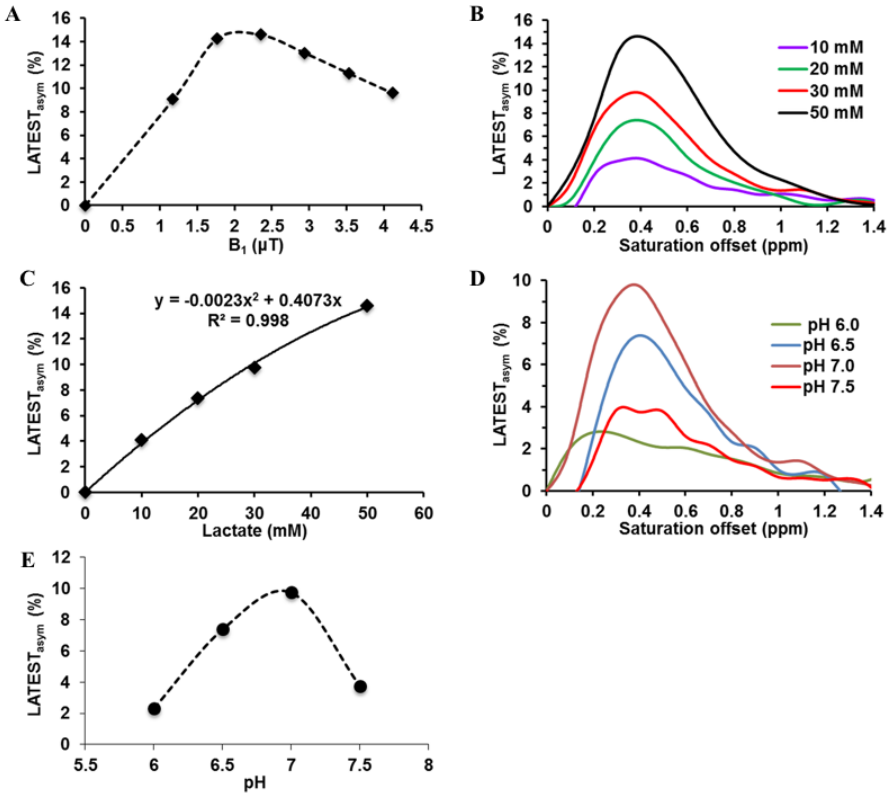

Figure 4.9 Characterization of LATEST. A) LATEST dependence on B_1 from a 50mM lactate phantom at pH 7, at the saturation duration of 0.4 ppm offset from water; B) asymmetry plot of LATEST at 10, 20, 30, and 50mM lactate at pH 7, with B_{1rms}=2.35μT and pulse duration=5s; C) concentration dependence of LATEST at 0.4ppm, pH 7, with B_{1rms}=2.35μT and pulse duration=5s; D) asymmetry plots from 30mM lactate, pH =6, 6.5, 7, and 7.5 E) pH dependence of LATEST at 0.4 ppm from 30mM lactate with B_{1rms}=2.35μT, duration =5s. All data acquired at 37°C, 9.4T. *(Reprinted with permission (DeBrosse, Nanga et al. 2016).)*

4.3.2 Animal model studies

LATEST imaging of lymphoma flank tumors. Anatomical images of flank tumors on three mice are shown in **Figure 4.10 A-C**. For each animal, we first acquired CEST images of the tumor region for several minutes in order to establish a baseline $LATEST_{asym}$. Baseline CEST maps from the tumor regions (**Figure 4.10 D-F**) showed an average $LATEST_{asym}$ of ~3.5%. Following infusion of 300mM pyruvate through the tail vein, the LATEST signal increased in the tumor regions (**Figure 4.10 G-I**).

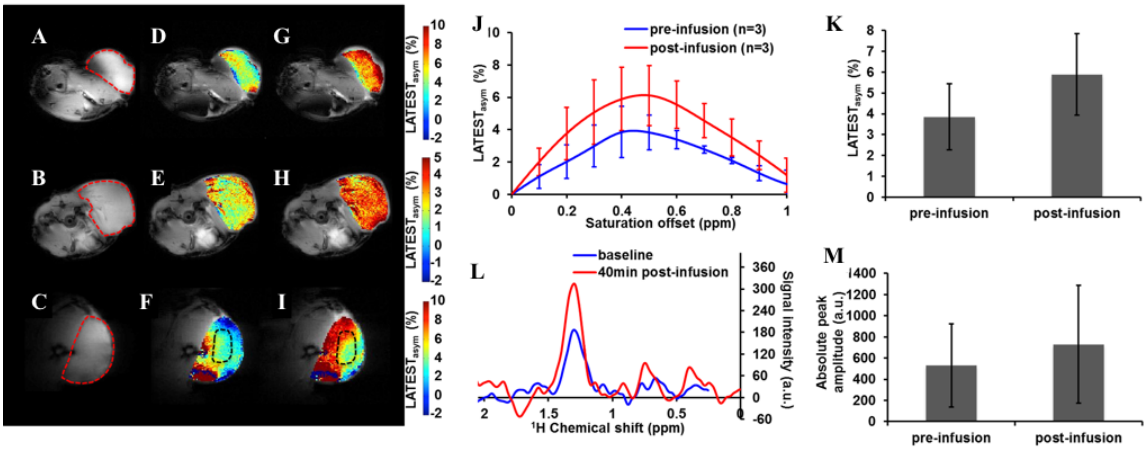

Figure 4.10 LATEST from lymphoma tumors. A-C) Anatomical image from three animals, with flank tumor region indicated by dotted red line, and the LATEST maps; D-F) pre-infusion and (g-i) post-infusion with J) corresponding asymmetry plots (asymmetry from Animal 3 in the third row is taken from region indicated in dotted black line), K) LATEST change at 0.4ppm from three animals pre- and post-infusion, l) representative SEL-MQC 1H-MRS pre- and 40 minutes post-infusion from flank tumor showing M) increase in lactate peak amplitude from three animals (~40%) from spectroscopy. *(Reprinted with permission (DeBrosse, Nanga et al. 2016).)*

This increase is challenging to visualize in the z-spectra from the animal tumors, but, analogous to the phantom study, the increased lactate post-infusion is readily apparent in the asymmetry plots. Average asymmetry plots from the tumor regions (**Figure 4.10J**) showed an endogenous LATEST peak and subsequent increase post-infusion, centered ~0.5ppm downfield from water. The asymmetry plot from one animal (row 3 of **Figure 4.10 A-I**) was obtained from the region of interest (ROI) indicated in the black dotted line (**Figure 4.10 F**). This region was used in order to avoid regions with large B_0 inhomogeneity, which was observed in the outer region of the tumor (**Figure 4.11**).

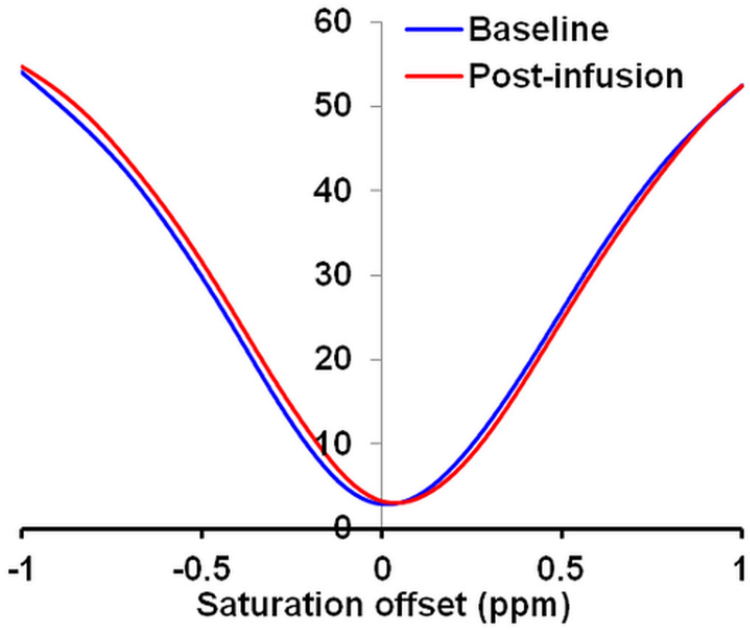

Figure 4.11 Z-spectra from the tumor region in a representative animal.

Z-spectra were compared pre- and post-infusion of pyruvate.

Data from lymphoma tumors of three animals showed a ~60% increase in LATEST asymmetry ~40 minutes post-infusion of pyruvate (**Figure 4.10K**). *In vivo* LATEST imaged from the animal tumors were corrected for B_0 and B_1 inhomogeneity (**Figure 4.12).**

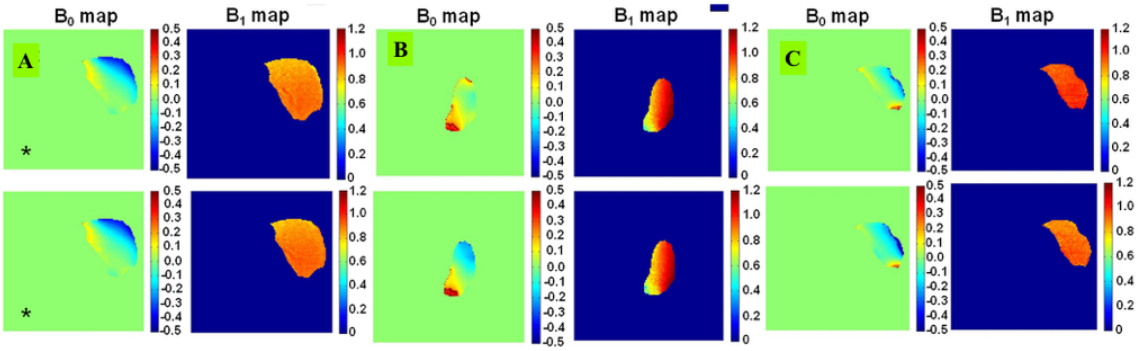

Figure 4.12 pre- and post-infusion B_0 and B_1 maps for three animals with flank tumors. *B_0 map is identical for pre- and post-infusion. No center frequency change, no animal movement.

In tumors, endogenous lactate levels are expected to be in the range of 2 to 10 mM (Lee, Huang et al. 2008). Baseline LATEST observed in the tumor model is largely due to endogenous lactate, based on the ~0.4% LATEST asymmetry per mM of lactate observed in phantoms at 9.4T. The increase in $LATEST_{asym}$ post-infusion is due to the conversion of pyruvate to lactate by the tumor tissue.

In order to validate the LATEST method, tumor lactate was also measured in three animals with flank tumors using SEL-MQC ^{1}H MRS. Spectroscopy results pre- and post-infusion of pyruvate are shown for a representative animal (**Figure 4.10 L**). The increase in lactate peak amplitude after pyruvate infusion shown by spectroscopy from all three animals (**Figure 4.10M**) showed a trend in lactate change that is similar to the trend observed with LATEST.

LATEST imaging of 9L rat brain tumor. We have also recently implemented LATEST in a rat brain model of glioma. The anatomical image of a representative rat brain is shown in **Fig 4.13A**. In the two baseline LATEST maps from the tumor region, we clearly observe higher LATEST contrast (~2.5%) than in the normal appearing brain region (~2%) **Fig 4.13B**. This difference is presumably due to the higher LDH expression in the tumor tissue. Additionally, the baseline LATEST contrast of 2-2.5% may arise from the myoinositol and other metabolites containing hydroxyl protons(Haris, Cai et al. 2011).

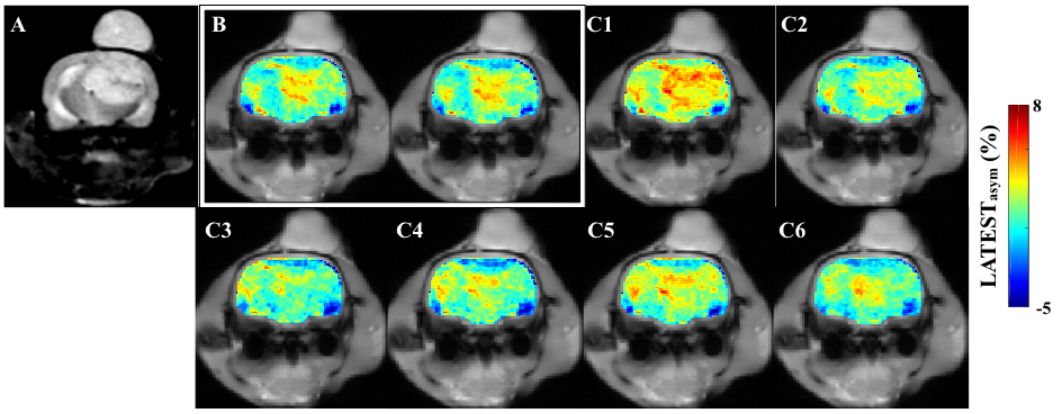

Figure 4.13 LATEST from 9L glioma rat brain model. A) anatomical coronal MRI image showing the brain tumor region, which extends outside of the skull; B) the two baseline LATEST images, with only the brain region segmented, that show higher signal than the healthy tissue; C1-6) post-infusion of pyruvate, an increase in LATEST is observed in the tumor region. Images were acquired for 90 minutes post-infusion, here we are showing 6 images with a temporal resolution of 15 min.

Following the infusion of pyruvate, the LATEST signal increased in the tumor region (**Fig 4.13C**) while no appreciable change in the LATEST signal was observed in the normal appearing brain region. Average asymmetry plots from the tumor region (**Fig. 4.14A**) pre- and post- pyruvate infusion showed an increase in the LATEST contrast post infusion which centered ~0.5ppm downfield from water. The asymmetry plots from the

normal appearing brain region showed no change in the LATEST following the infusion of pyruvate suggesting that normal brain region may not convert the pyruvate into lactate due to less LDH activity (**Fig 4.14B**).

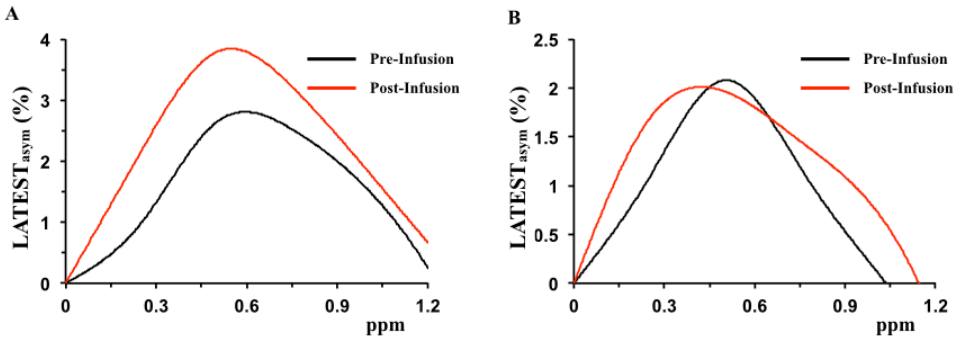

Figure 4.14 LATEST asymmetry plots from glioma model. A) pre- and post-infusion asymmetry from the tumor region; B) pre- and post-infusion asymmetry from the normal-appearing tissue.

4.3.3 Human studies: LATEST imaging of healthy human calf muscle

Healthy human calf muscle (**Figure 4.15A**) exhibited an average resting-state LATEST asymmetry of 1.5% (**Figure 4.15B**). This is consistent with the expected low concentration of endogenous lactate in muscle under resting conditions (Gaitanos, Williams et al. 1993). It also indicated that, with the experimental parameters used, contributions from any other endogenous metabolites to LATEST are negligibly small. After intensive, exhaustive exercise was performed by the subjects, the first LATEST image (acquired ~3 minutes after cessation of exercise) showed an increased LATEST asymmetry in exercising muscle (gastrocnemius muscle, activated through plantar

flexion) to ~4 - 7%, which recovered to baseline over period of 20 minutes (**Figure 4.15C**).

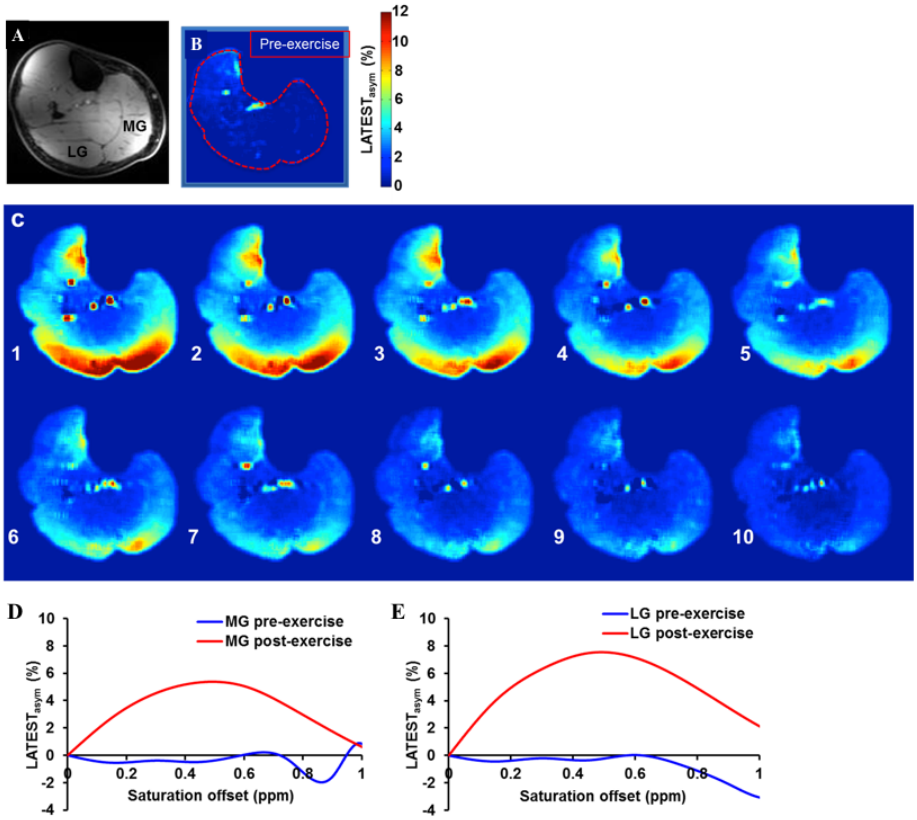

Figure 4.15 In vivo LATEST in healthy skeletal muscle. A) anatomical image of human calf muscle; B) two pre-exercise, resting-state CEST maps showing negligible LATEST signal at 0.4ppm, and C) after 3 minutes of exhaustive exercise, ten post-exercise images acquired over 18 minutes: the first image (C1) obtained 3 minutes after cessation of exercise shows a CEST asymmetry increase in the medial gastrocnemius (MG) and lateral gastrocnemius (LG) muscles of ~8%. Each of the subsequent images (C2-10), acquired with a resolution of 1.8 minutes, shows lactate recovery in the MG and LG. All LATEST images acquired using B1rms = 0.73μT and 3s duration; Asymmetry plots for pre- and post-exercise LATEST of the D) medial gastrocnemius (MG) and E) lateral gastrocnemius muscles from a representative subject, acquired with B_{1rms} = 0.73μT, 3s duration. *(Reprinted with permission (DeBrosse, Nanga et al. 2016).)*

Again, it is challenging to determine the lactate change from the z-spectra of the individual muscle regions. From the asymmetry analysis, however, it is clear that the lactate resonance is centered at ~0.5ppm (**Figure 4.16**).

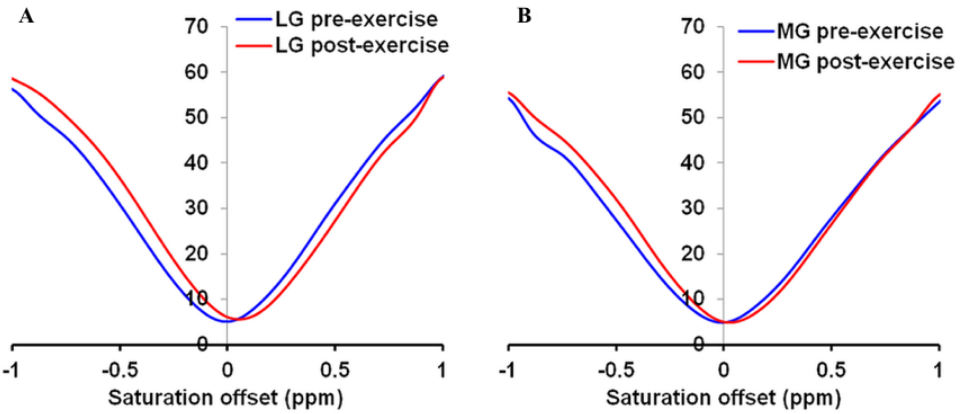

Figure 4.16 Z-spectra for skeletal muscle. A) Z-spectra for the lateral gastrocnemius muscle region, B) Z-spectra for the medial gastrocnemius muscle region, from a representative subject.

The asymmetry plots from the medial and lateral gastrocnemius muscles from a representative subject pre-exercise, and immediately post-exercise, are shown in **Figure 4.15 D-E**. Similar increase in post-exercise LATEST is consistently observed in all five of the healthy volunteers (**Figure 4.17A**). Again, like in the animal tumor experiments, we sought to validate the LATEST imaging method in vivo at 7T by performing the same exercise paradigm and measure lactate via spectroscopy. Lactate concentration derived from SEL-MQC based edited spectra (**Figure 4.17B**) pre- and post-exercise from 3 healthy volunteers exhibited the same trend (**Figure 4.17C**) as the LATEST imaging-

derived lactate. The LATEST correlates well (R^2 =0.97) with lactate spectral area (**Figure 4.17D**). Based on the slope value of ~0.29% per mM of lactate from spectroscopy, we estimate post-exercise muscle lactate levels to be approximately 14-25 mM. These results are consistent with reported lactate concentration increase of ~20mM measured in muscle biopsy after intense exercise (Bangsbo, Johansen et al. 1993).

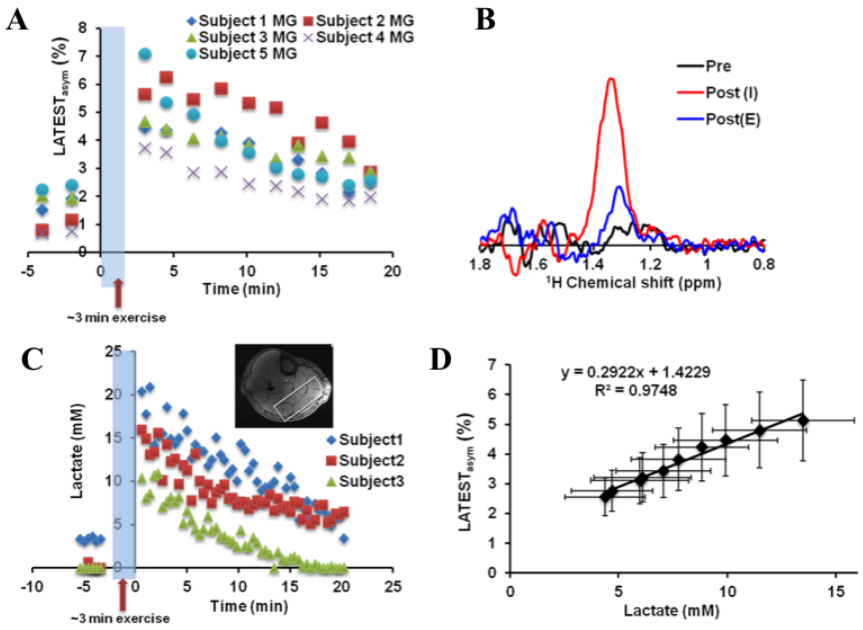

Figure 4.17 In vivo LATEST and SEL-MQC spectroscopy. A) LATEST at 0.4ppm in the medial gastrocnemius (MG) of resting-state calf muscle, and post-exercise recovery from 5 healthy volunteers; B) representative lactate MRS in a voxel from the MG/LG pre-exercise, immediately post-exercise, and after 20 minutes of recovery, and C) pre- and post-exercise lactate edited MRS data from 3 healthy volunteers (representative voxel location from one subject shown in insert); D) correlation of lactate concentration from spectroscopy and LATEST from the MG. Error bars indicate standard error. *(Reprinted with permission (DeBrosse, Nanga et al. 2016).)*

As in the animal tumors, a key component of post-processing the LATEST data was accurate correction for B_0 and B_1 inhomogeneities (**Figure 4.18).** Because the lactate resonance is so close to the bulk water peak, the LATEST images are very sensitive to any small inhomogeneity in the field or applied pulse.

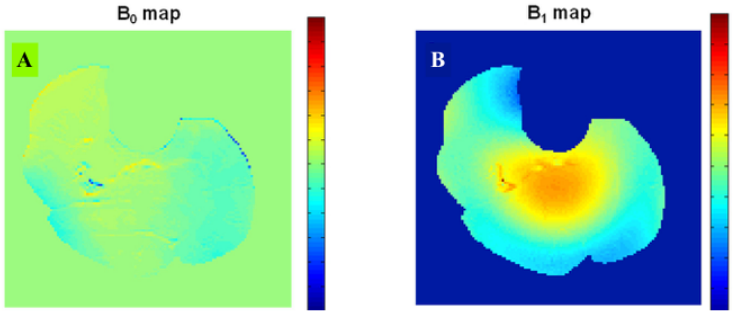

Figure 4.18 B_0 and B_1 correction of in vivo calf muscle CEST. A) B_0 (WASSR) map, acquired with B_{1rms} = 0.29μT and 200ms duration, collected from 0 ppm to ±0.5 ppm, in steps of 0.05ppm and B) B_1 GRE map for human calf muscle

We also considered that, due to the intense exercise performed for these experiments, there was the possibility of muscle T_2 changes, which could confound the LATEST results. To address this issue, we computed T_2 maps of skeletal muscle under identical exercising conditions and found that T_2 is elevated by <10% immediately after exercise, and stayed constant over 20 minutes (**Figure 4.19**). We estimated that this very small change in the T_2 would have a negligible contribution to LATEST.

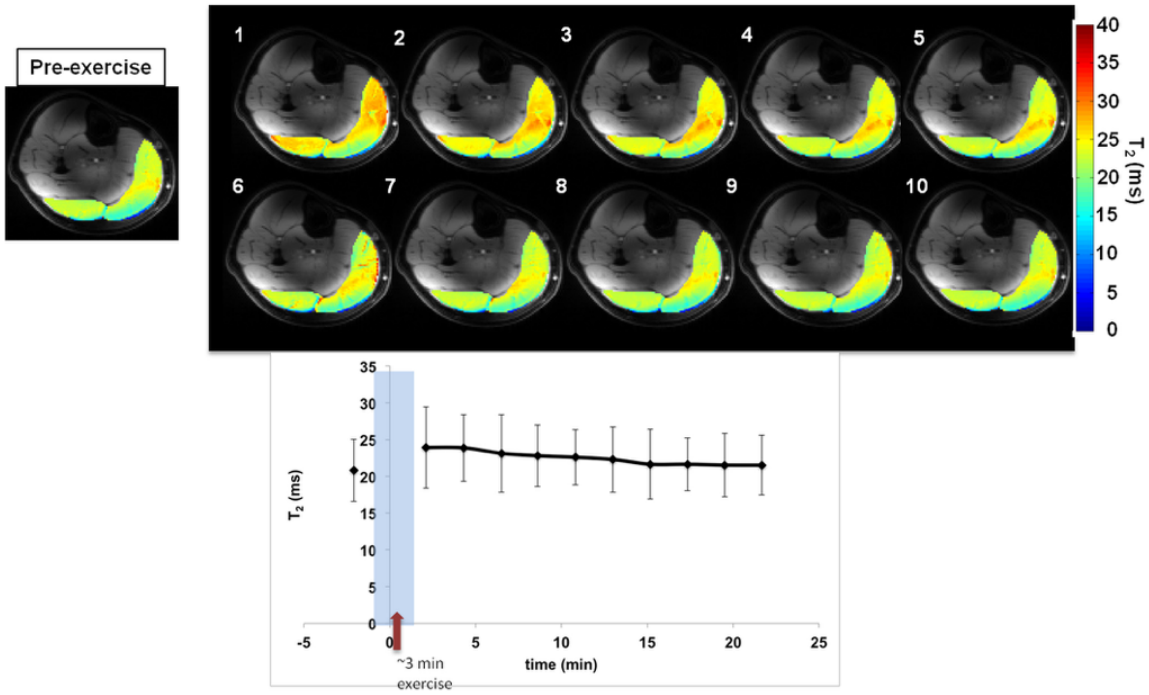

Figure 4.19 Gastrocnemius muscle T_2 measurements. A) T2 maps overlaid on the anatomical image before exercise, and B) T2 maps post-exercise, acquired with the same time resolution as the LATEST images; C) T2 value in ms vs. recovery time in minutes.

4.4 Discussion

The results presented on phantoms, tumor model, and skeletal muscle demonstrate the feasibility of lactate measurement with the LATEST technique. Based on the results of the phantom experiments, we chose B_1 parameters that provide optimal CEST effect at 0.4ppm. The application of this method in tumors was demonstrated in **Figure 4.10** in a lymphoma mouse model. As discussed in the introduction of this chapter, elevated tumor

lactate levels contribute to cancer progression and are correlated with poor patient outcome. With LATEST, we can investigate tumor glycolysis through injection of non-enriched pyruvate or glucose. For the mouse tumor studies, due to long acquisition times, we have acquired LATEST only at one time point following the infusion of pyruvate solution in tumors. However, with further optimization of the protocol it is feasible to gather time dependent data post-infusion.

When developing new CEST biomarkers, it is necessary to consider other possible contributions to the CEST signal. Due to the presence of –OH groups from other endogenous molecules (glucose, glycogen, etc.) it is possible that the baseline, endogenous LATEST signal may have contributions from these molecules. Although we have demonstrated the LATEST measurement pre- and post- pyruvate infusion, similar studies can be performed using glucose infusion. Previous studies with GlucoCEST have shown that there is a measurable GlucoCEST contrast in tumors after glucose infusion, which has been attributed primarily to the extracellular glucose (Chan, McMahon et al. 2012, Walker-Samuel, Ramasawmy et al. 2013). However, it has recently been speculated that this increased signal may also be due to the byproducts of glycolysis, including lactate (Wang, Weygand et al. 2016). Furthermore, as shown previously, -OH groups from glucose and glycogen have resonances at around 1 ppm as opposed to ~0.4ppm in the case of lactate (van Zijl, Jones et al. 2007, Yadav, Xu et al. 2014). Other metabolites that may be present in tumors, such as pyruvate, do not have exchangeable hydroxyl protons, and would not be expected to contribute to the LATEST signal at 0.4ppm. Thus, LATEST and GlucoCEST are expected to provide complementary

information from tumors. The addition of LATEST to the available tools for studying tumor glycolysis *in vivo* will be beneficial when used to complement existing methods.

In skeletal muscle, we must consider the possible contribution of creatine to the LATEST signal. The creatine CEST experiments in chapter 2 demonstrated that the guanidine protons of creatine resonate farther downfield at 1.8ppm from bulk water, and require a much shorter saturation pulse (500ms) and higher B_1 power of 2.9μT. Furthermore, if creatine contributed to the LATEST effect at ~0.5ppm, we would have observed higher signal in the resting state skeletal muscle. Additionally, increased post-exercise creatine has been shown to recover within ~2 minutes, which is much shorter than the ~18 minutes it takes for the LATEST signal to dissipate post-exercise. Based on *in vivo* asymmetry plots presented in **Figure 4.15**, and the intercept in **Figure 4.17**, the contributions to LATEST from other metabolites are small with the given saturation parameters. The primary use of the LATEST method is in the dynamic measurement of changes in lactate, like in pyruvate or glucose infusion in tumor, post-exercising muscle experiments.

The major advantage of this method is that it is not affected by lipid resonances that confound ^{1}H-MRS- derived lactate. In addition, this method has a sensitivity enhancement of two orders of magnitude compared to conventional ^{1}H-MRS-based detection of lactate. Considering the sensitivity differences in ^{13}C and ^{1}H, LATEST sensitivity is comparable to DNP. We have demonstrated the feasibility of LATEST *in vivo* at both 9.4T and 7T.

While there are clear advantages of LATEST imaging compared to other methods, there are also some challenges to address. Because the hydroxyl protons of lactate resonate so close to the large water peak, there is a greater effect of direct saturation. A robust B_0 correction method is required for LATEST. In this work, the images were corrected for B_0 and B_1 inhomogeneities prior to computation of CEST asymmetry. We observed that any significant drift of the center frequency was typically due to the intense exercise in our skeletal muscle experiments and resulting movement of the leg. Post-exercise "checking" of the center frequency is a step that was not required for CrCEST studies where only mild exercise was performed, and significant subject motion rarely observed. Furthermore, a small center frequency drift is more easily corrected in post-processing for CrCEST images as there is less contribution from DS confounding the signal. Here, we were careful to monitor and record any major changes in the center frequency to ensure CEST pulse saturation accuracy at 0.5ppm. Another potential limitation of LATEST when considering clinical translation is that this must be performed at high-field strength (≥7T), due to the close proximity of the peak to the bulk water peak. Despite this, LATEST has significant potential for research studies at high fields, particularly for animal studies.

4.5 Summary

Through studies of phantoms, animal models of tumors, and in exercising human skeletal muscle, we demonstrated that the LATEST method enables high-resolution imaging of lactate *in vivo*, without requiring the use of expensive contrast agents. In terms of sensitivity, the LATEST method out-performs conventional ^{1}H-MRS. Given the increasing availability of 7T MRI scanners, the LATEST method can be translated into clinical research settings to study patients with cancer and other metabolic diseases. Potential applications of the method include: tumors diagnosis, probing tumor glycolytic activity, and monitoring of response to therapies in cancer and a variety of metabolic disorders.

Thesis summary and future directions

In Chapter 1, we explored the motivation for developing novel MRI techniques for molecular imaging, and presented two pathways (OXPHOS and glycolysis) that are of particular interest in studies of metabolic dysfunction. The goal for this dissertation work was to develop and optimize CEST MRI techniques, which allow for noninvasive measurements of small metabolites. The benefits of CEST, compared to traditional spectroscopic techniques and imaging modalities such as PET, include significant signal enhancement and high spatial resolution, without use of invasive contrast agents or radioactive ligands. In Chapter 2, we focused on creatine, which serves as a marker of OXPHOS and therefore mitochondrial function in exercising skeletal muscle. Building upon the initial development of CrCEST, we performed a small reproducibility study in healthy skeletal muscle at clinical field strength (3T), and built new MRI-compatible,

MRI-safe, exercise equipment. We then performed a high-field (7T) study in patients with primary mitochondrial disorders and other inborn errors of metabolism, detailed in Chapter 3. The results of this work showed that CrCEST has the capability to distinguish between healthy exercising muscle and muscle that contains impaired mitochondria. The high spatial resolution of CrCEST allowed for assessment of several muscle groups simultaneously, providing a more comprehensive "snapshot" of the entire muscle than could previously be obtained within a clinical timeframe. In future, CrCEST imaging has potential use in other metabolic disease such as diabetes and cardiac disease. We are currently working on implementing CrCEST in muscle of cardiac disease patients, and optimizing the technique in order to reduce scan time for application in cardiac tissue in humans.

The second goal for this dissertation work was to develop a CEST biomarker for glycolysis. Previously, glucose was targeted for CEST imaging as it is the "fuel" for cancer cells and therefore provides information on tumor metabolism. However, there has been some debate about the specificity of that measurement, as the products of glycolysis could also contribute to the measured signal. With that in mind, we developed CEST imaging of lactate (LATEST) to provide another tool for probing the complexities of cancer metabolism (Chapter 4). We first demonstrated feasibility of measuring lactate with CEST in phantom experiments at 7T and 9.4T, and then validated that this technique could detect lactate *in vivo* by measuring the LATEST signal in intensely exercised human skeletal muscle at 7T. Then we implemented LATEST in a tumor models in mice at 9.4T, and detected changes in lactate upon infusion of its precursor, pyruvate. The

pyruvate used in our studies was unlabeled, and therefore cheaper and safer than labeled pyruvate used in other modalities. We validated both our muscle and tumor *in vivo* studies by comparing to spectroscopically-derived measures of lactate, which showed good agreement with the LATEST measurements. In addition to the enhanced sensitivity of our method, we predict that in future studies, the high spatial resolution of LATEST might provide more information than previous methods when imaging heterogeneous tumor tissue and assessing therapeutic efficacy.

Taken together, these studies demonstrate that CEST can be used to study two different metabolic pathways, glycolysis and OXPHOS, and are particularly useful in dynamic studies where we predict a change in metabolite concentration due to metabolic disruption. With further development and application of these techniques, CEST imaging has the potential for clinical translation, and will benefit research studies across a variety of disciplines.

Bibliography

Abergel, D. and A. G. Palmer (2004). "Approximate solutions of the Bloch-McConnell equations for two-site chemical exchange." Chemphyschem **5**(6): 787-793.

Abrahams, J. P., A. G. W. Leslie, R. Lutter and J. E. Walker (1994). "Structure at 2.8-angstrom resolution of f1-atpase from bovine heart-mitochondria." Nature **370**(6491): 621-628.

Abramov, A. Y., A. Scorziello and M. R. Duchen (2007). "Three distinct mechanisms generate oxygen free radicals in neurons and contribute to cell death during anoxia and reoxygenation." Journal of Neuroscience **27**(5): 1129-1138.

Adeva, M., M. Gonzalez-Lucan, M. Seco and C. Donapetry (2013). "Enzymes involved in L-lactate metabolism in humans." Mitochondrion **13**(6): 615-629.

Agatston, A. S., W. R. Janowitz, F. J. Hildner, N. R. Zusmer, M. Viamonte and R. Detrano (1990). "Quantification of coronary-artery calcium using ultrafast computed-tomography." Journal of the American College of Cardiology **15**(4): 827-832.

Aime, S., M. Botta and E. Terreno (2005). "Gd(III)-based contrast agents for MRI." Advances in Inorganic Chemistry - Including Bioinorganic Studies, Vol 57 **57**: 173-237.

Aime, S., C. Carrera, D. Delli Castelli, S. G. Crich and E. Terreno (2005). "Tunable imaging of cells labeled with MRI-PARACEST agents." Angewandte Chemie-International Edition **44**(12): 1813-1815.

Aime, S., F. Fedeli, A. Sanino and E. Terreno (2006). "A R-2/R-1 ratiometric procedure for a concentration-independent, pH-responsive, Gd(III)-based MRI agent." Journal of the American Chemical Society **128**(35): 11326-11327.

Albert, M. S., G. D. Cates, B. Driehuys, W. Happer, B. Saam, C. S. Springer and A. Wishnia (1994). "Biological magnetic-resonance-imaging using laser polarized XE-129." Nature **370**(6486): 199-201.

Alberts, B., A. Johnson, J. Lewis, M. Raff, K. Roberts and P. Walter (2008). Molecular biology of the cell, 5th edition. 270 Madison Avenue, New York NY 10016, USA, Garland Science, Taylor & Francis Group, LLC.

Alsop, D. C. and J. A. Detre (1998). "Multisection cerebral blood flow MR imaging with continuous arterial spin labeling." Radiology **208**(2): 410-416.

Alston, C., C. Ceccatelli Berti, E. Blakely, M. Olahova, L. P. He, C. McMahon, S. Olpin, I. Hargreaves, C. Nolli, R. McFarland, P. Goffrini, M. O'Sullivan and R. W. Taylor (2015). "A recessive homozygous p.Asp92Gly SDHD mutation causes prenatal cardiomyopathy and a severe mitochondrial complex II deficiency." Human Genetics **134**(8): 869-879.

Alston, C. L., J. E. Davison, F. Meloni, F. H. van der Westhuizen, L. P. He, H. T. Hornig-Do, A. C. Peet, P. Gissen, P. Goffrini, I. Ferrero, E. Wassmer, R. McFarland and R. W. Taylor (2012). "Recessive germline SDHA and SDHB mutations causing leukodystrophy and isolated mitochondrial complex II deficiency." Journal of Medical Genetics **49**(9): 569-577.

Andreu, A. L., M. G. Hanna, H. Reichmann, C. Bruno, A. S. Penn, K. Tanji, F. Pallotti, S. Iwata, E. Bonilla, B. Lach, J. Morgan-Hughes and S. DiMauro (1999). "Exercise

intolerance due to mutations in the cytochrome b gene of mitochondrial DNA." New England Journal of Medicine **341**(14): 1037-1044.
Andreyev, A. I., Y. E. Kushnareva and A. A. Starkov (2005). "Mitochondrial metabolism of reactive oxygen species." Biochemistry-Moscow **70**(2): 200-214.
Argov, Z. and W. J. Bank (1991). "Phosphorous magnetic-resonance spectroscopy (P-31 MRS) in neuromuscular disorders." Ann Neurol **30**(1): 90-97.
Arnold, D. L., D. J. Taylor and G. K. Radda (1985). "Investigation of human mitochondrial myopathies by phosphorus magnetic resonance spectroscopy." Ann Neurol **18**(2): 189-196.
Babior, B. M. (2000). "The NADPH oxidase of endothelial cells." Iubmb Life **50**(4-5): 267-269.
Bagga, P., R. Crescenzi, G. Krishnamoorthy, G. Verma, R. P. R. Nanga, D. Reddy, J. Greenberg, J. A. Detre, H. Hariharan and R. Reddy (2016). "Mapping the alterations in glutamate with GIuCEST MRI in a mouse model of dopamine deficiency." Journal of Neurochemistry **139**(3): 432-439.
Bajpeyi, S., M. Pasarica, C. Moro, K. Conley, S. Jubrias, O. Sereda, D. H. Burk, Z. Zhang, A. Gupta, L. Kjems and S. R. Smith (2011). "Skeletal Muscle Mitochondrial Capacity and Insulin Resistance in Type 2 Diabetes." Journal of Clinical Endocrinology & Metabolism **96**(4): 1160-1168.
Ballinger, S. W., J. M. Shoffner, S. Gebhart, D. A. Koontz and D. C. Wallace (1994). "Mitochondrial diabetes revisited." Nature Genetics **7**(4): 458-459.
Bangsbo, J., L. Johansen, T. Graham and B. Saltin (1993). "Lactate and h+ effluxes from human skeletal-muscles during intense, dynamic exercise." Journal of Physiology-London **462**: 115-133.
Barile, J. P., B. B. Reeve, A. W. Smith, M. M. Zack, S. A. Mitchell, R. Kobau, D. F. Cella, C. Luncheon and W. W. Thompson (2013). "Monitoring population health for Healthy People 2020: evaluation of the NIH PROMIS(R) Global Health, CDC Healthy Days, and satisfaction with life instruments." Qual Life Res **22**(6): 1201-1211.
Bates, M. G., K. G. Hollingsworth, J. H. Newman, D. G. Jakovljevic, A. M. Blamire, G. A. MacGowan, B. D. Keavney, P. F. Chinnery, D. M. Turnbull, R. W. Taylor, M. I. Trenell and G. S. Gorman (2013). "Concentric hypertrophic remodelling and subendocardial dysfunction in mitochondrial DNA point mutation carriers." Eur Heart J Cardiovasc Imaging **14**(7): 650-658.
Bayot, A., R. Santos, J. M. Camadro and P. Rustin (2011). "Friedreich's ataxia: the vicious circle hypothesis revisited." Bmc Medicine **9**: 8.
Bendahan, D., B. Giannesini and P. J. Cozzone (2004). "Functional investigations of exercising muscle: a noninvasive magnetic resonance spectroscopy-magnetic resonance imaging approach." Cellular and Molecular Life Sciences **61**(9): 1001-1015.
Bergman, B. C., E. E. Wolfel, G. E. Butterfield, G. D. Lopaschuk, G. A. Casazza, M. A. Horning and G. A. Brooks (1999). "Active muscle and whole body lactate kinetics after endurance training in men." Journal of Applied Physiology **87**(5): 1684-1696.
Blake, P., B. Johnson and J. W. VanMeter (2003). "Positron emission tomography (PET) and single photon emission computed tomography (SPECT): Clinical applications." Journal of Neuro-Ophthalmology **23**(1): 34-41.

Boffoli, D., S. C. Scacco, R. Vergari, G. Solarino, G. Santacroce and S. Papa (1994). "Decline with age of the respiratory-chain activity in human skeletal-muscle." Biochimica Et Biophysica Acta-Molecular Basis of Disease **1226**(1): 73-82.
Bottomley, P. A., Y. H. Lee and R. G. Weiss (1997). "Total creatine in muscle: Imaging and quantification with proton MR spectroscopy." Radiology **204**(2): 403-410.
Boveris, A. and B. Chance (1973). "Mitochondrial generation of hydrogen-peroxide - general properties and effect of hyperbaric-oxygen." Biochemical Journal **134**(3): 707-716.
Boveris, A., B. Chance and N. Oshino (1972). "Cellular production of hydrogen-peroxide." Biochemical Journal **128**(3): 617-&.
Brizel, D. M., T. Schroeder, R. L. Scher, S. Walenta, R. W. Clough, M. W. Dewhirst and W. Mueller-Klieser (2001). "Elevated tumor lactate concentrations predict for an increased risk of metastases in head-and-neck cancer." International Journal of Radiation Oncology Biology Physics **51**(2): 349-353.
Bryant, R. G. (1996). "The dynamics of water-protein interactions." Annual Review of Biophysics and Biomolecular Structure **25**: 29-53.
Burt, C. T., T. Glonek and M. Barany (1976). "Analysis of phosphate metabolites, intracellular pH, and state of adenosine-triphosphate in intact muscle by phosphorous nuclear magnetic-resonance." Journal of Biological Chemistry **251**(9): 2584-2591.
Burt, C. T., T. Glonek and M. Barany (1977). "Analysis of living tissue by phosphorus-31 magnetic resonance." Science **195**(4274): 145-149.
Cadenas, E. and K. J. A. Davies (2000). "Mitochondrial free radical generation, oxidative stress, and aging." Free Radical Biology and Medicine **29**(3-4): 222-230.
Cai, K. J., M. Haris, A. Singh, F. Kogan, J. H. Greenberg, H. Hariharan, J. A. Detre and R. Reddy (2012). "Magnetic resonance imaging of glutamate." Nature Medicine **18**(2): 302-306.
Cai, K. J., A. Singh, H. Poptani, W. G. Li, S. L. Yang, Y. Lu, H. Hariharan, X. H. J. Zhou and R. Reddy (2015). "CEST signal at 2ppm (CEST@2ppm) from Z-spectral fitting correlates with creatine distribution in brain tumor." Nmr in Biomedicine **28**(1): 1-8.
Cain, D. F. and R. E. Davies (1962). "Breakdown of adenosine triphosphate during a single contraction of working muscle." Biochem Biophys Res Commun **8**(5): 361-&.
Caravan, P., J. J. Ellison, T. J. McMurry and R. B. Lauffer (1999). "Gadolinium(III) chelates as MRI contrast agents: Structure, dynamics, and applications." Chemical Reviews **99**(9): 2293-2352.
Carrer, A. and K. E. Wellen (2015). "Metabolism and epigenetics: a link cancer cells exploit." Current Opinion in Biotechnology **34**: 23-29.
Cecchini, G. (2003). "Function and structure of complex II of the respiratory chain." Annual Review of Biochemistry **72**: 77-109.
Chan, K. W. Y., M. T. McMahon, Y. Kato, G. S. Liu, J. W. M. Bulte, Z. M. Bhujwalla, D. Artemov and P. C. M. van Zijl (2012). "Natural D-glucose as a biodegradable MRI contrast agent for detecting cancer." Magnetic Resonance in Medicine **68**(6): 1764-1773.
Chance, B. and W. Bank (1995). "Genetic disease of mitochondrial function evaluated by NMR and NIR spectroscopy of skeletal tissue." Biochim Biophys Acta **1271**(1): 7-14.

Chance, B., S. Eleff, J. S. Leigh, D. Sokolow and A. Sapega (1981). "Mitochondrial regulation of phosphocreatine inorganic-phosphate ratios in exercising human-muscle - a gated P-31 NMR-study." Proceedings of the National Academy of Sciences of the United States of America-Biological Sciences **78**(11): 6714-6718.
Chance, B., B. Schoener, R. Oshino, F. Itshak and Y. Nakase (1979). "Oxidation-reduction ratio studies of mitochondria in freeze-trapped samples - nadh and flavoprotein fluorescence signals." Journal of Biological Chemistry **254**(11): 4764-4771.
Chance, B., H. Sies and A. Boveris (1979). "Hydroperoxide metabolism in mammalian organs." Physiological Reviews **59**(3): 527-605.
Chance, B. and G. R. Williams (1955). "Respiratory enzymes in oxidative phosphorylation .3. The steady state." Journal of Biological Chemistry **217**(1): 409-427.
Chance, B. and G. R. Williams (1956). "The respiratory chain and oxidative phosphorylation." Advances in Enzymology and Related Subjects of Biochemistry **17**: 65-134.
Chauvin, T., P. Durand, M. Bernier, H. Meudal, B. T. Doan, F. Noury, B. Badet, J. C. Beloeil and E. Toth (2008). "Detection of enzymatic activity by PARACEST MRI: A general approach to target a large variety of enzymes." Angewandte Chemie-International Edition **47**(23): 4370-4372.
Chen, A. P., M. J. Albers, C. H. Cunningham, S. J. Kohler, Y. F. Yen, R. E. Hurd, J. Tropp, R. Bok, J. M. Pauly, S. J. Nelson, J. Kurhanewicz and D. B. Vigneron (2007). "Hyperpolarized c-13 spectroscopic imaging of the TRAMP mouse at 3T - Initial experience." Magnetic Resonance in Medicine **58**(6): 1099-1106.
Chiolero, R. L., J. P. Revelly, X. Leverve, P. Gersbach, M. C. Cayeux, M. M. Berger and L. Tappy (2000). "Effects of cardiogenic shock on lactate and glucose metabolism after heart surgery." Critical Care Medicine **28**(12): 3784-3791.
Christiansen, J. P. and J. R. Lindner (2005). "Molecular and cellular imaging with targeted contrast ultrasound." Proceedings of the Ieee **93**(4): 809-818.
Cochran, A. J., M. E. Percival, S. Tricarico, J. P. Little, N. Cermak, J. B. Gillen, M. A. Tarnopolsky and M. J. Gibala (2014). "Intermittent and continuous high-intensity exercise training induce similar acute but different chronic muscle adaptations." Exp Physiol **99**(5): 782-791.
Cohn, M. and T. R. Hughes (1962). "Nuclear magnetic resonance spectra of adenosine d- and triphosphate .2. Effect of complexing with divalent metal ions." Journal of Biological Chemistry **237**(1): 176-&.
Comment, A., B. van den Brandt, K. Uffmann, F. Kurdzesau, S. Jannin, J. A. Konter, P. Hautle, W. T. H. Wenckebach, R. Gruetter and J. J. van der Klink (2007). "Design and performance of a DNP prepolarizer coupled to a rodent MRI scanner." Concepts in Magnetic Resonance Part B-Magnetic Resonance Engineering **31B**(4): 255-269.
Conley, K. E., S. A. Jubrias and P. C. Esselman (2000). "Oxidative capacity and ageing in human muscle." Journal of Physiology-London **526**(1): 203-210.
Coskun, P., J. Wyrembak, S. E. Schriner, H. W. Chen, C. Marciniack, F. LaFerla and D. C. Wallace (2012). "A mitochondrial etiology of Alzheimer and Parkinson disease." Biochimica Et Biophysica Acta-General Subjects **1820**(5): 553-564.

Couillard-Despres, S., R. Finkl, B. Winner, S. Ploetz, D. Wiedermann, R. Aigner, U. Bogdahn, J. Winkler, M. Hoehn and L. Aigner (2008). "In vivo optical imaging of neurogenesis: Watching new neurons in the intact brain." Molecular Imaging **7**(1): 28-34.
Cree-Green, M., B. R. Newcomer, M. Brown, A. Hull, A. D. West, D. Singel, J. E. B. Reusch, K. McFann, J. G. Regensteiner and K. J. Nadeau (2014). "Method for Controlled Mitochondrial Perturbation during Phosphorus MRS in Children." Medicine and Science in Sports and Exercise **46**(10): 2030-2036.
Crescenzi, R., C. DeBrosse, R. P. R. Nanga, M. D. Byrne, G. Krishnamoorthy, K. D'Aquilla, H. Nath, K. H. Morales, M. Iba, H. Hariharan, V. M. Y. Lee, J. A. Detre and R. Reddy (2017). "- Longitudinal imaging reveals subhippocampal dynamics in glutamate levels associated with histopathologic events in a mouse model of tauopathy and healthy mice." **- 27**(- 3): - 302.
Crescenzi, R., C. DeBrosse, R. P. R. Nanga, S. Reddy, M. Haris, H. Hariharan, M. Iba, V. M. Y. Lee, J. A. Detre, A. Borthakur and R. Reddy (2014). "In vivo measurement of glutamate loss is associated with synapse loss in a mouse model of tauopathy." Neuroimage **101**: 185-192.
Dang, C. V. (2010). "Rethinking the Warburg Effect with Myc Micromanaging Glutamine Metabolism." Cancer Research **70**(3): 859-862.
Davis, K. A., R. P. R. Nanga, S. Das, S. H. Chen, P. N. Hadar, J. R. Pollard, T. H. Lucas, R. T. Shinohara, B. Litt, H. Hariharan, M. A. Elliott, J. A. Detre and R. Reddy (2015). "Glutamate imaging (GluCEST) lateralizes epileptic foci in nonlesional temporal lobe epilepsy." Science Translational Medicine **7**(309).
Dawson, M. J., D. G. Gadian and D. R. Wilkie (1978). "Muscular fatigue investigated by phosphorous nuclear magnetic-resonance." Nature **274**(5674): 861-866.
Day, S. E., M. I. Kettunen, F. A. Gallagher, D. E. Hu, M. Lerche, J. Wolber, K. Golman, J. H. Ardenkjaer-Larsen and K. M. Brindle (2007). "Detecting tumor response to treatment using hyperpolarized C-13 magnetic resonance imaging and spectroscopy." Nature Medicine **13**(11): 1382-1387.
de Figueiredo, E., A. Borgonovi and T. M. Doring (2011). "Basic Concepts of MR Imaging, Diffusion MR Imaging, and Diffusion Tensor Imaging." Magnetic Resonance Imaging Clinics of North America **19**(1): 1-+.
de la Zerda, A., Z. A. Liu, S. Bodapati, R. Teed, S. Vaithilingam, B. T. Khuri-Yakub, X. Y. Chen, H. J. Dai and S. S. Gambhir (2010). "Ultrahigh Sensitivity Carbon Nanotube Agents for Photoacoustic Molecular Imaging in Living Mice." Nano Letters **10**(6): 2168-2172.
De Leon-Rodriguez, L. M., A. J. M. Lubag, C. R. Malloy, G. V. Martinez, R. J. Gillies and A. D. Sherry (2009). "Responsive MRI Agents for Sensing Metabolism in Vivo." Accounts of Chemical Research **42**(7): 948-957.
DeBerardinis, R. J. and N. S. Chandel (2016). "Fundamentals of cancer metabolism." Science Advances **2**(5): 18.
DeBerardinis, R. J., J. J. Lum, G. Hatzivassiliou and C. B. Thompson (2008). "The biology of cancer: Metabolic reprogramming fuels cell growth and proliferation." Cell Metabolism **7**(1): 11-20.

DeBerardinis, R. J., A. Mancuso, E. Daikhin, I. Nissim, M. Yudkoff, S. Wehrli and C. B. Thompson (2007). "Beyond aerobic glycolysis: Transformed cells can engage in glutamine metabolism that exceeds the requirement for protein and nucleotide synthesis." Proceedings of the National Academy of Sciences of the United States of America **104**(49): 19345-19350.
DeBerardinis, R. J., N. Sayed, D. Ditsworth and C. B. Thompson (2008). "Brick by brick: metabolism and tumor cell growth." Current Opinion in Genetics & Development **18**(1): 54-61.
DeBrosse, C., R. P. R. Nanga, P. Bagga, K. Nath, M. Haris, F. Marincola, M. D. Schnall, H. Hariharan and R. Reddy (2016). "Lactate Chemical Exchange Saturation Transfer (LATEST) Imaging in vivo A Biomarker for LDH Activity." Scientific Reports **6**: 9.
DeBrosse, C., R. P. R. Nanga, N. Wilson, K. D'Aquilla, M. Elliott, H. Hariharan, F. Yan, K. Wade, S. Nguyen, D. Worsley, C. Parris-Skeete, E. McCormick, R. Xiao, Z. Z. Cunningham, L. Fishbein, K. L. Nathanson, D. R. Lynch, V. A. Stallings, M. Yudkoff, M. J. Falk, R. Reddy and S. E. McCormack (2016). "Muscle oxidative phosphorylation quantitation using creatine chemical exchange saturation transfer (CrCEST) MRI in mitochondrial disorders." Jci Insight **1**(18).
Dickinson, W. C. (1951). "The Time Average Magnetic Field at the Nucleus in Nuclear Magnetic Resonance Experiments." Physical Review **81**(5): 717-731.
Dimauro, S., E. Bonilla, M. Zeviani, M. Nakagawa and D. C. Devivo (1985). "Mitochondrial myopathies." Annals of Neurology **17**(6): 521-538.
Dipple, K. M. and E. R. B. McCabe (2000). "Phenotypes of patients with "simple" mendelian disorders are complex traits: Thresholds, modifiers, and systems dynamics." American Journal of Human Genetics **66**(6): 1729-1735.
Doherty, J. R. and J. L. Cleveland (2013). "Targeting lactate metabolism for cancer therapeutics." Journal of Clinical Investigation **123**(9): 3685-3692.
Droge, W. (2002). "Free radicals in the physiological control of cell function." Physiological Reviews **82**(1): 47-95.
Duchen, M. R. (2004). "Roles of mitochondria in health and disease." Diabetes **53**: S96-S102.
Erez, A. and R. J. DeBerardinis (2015). "Metabolic dysregulation in monogenic disorders and cancer - finding method in madness." Nature Reviews Cancer **15**(7): 440-448.
Erez, A., O. A. Shchelochkov, S. E. Plon, F. Scaglia and B. Lee (2011). "Insights into the Pathogenesis and Treatment of Cancer from Inborn Errors of Metabolism." American Journal of Human Genetics **88**(4): 402-421.
Fantin, V. R., J. St-Pierre and P. Leder (2006). "Attenuation of LDH-A expression uncovers a link between glycolysis, mitochondrial physiology, and tumor maintenance." Cancer Cell **9**(6): 425-434.
Feldman, H. I., L. J. Appel, G. M. Chertow, D. Cifelli, B. Cizman, J. Daugirdas, J. C. Fink, E. D. Franklin-Becker, A. S. Go, L. L. Hamm, J. He, T. Hostetter, C. Y. Hsu, K. Jamerson, M. Joffe, J. W. Kusek, J. R. Landis, J. P. Lash, E. R. Miller, E. R. Mohler, 3rd, P. Muntner, A. O. Ojo, M. Rahman, R. R. Townsend and J. T. Wright (2003). "The Chronic Renal Insufficiency Cohort (CRIC) Study: Design and Methods." J Am Soc Nephrol **14**(7 Suppl 2): S148-153.

Fleischman, A., M. Kron, D. M. Systrom, M. Hrovat and S. K. Grinspoon (2009). "Mitochondrial function and insulin resistance in overweight and normal-weight children." J Clin Endocrinol Metab **94**(12): 4923-4930.
Folbergrova, J. and W. S. Kunz (2012). "Mitochondrial dysfunction in epilepsy." Mitochondrion **12**(1): 35-40.
Forsen, S. and R. A. Hoffman (1963). "Study of moderately rapid chemical exchange reactions by means of nuclear magnetic double resonance." Journal of Chemical Physics **39**(11): 2892-&.
Fridovich, I. (1995). "SUPEROXIDE RADICAL AND SUPEROXIDE DISMUTASES." Annual Review of Biochemistry **64**: 97-112.
Friedman, J. R. and J. Nunnari (2014). "Mitochondrial form and function." Nature **505**(7483): 335-343.
Frontera, W. R. and J. Ochala (2015). "Skeletal Muscle: A Brief Review of Structure and Function." Calcified Tissue International **96**(3): 183-195.
Gaitanos, G. C., C. Williams, L. H. Boobis and S. Brooks (1993). "Human muscle metabolism during intermittent maximal exercise." Journal of Applied Physiology **75**(2): 712-719.
Gerschman, R., D. L. Gilbert, S. W. Nye, P. Dwyer and W. O. Fenn (1954). "Oxygen poisoning and x-irradiation - a mechanism in common." Science **119**(3097): 623-626.
Giles, R. E., H. Blanc, H. M. Cann and D. C. Wallace (1980). "Maternal inheritance of human mitochondrial-dna." Proceedings of the National Academy of Sciences of the United States of America-Biological Sciences **77**(11): 6715-6719.
Gladden, L. B. (2004). "Lactate metabolism: a new paradigm for the third millennium." Journal of Physiology-London **558**(1): 5-30.
Glatz, C., K. D'Aco, S. Smith and N. Sondheimer (2011). "Mutation in the mitochondrial tRNA(Val) causes mitochondrial encephalopathy, lactic acidosis and stroke-like episodes." Mitochondrion **11**(4): 615-619.
Golman, K., R. in't Zandt, M. Lerche, R. Pehrson and J. H. Ardenkjaer-Larsen (2006). "Metabolic imaging by hyperpolarized C-13 magnetic resonance imaging for in vivo tumor diagnosis." Cancer Research **66**(22): 10855-10860.
Golman, K., R. in't Zandt and M. Thaning (2006). "Real-time metabolic imaging." Proceedings of the National Academy of Sciences of the United States of America **103**(30): 11270-11275.
Gorenstein, D. G. (1984). Phosphorous-31 NMR: principles and applications, Academic Press.
Goto, Y., I. Nonaka and S. Horai (1990). "A mutation in the transfer rnaleu(uur) gene associated with the melas subgroup of mitochondrial encephalomyopathies." Nature **348**(6302): 651-653.
Gray, M. W., G. Burger and B. F. Lang (1999). "Mitochondrial evolution." Science **283**(5407): 1476-1481.
Gribbestad, I. S., S. B. Petersen, H. E. Fjosne, S. Kvinnsland and J. Krane (1994). "H-1-NMR spectroscopic characterization of perchloric-acid extracts from breast carcinomas and noninvolved breast-tissue." Nmr in Biomedicine **7**(4): 181-194.

Grivennikova, V. G., A. N. Kapustin and A. D. Vinogradov (2001). "Catalytic activity of NADH-ubiquinone oxidoreductase (Complex I) in intact mitochondria - Evidence for the slow active/inactive transition." Journal of Biological Chemistry **276**(12): 9038-9044.
Guenebaut, V., A. Schlitt, H. Weiss, K. Leonard and T. Friedrich (1998). "Consistent structure between bacterial and mitochondrial NADH : ubiquinone oxidoreductase (complex I)." Journal of Molecular Biology **276**(1): 105-112.
Hanahan, D. and R. A. Weinberg (2011). "Hallmarks of Cancer: The Next Generation." Cell **144**(5): 646-674.
Haris, M., K. J. Cai, A. Singh, H. Hariharan and R. Reddy (2011). "In vivo mapping of brain myo-inositol." Neuroimage **54**(3): 2079-2085.
Haris, M., R. P. R. Nanga, A. Singh, K. Cai, F. Kogan, H. Hariharan and R. Reddy (2012). "Exchange rates of creatine kinase metabolites: feasibility of imaging creatine by chemical exchange saturation transfer MRI." Nmr in Biomedicine **25**(11): 1305-1309.
Haris, M., K. Nath, K. J. Cai, A. Singh, R. Crescenzi, F. Kogan, G. Verma, S. Reddy, H. Hariharan, E. R. Melhem and R. Reddy (2013). "Imaging of glutamate neurotransmitter alterations in Alzheimer's disease." Nmr in Biomedicine **26**(4): 386-391.
Haris, M., A. Singh, K. Cai, K. Nath, R. Crescenzi, F. Kogan, H. Hariharan and R. Reddy (2013). "MICEST: A potential tool for non-invasive detection of molecular changes in Alzheimer's disease." Journal of Neuroscience Methods **212**(1): 87-93.
Haris, M., A. Singh, K. J. Cai, F. Kogan, J. McGarvey, C. DeBrosse, G. A. Zsido, W. R. T. Witschey, K. Koomalsingh, J. J. Pilla, J. A. Chirinos, V. A. Ferrari, J. H. Gorman, H. Hariharan, R. C. Gorman and R. Reddy (2014). "A technique for in vivo mapping of myocardial creatine kinase metabolism." Nature Medicine **20**(2): 209-214.
Hatefi, Y. (1985). "The mitochondrial electron-transport and oxidative-phosphorylation system." Annual Review of Biochemistry **54**: 1015-1069.
He, Q. H., D. C. Shungu, P. C. M. Vanzijl, Z. M. Bhujwalla and J. D. Glickson (1995). "Single-scan in-vivo lactate editing with complete lipid and water suppression by selective multiple-quantum-coherence transfer (sel-mqc) with application to tumors." Journal of Magnetic Resonance Series B **106**(3): 203-211.
Heiden, M. G. V., L. C. Cantley and C. B. Thompson (2009). "Understanding the Warburg Effect: The Metabolic Requirements of Cell Proliferation." Science **324**(5930): 1029-1033.
Hirschey, M. D., R. J. DeBerardinis, A. M. E. Diehl, J. E. Drew, C. Frezza, M. F. Green, L. W. Jones, Y. H. Ko, A. Le, M. A. Lea, J. W. Locasale, V. D. Longo, C. A. Lyssiotis, E. McDonnell, M. Mehrmohamadi, G. Michelotti, V. Muralidhar, M. P. Murphy, P. L. Pedersen, B. Poore, L. Raffaghello, J. C. Rathmell, S. Sivanand, M. G. Vander Heiden, K. E. Wellen and T. Target Validation (2015). "Dysregulated metabolism contributes to oncogenesis." Seminars in Cancer Biology **35**: S129-S150.
Holt, I. J., A. E. Harding, R. K. H. Petty and J. A. Morganhughes (1990). "A NEW Mitochondrial disease associated with mitochondrial-dna heteroplasmy." American Journal of Human Genetics **46**(3): 428-433.
Horiuchi, M., P. J. Fadel and S. Ogoh (2013). "Differential effect of sympathetic activation on tissue oxygenation in gastrocnemius and soleus muscles during exercise in humans." Exp Physiol.

Hoult, D. I., S. J. W. Busby, D. G. Gadian, G. K. Radda, R. E. Richards and P. J. Seeley (1974). "Observation of tissue metabolites using P-31 nuclear magnetic resonance." Nature **252**(5481): 285-287.
Hsu, P. P. and D. M. Sabatini (2008). "Cancer cell metabolism: Warburg and beyond." Cell **134**(5): 703-707.
Infante, A. A. and R. E. Davies (1965). "Effect of 2,4-dinitrofluorobenzene on activity of striated muscle." Journal of Biological Chemistry **240**(10): 3996-&.
Inoue, M., E. F. Sato, M. Nishikawa, A. M. Park, Y. Kira, I. Imada and K. Utsumi (2003). "Mitochondrial generation of reactive oxygen species and its role in aerobic life." Current Medicinal Chemistry **10**(23): 2495-2505.
Iotti, S., R. Lodi, C. Frassineti, P. Zaniol and B. Barbiroli (1993). "In-vivo assessment of mitochondrial functionality in human gastrocnemius-muscle by p-31 mrs - the role of ph in the evaluation of phosphocreatine and inorganic-phosphate recoveries from exercise." Nmr in Biomedicine **6**(4): 248-253.
Jackson, C. B., J. M. Nuoffer, D. Hahn, H. Prokisch, B. Haberberger, M. Gautschi, A. Haberli, S. Gallati and A. Schaller (2014). "Mutations in SDHD lead to autosomal recessive encephalomyopathy and isolated mitochondrial complex II deficiency." J Med Genet **51**(3): 170-175.
Jackson, C. B., J. M. Nuoffer, D. Hahn, H. Prokisch, B. Haberberger, M. Gautschi, A. Haberli, S. Gallati and A. Schaller (2014). "Mutations in SDHD lead to autosomal recessive encephalomyopathy and isolated mitochondrial complex II deficiency." Journal of Medical Genetics **51**(3): 170-175.
James, M. L. and S. S. Gambhir (2012). "A molecular imaging primer: modalities, imaging agents, and applications." Physiological Reviews **92**(2): 897-965.
Jeppesen, J. B., C. Mortensen, F. Bendtsen and S. Moller (2013). "Lactate metabolism in chronic liver disease." Scandinavian Journal of Clinical & Laboratory Investigation **73**(4): 293-299.
Jeppesen, T. D., M. Duno, M. Schwartz, T. Krag, J. Rafiq, F. Wibrand and J. Vissing (2009). "Short- and long-term effects of endurance training in patients with mitochondrial myopathy." Eur J Neurol **16**(12): 1336-1339.
Jia, G., R. Abaza, J. D. Williams, D. L. Zynger, J. Zhou, Z. K. Shah, M. Patel, S. Sammet, L. Wei, R. R. Bahnson and M. V. Knopp (2011). "Amide Proton Transfer MR Imaging of Prostate Cancer: A Preliminary Study." Journal of Magnetic Resonance Imaging **33**(3): 647-654.
Johnson, M. A., J. Polgar, D. Weightman and D. Appleton (1973). "Data on the distribution of fibre types in thirty-six human muscles. An autopsy study." J Neurol Sci **18**(1): 111-129.
Jordan, C. D., M. Saranathan, N. K. Bangerter, B. A. Hargreaves and G. E. Gold (2013). "Musculoskeletal MRI at 3.0 T and 7.0 T: A comparison of relaxation times and image contrast." European Journal of Radiology **82**(5): 734-739.
Jouvensal, L., P. G. Carlier and G. Bloch (1997). "Low visibility of lactate in excised rat muscle using double quantum proton spectroscopy." Magnetic Resonance in Medicine **38**(5): 706-711.

Kaplan, J. (1999). "Friedreich's ataxia is a mitochondrial disorder." Proc Natl Acad Sci U S A **96**(20): 10948-10949.
Karp, G. (2008). Cell and Molecular Biology John Wiley and Sons.
Kelley, D. E., J. He, E. V. Menshikova and V. B. Ritov (2002). "Dysfunction of mitochondria in human skeletal muscle in type 2 diabetes." Diabetes **51**(10): 2944-2950.
Kemp, G. J., M. Meyerspeer and E. Moser (2007). "Absolute quantification of phosphorus metabolite concentrations in human muscle in vivo by 31P MRS: a quantitative review." NMR Biomed **20**(6): 555-565.
Kennedy, B. W. C., M. I. Kettunen, D.-E. Hu and K. M. Brindle (2012). "Probing Lactate Dehydrogenase Activity in Tumors by Measuring Hydrogen/Deuterium Exchange in Hyperpolarized L- 1-C-13,U-H-2 Lactate." Journal of the American Chemical Society **134**(10): 4969-4977.
Kent-Braun, J. A., K. K. McCully and B. Chance (1990). "Metabolic effects of training in humans: a 31P-MRS study." J Appl Physiol (1985) **69**(3): 1165-1170.
Kim, M., J. Gillen, B. A. Landman, J. Y. Zhou and P. C. M. van Zijl (2009). "Water Saturation Shift Referencing (WASSR) for Chemical Exchange Saturation Transfer (CEST) Experiments." Magnetic Resonance in Medicine **61**(6): 1441-1450.
Klomp, D. W. J., A. N. Dula, L. R. Arlinghaus, M. Italiaander, R. D. Dortch, Z. L. Zu, J. M. Williams, D. F. Gochberg, P. R. Luijten, J. C. Gore, T. E. Yankeelov and S. A. Smith (2013). "Amide proton transfer imaging of the human breast at 7T: development and reproducibility." Nmr in Biomedicine **26**(10): 1271-1277.
Kogan, F., H. Hariharan and R. Reddy (2013). "Chemical Exchange Saturation Transfer (CEST) Imaging: Description of Technique and Potential Clinical Applications." Current Radiology Reports **1**(2): 102-114.
Kogan, F., M. Haris, C. Debrosse, A. Singh, R. P. Nanga, K. Cai, H. Hariharan and R. Reddy (2013). "In vivo chemical exchange saturation transfer imaging of creatine (CrCEST) in skeletal muscle at 3T." Journal of Magnetic Resonance Imaging: n/a-n/a.
Kogan, F., M. Haris, A. Singh, K. J. Cai, C. Debrosse, R. P. R. Nanga, H. Hariharan and R. Reddy (2014). "Method for High-Resolution Imaging of Creatine In Vivo Using Chemical Exchange Saturation Transfer." Magnetic Resonance in Medicine **71**(1): 164-172.
Kogan, F., A. Singh, C. Debrosse, M. Haris, K. J. Cai, R. P. Nanga, M. Elliott, H. Hariharan and R. Reddy (2013). "Imaging of glutamate in the spinal cord using GluCEST." Neuroimage **77**: 262-267.
Lambert, A. J. and M. D. Brand (2004). "Inhibitors of the quinone-binding site allow rapid superoxide production from mitochondrial NADH : ubiquinone oxidoreductase (complex I)." Journal of Biological Chemistry **279**(38): 39414-39420.
Lanza, I. R., S. Bhagra, K. S. Nair and J. D. Port (2011). "Measurement of human skeletal muscle oxidative capacity by 31P-MR spectroscopy: a cross-validation with in vitro measurements." J Magn Reson Imaging **34**(5): 1143-1150.
Lardinois, D., W. Weder, T. F. Hany, E. M. Kamel, S. Korom, B. Seifert, G. K. von Schulthess and H. C. Steinert (2003). "Staging of non-small-cell lung cancer with integrated positron-emission tomography and computed tomography." New England Journal of Medicine **348**(25): 2500-2507.

Lardy, H. A. and H. Wellman (1952). "Oxidative phosphorylations - role of inorganic phosphate and acceptor systems in control of metabolic rates." Journal of Biological Chemistry **195**(1): 215-224.
Larsen, R. G., D. M. Callahan, S. A. Foulis and J. A. Kent-Braun (2012). "Age-related changes in oxidative capacity differ between locomotory muscles and are associated with physical activity behavior." Appl Physiol Nutr Metab **37**(1): 88-99.
Larsson, N. G., E. Holme, B. Kristiansson, A. Oldfors and M. Tulinius (1990). "Progressive increase of the mutated mitochondrial-dna fraction in kearns-sayre syndrome." pediatric research **28**(2): 131-136.
Lauterbur, p. C. (1973). "image formation by induced local interactions - examples employing nuclear magnetic-resonance." Nature **242**(5394): 190-191.
Lee, J. H., R. A. Komoroski, W. J. Chu and J. A. Dudley (2012). Methods and Applications of Phosphorus NMR Spectroscopy In Vivo. Annual Reports on Nmr Spectroscopy, Vol 75. G. A. Webb. San Diego, Elsevier Academic Press Inc. **75:** 115-160.
Lee, S. C., M. Q. Huang, D. S. Nelson, S. Pickup, S. Wehrli, O. Adegbola, H. Poptani, E. J. Delikatny and J. D. Glickson (2008). "In vivo MRS markers of response to CHOP chemotherapy in the WSU-DLCL2 human diffuse large B-cell lymphoma xenograft." Nmr in Biomedicine **21**(7): 723-733.
Leibfritz, D. and W. Dreher (2001). "Magnetization transfer MRS." Nmr in Biomedicine **14**(2): 65-76.
Lenaz, G. (1998). "Role of mitochondria in oxidative stress and ageing." Biochimica Et Biophysica Acta-Bioenergetics **1366**(1-2): 53-67.
Levitt, M. (2008). Spin Dynamics: Basics of Nuclear Magnetic Resonance, John Wiley & Sons, Ltd.
Lin, J. D., P. H. Wu, P. T. Tarr, K. S. Lindenberg, J. St-Pierre, C. Y. Zhang, V. K. Mootha, S. Jager, C. R. Vianna, R. M. Reznick, L. B. Cui, M. Manieri, M. X. Donovan, Z. D. Wu, M. P. Cooper, M. C. Fan, L. M. Rohas, A. M. Zavacki, S. Cinti, G. I. Shulman, B. B. Lowell, D. Krainc and B. M. Spiegelman (2004). "Defects in adaptive energy metabolism with CNS-Linked hyperactivity in PGC-1 alpha null mice." Cell **119**(1): 121-+.
Little, J. P., J. B. Gillen, M. E. Percival, A. Safdar, M. A. Tarnopolsky, Z. Punthakee, M. E. Jung and M. J. Gibala (2011). "Low-volume high-intensity interval training reduces hyperglycemia and increases muscle mitochondrial capacity in patients with type 2 diabetes." J Appl Physiol (1985) **111**(6): 1554-1560.
Little, J. P., A. Safdar, D. Bishop, M. A. Tarnopolsky and M. J. Gibala (2011). "An acute bout of high-intensity interval training increases the nuclear abundance of PGC-1alpha and activates mitochondrial biogenesis in human skeletal muscle." Am J Physiol Regul Integr Comp Physiol **300**(6): R1303-1310.
Liu, G., F. Mac Gabhann and A. S. Popel (2012). "Effects of Fiber Type and Size on the Heterogeneity of Oxygen Distribution in Exercising Skeletal Muscle." Plos One **7**(9): 13.
Liu, G. S., A. A. Gilad, J. W. M. Bulte, P. C. M. van Zijl and M. T. McMahon (2010). "High-throughput screening of chemical exchange saturation transfer MR contrast agents." Contrast Media & Molecular Imaging **5**(3): 162-170.

Liu, G. S., X. L. Song, K. W. Y. Chan and M. T. McMahon (2013). "Nuts and bolts of chemical exchange saturation transfer MRI." Nmr in Biomedicine **26**(7): 810-828.
Lodi, R., J. M. Cooper, J. L. Bradley, D. Manners, P. Styles, D. J. Taylor and A. H. V. Schapira (1999). "Deficit of in vivo mitochondrial ATP production in patients with Friedreich ataxia." Proceedings of the National Academy of Sciences of the United States of America **96**(20): 11492-11495.
Low, H., P. Siekevitz, L. Ernster and O. Lindberg (1958). "Studies on the relation of the adenosinetriphosphate-inorganic phosphate exchange reaction of mitochondria to oxidative phosphorylation." Biochimica Et Biophysica Acta **29**(2): 392-405.
Luft, R., D. Ikkos, B. Afzelius, G. Palmieri and L. Ernster (1962). "A case of severe hypermetabolism of nonthyroid origin with a defect in maintenance of mitochondrial respiratory control - a correlated clinical, biochemical, and morphological study." Journal of Clinical Investigation **41**(9): 1776-&.
Maly, T., G. T. Debelouchina, V. S. Bajaj, K. N. Hu, C. G. Joo, M. L. Mak-Jurkauskas, J. R. Sirigiri, P. C. A. van der Wel, J. Herzfeld, R. J. Temkin and R. G. Griffin (2008). "Dynamic nuclear polarization at high magnetic fields." Journal of Chemical Physics **128**(5): 19.
Massoud, T. F. and S. S. Gambhir (2003). "Molecular imaging in living subjects: seeing fundamental biological processes in a new light." Genes & Development **17**(5): 545-580.
Matthews, P. M., C. Allaire, E. A. Shoubridge, G. Karpati, S. Carpenter and D. L. Arnold (1991). "In vivo muscle magnetic resonance spectroscopy in the clinical investigation of mitochondrial disease." Neurology **41**(1): 114-120.
McConnell, H. M. (1958). "Reaction rates by nuclear magnetic resonance." Journal of Chemical Physics **28**(3): 430-431.
McCord, J. M. and Fridovic.I (1969). "Superoxide dismutase an enzymic function for erythrocuprein (hemocuprein)." Journal of Biological Chemistry **244**(22): 6049-&.
McCord, J. M., B. B. Keele and I. Fridovich (1971). "Enzyme-based theory of obligate anaerobiosis - physiological function of superoxide dismutase." Proceedings of the National Academy of Sciences of the United States of America **68**(5): 1024-+.
McCormack, S. E., M. A. McCarthy, L. Farilla, M. I. Hrovat, D. M. Systrom, S. K. Grinspoon and A. Fleischman (2011). "Skeletal muscle mitochondrial function is associated with longitudinal growth velocity in children and adolescents." J Clin Endocrinol Metab **96**(10): E1612-1618.
McCormack, S. E., M. A. McCarthy, L. Farilla, M. I. Hrovat, D. M. Systrom, S. K. Grinspoon and A. Fleischman (2011). "Skeletal Muscle Mitochondrial Function Is Associated with Longitudinal Growth Velocity in Children and Adolescents." Journal of Clinical Endocrinology & Metabolism **96**(10): E1612-E1618.
McCormack, S. E., M. A. McCarthy, S. G. Harrington, L. Farilla, M. I. Hrovat, D. M. Systrom, B. J. Thomas, M. Torriani, K. McInnis, S. K. Grinspoon and A. Fleischman (2013). "Effects of exercise and lifestyle modification on fitness, insulin resistance, skeletal muscle oxidative phosphorylation and intramyocellular lipid content in obese children and adolescents." Pediatr Obes.
McMahon, M. T., A. A. Gilad, J. W. M. Bulte and P. C. M. van Zijl (2017). Chemical Exchange Saturation Transfer Imaging: Advances and Applications, CRC Press.

McMahon, M. T., A. A. Gilad, J. Y. Zhou, P. Z. Sun, J. W. M. Bulte and P. C. M. van Zijl (2006). "Quantifying exchange rates in chemical exchange saturation transfer agents using the saturation time and saturation power dependencies of the magnetization transfer effect on the magnetic resonance imaging signal (QUEST and QUESP): pH calibration for poly-L-lysine and a starburst dendrimer." Magnetic Resonance in Medicine **55**(4): 836-847.
Mecocci, P., U. Macgarvey, A. E. Kaufman, D. Koontz, J. M. Shoffner, D. C. Wallace and M. F. Beal (1993). "Oxidative damage to mitochondrial-dna shows marked age-dependent increases in human brain." Annals of Neurology **34**(4): 609-616.
Metallo, C. M. and M. G. Vander Heiden (2013). "Understanding Metabolic Regulation and Its Influence on Cell Physiology." Molecular Cell **49**(3): 388-398.
Middleton, H., R. D. Black, B. Saam, G. D. Cates, G. P. Cofer, R. Guenther, W. Happer, L. W. Hedlund, G. A. Johnson, K. Juvan and J. Swartz (1995). "MR-imaging with hyperpolarized he-3 gas." Magnetic Resonance in Medicine **33**(2): 271-275.
Milone, M., B. T. Klassen, M. L. Landsverk, R. H. Haas and L. J. Wong (2013). "Orthostatic Tremor, Progressive External Ophthalmoplegia, and Twinkle." Jama Neurology **70**(11): 1429-1431.
Misbin, R. I., L. Green, B. V. Stadel, J. L. Gueriguian, A. Gubbi and G. A. Fleming (1998). "Lactic acidosis in patients with diabetes treated with metformin." New England Journal of Medicine **338**(4): 265-266.
Mitchell, P. (1991). "FOUNDATIONS OF VECTORIAL METABOLISM AND OSMOCHEMISTRY." Bioscience Reports **11**(6): 297-346.
Mitchell, P. and J. Moyle (1965). "STOICHIOMETRY OF PROTON TRANSLOCATION THROUGH RESPIRATORY CHAIN AND ADENOSINE TRIPHOSPHATASE SYSTEMS OF RAT LIVER MITOCHONDRIA." Nature **208**(5006): 147-&.
Mitchell, P. and J. Moyle (1967). "CHEMIOSMOTIC HYPOTHESIS OF OXIDATIVE PHOSPHORYLATION." Nature **213**(5072): 137-&.
Moats, R. A., S. E. Fraser and T. J. Meade (1997). "A "smart" magnetic resonance imaging agent that reports on specific enzymatic activity." Angewandte Chemie-International Edition in English **36**(7): 726-728.
Mohammad, R. M., N. R. Wall, J. A. Dutcher and A. M. Al-Katib (2000). "The addition of bryostatin 1 to cyclophosphamide, doxorubicin, vincristine, and prednisone (CHOP) chemotherapy improves response in a CHOP-resistant human diffuse large cell lymphoma xenograft model." Clinical Cancer Research **6**(12): 4950-4956.
Moon, R. B. and J. H. Richards (1973). "Determination of intracellular pH by P-31 magnetic-resonance." Journal of Biological Chemistry **248**(20): 7276-7278.
Moraes, C. T., S. Shanske, H. J. Tritschler, J. R. Aprille, F. Andreetta, E. Bonilla, E. A. Schon and S. Dimauro (1991). "MTDNA DEPLETION WITH VARIABLE TISSUE EXPRESSION - A NOVEL GENETIC ABNORMALITY IN MITOCHONDRIAL DISEASES." American Journal of Human Genetics **48**(3): 492-501.
Muller, F. L., Y. H. Liu and H. Van Remmen (2004). "Complex III releases superoxide to both sides of the inner mitochondrial membrane." Journal of Biological Chemistry **279**(47): 49064-49073.

Murphy, J. L., E. L. Blakely, A. M. Schaefer, L. He, P. Wyrick, R. G. Haller, R. W. Taylor, D. M. Turnbull and T. Taivassalo (2008). "Resistance training in patients with single, large-scale deletions of mitochondrial DNA." Brain **131**(Pt 11): 2832-2840.
Nasrallah, F., M. Feki and N. Kaabachi (2010). "Creatine and Creatine Deficiency Syndromes: Biochemical and Clinical Aspects." Pediatric Neurology **42**(3): 163-171.
Navon, G., Y. Q. Song, T. Room, S. Appelt, R. E. Taylor and A. Pines (1996). "Enhancement of solution NMR and MRI with laser-polarized xenon." Science **271**(5257): 1848-1851.
Nelson, S. J., J. Kurhanewicz, D. B. Vigneron, P. E. Z. Larson, A. L. Harzstark, M. Ferrone, M. van Criekinge, J. W. Chang, R. Bok, I. Park, G. Reed, L. Carvajal, E. J. Small, P. Munster, V. K. Weinberg, J. H. Ardenkjaer-Larsen, A. P. Chen, R. E. Hurd, L. I. Odegardstuen, F. J. Robb, J. Tropp and J. A. Murray (2013). "Metabolic Imaging of Patients with Prostate Cancer Using Hyperpolarized 1-C-13 Pyruvate." Science Translational Medicine **5**(198): 10.
Newman, N. J., M. T. Lott and D. C. Wallace (1991). "THE CLINICAL CHARACTERISTICS OF PEDIGREES OF LEBERS HEREDITARY OPTIC NEUROPATHY WITH THE 11778 MUTATION." American Journal of Ophthalmology **111**(6): 750-762.
Nouioua, S., D. Cheillan, S. Zaouidi, G. S. Salomons, N. Amedjout, F. Kessaci, N. Boulandour, T. Hamadouche and M. Tazir (2013). "Creatine deficiency syndrome. A treatable myopathy due to arginine-glycine amidinotransferase (AGAT) deficiency." Neuromuscular Disorders **23**(8): 670-674.
Ogawa, S., T. M. Lee, A. R. Kay and D. W. Tank (1990). "BRAIN MAGNETIC-RESONANCE-IMAGING WITH CONTRAST DEPENDENT ON BLOOD OXYGENATION." Proceedings of the National Academy of Sciences of the United States of America **87**(24): 9868-9872.
Ordidge, R. J., A. Connelly and J. A. B. Lohman (1986). "IMAGE-SELECTED INVIVO SPECTROSCOPY (ISIS) - A NEW TECHNIQUE FOR SPATIALLY SELECTIVE NMR-SPECTROSCOPY." Journal of Magnetic Resonance **66**(2): 283-294.
Padhani, A. R. and J. E. Husband (2001). "Dynamic contrast-enhanced MRI studies in oncology with an emphasis on quantification, validation and human studies." Clinical Radiology **56**(8): 607-620.
Pagliarini, D. J., S. E. Calvo, B. Chang, S. A. Sheth, S. B. Vafai, S.-E. Ong, G. A. Walford, C. Sugiana, A. Boneh, W. K. Chen, D. E. Hill, M. Vidal, J. G. Evans, D. R. Thorburn, S. A. Carr and V. K. Mootha (2008). "A mitochondrial protein compendium elucidates complex I disease biology." Cell **134**(1): 112-123.
Pampols, T. (2010). Inherited Metabolic Rare Disease. Rare Diseases Epidemiology. M. P. DelaPaz and S. C. Groft. Berlin, Springer-Verlag Berlin. **686:** 397-431.
Parasoglou, P., D. Xia, G. Chang and R. R. Regatte (2013). "Dynamic three-dimensional imaging of phosphocreatine recovery kinetics in the human lower leg muscles at 3T and 7T: a preliminary study." Nmr in Biomedicine **26**(3): 348-356.
Parikh, S., A. Goldstein, M. K. Koenig, F. Scaglia, G. M. Enns, R. Saneto, I. Anselm, B. H. Cohen, M. J. Falk, C. Greene, A. L. Gropman, R. Haas, M. Hirano, P. Morgan, K. Sims, M. Tarnopolsky, J. L. Van Hove, L. Wolfe and S. DiMauro (2014). "Diagnosis and

management of mitochondrial disease: a consensus statement from the Mitochondrial Medicine Society." Genet Med.
Parikh, S., R. Saneto, M. J. Falk, I. Anselm, B. H. Cohen, R. Haas and T. M. Medicine Society (2009). "A modern approach to the treatment of mitochondrial disease." Curr Treat Options Neurol **11**(6): 414-430.
Penn, A. M., J. W. Lee, P. Thuillier, M. Wagner, K. M. Maclure, M. R. Menard, L. D. Hall and N. G. Kennaway (1992). "MELAS syndrome with mitochondrial tRNA(Leu)(UUR) mutation: correlation of clinical state, nerve conduction, and muscle 31P magnetic resonance spectroscopy during treatment with nicotinamide and riboflavin." Neurology **42**(11): 2147-2152.
Phelps, M. E. (2000). "Positron emission tomography provides molecular imaging of biological processes." Proceedings of the National Academy of Sciences of the United States of America **97**(16): 9226-9233.
Picard, M., D. C. Wallace and Y. Burelle (2016). "The rise of mitochondria in medicine." Mitochondrion **30**: 105-116.
Pickup, S., S. C. Lee, A. Mancuso and J. D. Glickson (2008). "Lactate imaging with Hadamard-encoded slice-selective multiple quantum coherence chemical-shift imaging." Magnetic Resonance in Medicine **60**(2): 299-305.
Pikkemaat, J. A., R. T. Wegh, R. Lamerichs, R. A. van de Molengraaf, S. Langereis, D. Burdinski, A. Y. F. Raymond, H. M. Janssen, B. F. M. de Waal, N. P. Willard, E. W. Meijer and H. Grull (2007). "Dendritic PARACEST contrast agents for magnetic resonance imaging." Contrast Media & Molecular Imaging **2**(5): 229-239.
Pizer, E. S., F. D. Wood, H. S. Heine, F. E. Romantsev, G. R. Pasternack and F. P. Kuhajda (1996). "Inhibition of fatty acid synthesis delays disease progression in a xenograft model of ovarian cancer." Cancer Research **56**(6): 1189-1193.
Plathow, C. and W. A. Weber (2008). "Tumor cell metabolism imaging." Journal of Nuclear Medicine **49**: 43S-63S.
Potter, M., E. Newport and K. J. Morten (2016). "The Warburg effect: 80 years on." Biochemical Society Transactions **44**: 1499-1505.
Proctor, D. N., W. E. Sinning, J. M. Walro, G. C. Sieck and P. W. R. Lemon (1995). "OXIDATIVE CAPACITY OF HUMAN MUSCLE-FIBER TYPES - EFFECTS OF AGE AND TRAINING STATUS." Journal of Applied Physiology **78**(6): 2033-2038.
Rashid, A., E. S. Pizer, M. Moga, L. Z. Milgraum, M. Zahurak, G. R. Pasternack, F. P. Kuhajda and S. R. Hamilton (1997). "Elevated expression of fatty acid synthase and fatty acid synthetic activity in colorectal neoplasia." American Journal of Pathology **150**(1): 201-208.
Ricardo, A. C., C. A. Anderson, W. Yang, X. Zhang, M. J. Fischer, L. M. Dember, J. C. Fink, A. Frydrych, N. G. Jensvold, E. Lustigova, L. C. Nessel, A. C. Porter, M. Rahman, J. A. Wright Nunes, M. L. Daviglus, J. P. Lash and C. S. Investigators (2015). "Healthy lifestyle and risk of kidney disease progression, atherosclerotic events, and death in CKD: findings from the Chronic Renal Insufficiency Cohort (CRIC) Study." Am J Kidney Dis **65**(3): 412-424.
Roalf, D. R., R. P. R. Nanga, P. E. Rupert, H. Hariharan, M. Quarmley, M. E. Calkins, E. Dress, K. Prabhakaran, M. A. Elliott, P. J. Moberg, R. C. Gur, R. E. Gur, R. Reddy and

B. I. Turetsky "Glutamate imaging (GluCEST) reveals lower brain GluCEST contrast in patients on the psychosis spectrum."
Rogosnitzky, M. and S. Branch (2016). "Gadolinium-based contrast agent toxicity: a review of known and proposed mechanisms." Biometals **29**(3): 365-376.
Rotig, A., V. Cormier, S. Blanche, J. P. Bonnefont, F. Ledeist, N. Romero, J. Schmitz, P. Rustin, A. Fischer, J. M. Saudubray and A. Munnich (1990). "PEARSON MARROW PANCREAS SYNDROME - A MULTISYSTEM MITOCHONDRIAL DISORDER IN INFANCY." Journal of Clinical Investigation **86**(5): 1601-1608.
Roussel, M., D. Bendahan, J. P. Mattei, Y. Le Fur and P. J. Cozzone (2000). "P-31 magnetic resonance spectroscopy study of phosphocreatine recovery kinetics in skeletal muscle: the issue of intersubject variability." Biochimica Et Biophysica Acta-Bioenergetics **1457**(1-2): 18-26.
Saks, V. A., R. VenturaClapier and M. K. Aliev (1996). "Metabolic control and metabolic capacity: Two aspects of creatine kinase functioning in the cells." Biochimica Et Biophysica Acta-Bioenergetics **1274**(3): 81-88.
Scheuermann-Freestone, M., P. L. Madsen, D. Manners, A. M. Blamire, R. E. Buckingham, P. Styles, G. K. Radda, S. Neubauer and K. Clarke (2003). "Abnormal cardiac and skeletal muscle energy metabolism in patients with type 2 diabetes." Circulation **107**(24): 3040-3046.
Schiaffino, S. and C. Reggiani (2011). "FIBER TYPES IN MAMMALIAN SKELETAL MUSCLES." Physiological Reviews **91**(4): 1447-1531.
Scholz, R., R. G. Thurman, J. R. Williamson, B. Chance and T. Bucher (1969). "FLAVIN AND PYRIDINE NUCLEOTIDE OXIDATION-REDUCTION CHANGES IN PERFUSED RAT LIVER .I. ANOXIA AND SUBCELLULAR LOCALIZATION OF FLUORESCENT FLAVOPROTEINS." Journal of Biological Chemistry **244**(9): 2317-+.
Schrauwen-Hinderling, V. B., M. E. Kooi and P. Schrauwen (2016). "Mitochondrial Function and Diabetes: Consequences for Skeletal and Cardiac Muscle Metabolism." Antioxidants & Redox Signaling **24**(1): 39-51.
Schriner, S. E., C. E. Ogburn, A. C. Smith, T. G. Newcomb, W. C. Ladiges, M. E. T. Dolle, J. Vijg, K. I. Fukuchi and G. M. Martin (2000). "Levels of DNA damage are unaltered in mice overexpressing human catalase in nuclei." Free Radical Biology and Medicine **29**(7): 664-673.
Shanske, S., C. T. Moraes, A. Lombes, A. F. Miranda, E. Bonilla, P. Lewis, M. A. Whelan, C. A. Ellsworth and S. Dimauro (1990). "WIDESPREAD TISSUE DISTRIBUTION OF MITOCHONDRIAL-DNA DELETIONS IN KEARNS-SAYRE SYNDROME." Neurology **40**(1): 24-28.
Sherry, A. D. and M. Woods (2008). Chemical exchange saturation transfer contrast agents for magnetic resonance imaging. Annual Review of Biomedical Engineering. **10:** 391-411.
Sherry, A. D. and M. Woods (2008). "Chemical exchange saturation transfer contrast agents for magnetic resonance imaging." Annu Rev Biomed Eng **10**: 391-411.

Shoffner, J. M., M. T. Lott and D. C. Wallace (1991). "MERRF - A MODEL DISEASE FOR UNDERSTANDING THE PRINCIPLES OF MITOCHONDRIAL GENETICS." Revue Neurologique **147**(6-7): 431-435.
Shoffner, J. M., M. T. Lott and D. C. Wallace (1991). "MERRF: a model disease for understanding the principles of mitochondrial genetics." Rev Neurol (Paris) **147**(6-7): 431-435.
Shoubridge, E. A., G. Karpati and K. E. M. Hastings (1990). "DELETION MUTANTS ARE FUNCTIONALLY DOMINANT OVER WILD-TYPE MITOCHONDRIAL GENOMES IN SKELETAL-MUSCLE FIBER SEGMENTS IN MITOCHONDRIAL DISEASE." Cell **62**(1): 43-49.
Sies, H. (1997). "Oxidative stress: Oxidants and antioxidants." Experimental Physiology **82**(2): 291-295.
Simoneau, J. A., S. R. Colberg, F. L. Thaete and D. E. Kelley (1995). "SKELETAL-MUSCLE GLYCOLYTIC AND OXIDATIVE ENZYME CAPACITIES ARE DETERMINANTS OF INSULIN SENSITIVITY AND MUSCLE COMPOSITION IN OBESE WOMEN." Faseb Journal **9**(2): 273-278.
Simoneau, J. A. and D. E. Kelley (1997). "Altered glycolytic and oxidative capacities of skeletal muscle contribute to insulin resistance in NIDDM." Journal of Applied Physiology **83**(1): 166-171.
Singh, A., K. J. Cai, M. Haris, H. Hariharan and R. Reddy (2013). "On B1 inhomogeneity correction of in vivo human brain glutamate chemical exchange saturation transfer contrast at 7T." Magnetic Resonance in Medicine **69**(3): 818-824.
Singh, A., M. Haris, K. Cai, H. Hariharan and R. Reddy (2011). Chemical exchange transfer imaging of creatine. Proceedings of the 19th annual meeting of ISMRM, Montreal.
Singh, A., M. Haris, K. Cai, V. B. Kassey, F. Kogan, D. Reddy, H. Hariharan and R. Reddy (2012). "Chemical exchange saturation transfer magnetic resonance imaging of human knee cartilage at 3 T and 7 T." Magnetic Resonance in Medicine **68**(2): 588-594.
Sleigh, A., V. Lupson, A. Thankamony, D. B. Dunger, D. B. Savage, T. A. Carpenter and G. J. Kemp (2016). "Simple and effective exercise design for assessing in vivo mitochondrial function in clinical applications using P-31 magnetic resonance spectroscopy." Scientific Reports **6**: 9.
Spelbrink, J. N., F. Y. Li, V. Tiranti, K. Nikali, Q. P. Yuan, M. Tariq, S. Wanrooij, N. Garrido, G. Comi, L. Morandi, L. Santoro, A. Toscano, G. M. Fabrizi, H. Somer, R. Croxen, D. Beeson, J. Poulton, A. Suomalainen, H. T. Jacobs, M. Zeviani and C. Larsson (2001). "Human mitochondrial DNA deletions associated with mutations in the gene encoding Twinkle, a phage T7 gene 4-like protein localized in mitochondria." Nat Genet **28**(3): 223-231.
Stacpoole, P. W., T. J. deGrauw, A. S. Feigenbaum, C. Hoppel, D. S. Kerr, S. E. McCandless, M. V. Miles, B. H. Robinson and P. H. Tang (2012). "Design and implementation of the first randomized controlled trial of coenzyme CoQ(1)(0) in children with primary mitochondrial diseases." Mitochondrion **12**(6): 623-629.

Stanisz, G. J., E. E. Odrobina, J. Pun, M. Escaravage, S. J. Graham, M. J. Bronskill and R. M. Henkelman (2005). "T-1, T-2 relaxation and magnetization transfer in tissue at 3T." Magnetic Resonance in Medicine **54**(3): 507-512.
Steiner, J. L., E. A. Murphy, J. L. McClellan, M. D. Carmichael and J. M. Davis (2011). "Exercise training increases mitochondrial biogenesis in the brain." Journal of Applied Physiology **111**(4): 1066-1071.
Sun, P. Z., Y. Wang, Z. Z. Dai, G. Xiao and R. H. Wu (2014). "Quantitative chemical exchange saturation transfer (qCEST) MRI - RF spillover effect-corrected omega plot for simultaneous determination of labile proton fraction ratio and exchange rate." Contrast Media & Molecular Imaging **9**(4): 268-275.
Szewczyk, A. and L. Wojtczak (2002). "Mitochondria as a pharmacological target." Pharmacological Reviews **54**(1): 101-127.
Tarnopolsky, M. A. (2014). "Exercise as a therapeutic strategy for primary mitochondrial cytopathies." J Child Neurol **29**(9): 1225-1234.
Tarnopolsky, M. A. and G. Parise (1999). "Direct measurement of high-energy phosphate compounds in patients with neuromuscular disease." Muscle & Nerve **22**(9): 1228-1233.
Tarnopolsky, M. A., A. Parshad, B. Walzel, U. Schlattner and T. Wallimann (2001). "Creatine transporter and mitochondrial creatine kinase protein content in myopathies." Muscle & Nerve **24**(5): 682-688.
Terreno, E., D. Delli Castelli, A. Viale and S. Aime (2010). "Challenges for Molecular Magnetic Resonance Imaging." Chemical Reviews **110**(5): 3019-3042.
Thompson, C. H., G. J. Kemp, A. L. Sanderson and G. K. Radda (1995). "SKELETAL-MUSCLE MITOCHONDRIAL-FUNCTION STUDIED BY KINETIC-ANALYSIS OF POSTEXERCISE PHOSPHOCREATINE RESYNTHESIS." Journal of Applied Physiology **78**(6): 2131-2139.
Trappe, S. W., T. A. Trappe, G. A. Lee and D. L. Costill (2001). "Calf muscle strength in humans." Int J Sports Med **22**(3): 186-191.
Treberg, J. R., C. L. Quinlan and M. D. Brand (2011). "Evidence for Two Sites of Superoxide Production by Mitochondrial NADH-Ubiquinone Oxidoreductase (Complex I)." Journal of Biological Chemistry **286**(31): 27103-27110.
Turrens, J. F. (2003). "Mitochondrial formation of reactive oxygen species." Journal of Physiology-London **552**(2): 335-344.
Turrens, J. F., B. A. Freeman, J. G. Levitt and J. D. Crapo (1982). "THE EFFECT OF HYPEROXIA ON SUPEROXIDE PRODUCTION BY LUNG SUB-MITOCHONDRIAL PARTICLES." Archives of Biochemistry and Biophysics **217**(2): 401-410.
van Zijl, P. C. and N. N. Yadav (2011). "Chemical exchange saturation transfer (CEST): what is in a name and what isn't?" Magn Reson Med **65**(4): 927-948.
van Zijl, P. C. M., C. K. Jones, J. Ren, C. R. Malloy and A. D. Sherry (2007). "MR1 detection of glycogen in vivo by using chemical exchange saturation transfer imaging (glycoCEST)." Proceedings of the National Academy of Sciences of the United States of America **104**(11): 4359-4364.

van Zijl, P. C. M. and N. N. Yadav (2011). "Chemical Exchange Saturation Transfer (CEST): What is in a Name and What Isn't?" Magnetic Resonance in Medicine **65**(4): 927-948.
Venditti, P., L. Di Stefano and S. Di Meo (2013). "Mitochondrial metabolism of reactive oxygen species." Mitochondrion **13**(2): 71-82.
Viswanathan, S., Z. Kovacs, K. N. Green, S. J. Ratnakar and A. D. Sherry (2010). "Alternatives to Gadolinium-Based Metal Chelates for Magnetic Resonance Imaging." Chemical Reviews **110**(5): 2960-3018.
Viswanathan, S., S. J. Ratnakar, K. N. Green, Z. Kovacs, L. M. De Leon-Rodriguez and A. D. Sherry (2009). "Multi-Frequency PARACEST Agents Based on Europium(III)-DOTA-Tetraamide Ligands." Angewandte Chemie-International Edition **48**(49): 9330-9333.
Walenta, S., M. Wetterling, M. Lehrke, G. Schwickert, K. Sundfor, E. K. Rofstad and W. Mueller-Klieser (2000). "High lactate levels predict likelihood of metastases, tumor recurrence, and restricted patient survival in human cervical cancers." Cancer Research **60**(4): 916-921.
Walker-Samuel, S., R. Ramasawmy, F. Torrealdea, M. Rega, V. Rajkumar, S. P. Johnson, S. Richardson, M. Goncalves, H. G. Parkes, E. Arstad, D. L. Thomas, R. B. Pedley, M. F. Lythgoe and X. Golay (2013). "In vivo imaging of glucose uptake and metabolism in tumors." Nature Medicine **19**(8): 1067-+.
Wall, M. and S. A. Newman (1991). "OPTIC-NERVE SHEATH DECOMPRESSION FOR THE TREATMENT OF PROGRESSIVE NONARTERITIC ISCHEMIC OPTIC NEUROPATHY." American Journal of Ophthalmology **112**(6): 741-741.
Wallace, D. C. (1989). "MITOCHONDRIAL-DNA MUTATIONS AND NEUROMUSCULAR DISEASE." Trends in Genetics **5**(1): 9-13.
Wallace, D. C. (1992). "DISEASES OF THE MITOCHONDRIAL-DNA." Annual Review of Biochemistry **61**: 1175-1212.
Wallace, D. C. (1992). "MITOCHONDRIAL GENETICS - A PARADIGM FOR AGING AND DEGENERATIVE DISEASES." Science **256**(5057): 628-632.
Wallace, D. C. (1999). "Mitochondrial diseases in man and mouse." Science **283**(5407): 1482-1488.
Wallace, D. C. (2005). A mitochondrial paradigm of metabolic and degenerative diseases, aging, and cancer: A dawn for evolutionary medicine. Annual Review of Genetics. Palo Alto, Annual Reviews. **39:** 359-407.
Wallace, D. C. (2007). Why do we still have a maternally inherited mitochondrial DNA? Insights from evolutionary medicine. Annual Review of Biochemistry. Palo Alto, Annual Reviews. **76:** 781-821.
Wallace, D. C. (2010). "Mitochondrial DNA Mutations in Disease and Aging." Environmental and Molecular Mutagenesis **51**(5): 440-450.
Wallace, D. C. (2013). "A mitochondrial bioenergetic etiology of disease." Journal of Clinical Investigation **123**(4): 1405-1412.
Wallace, D. C. (2013). "A mitochondrial bioenergetic etiology of disease." J Clin Invest **123**(4): 1405-1412.

Wallace, D. C. (2013). "Bioenergetics in human evolution and disease: implications for the origins of biological complexity and the missing genetic variation of common diseases." Philosophical Transactions of the Royal Society B-Biological Sciences **368**(1622).
Wallace, D. C. (2015). "Mitochondrial DNA Variation in Human Radiation and Disease." Cell **163**(1): 33-38.
Wallimann, T., M. Tokarska-Schlattner and U. Schlattner (2011). "The creatine kinase system and pleiotropic effects of creatine." Amino Acids **40**(5): 1271-1296.
Wallimann, T., M. Wyss, D. Brdiczka, K. Nicolay and H. M. Eppenberger (1992). "Intracellular compartmentation, structure and function of creatine-kinase isoenzymes in tissues with high and fluctuating energy demands - the phosphocreatine circuit for cellular-energy homeostasis." Biochemical Journal **281**: 21-40.
Wang, B.-D., O. M. Rennert and Y. A. Su (2008). "Mitochondrial Oxidative Phosphorylation, Obesity and Diabetes." Cellscience **4**(4): 57-81.
Wang, J. H., J. Weygand, K. P. Hwang, A. S. R. Mohamed, Y. Ding, C. D. Fuller, S. Y. Lai, S. J. Frank and J. Y. Zhou (2016). "Magnetic Resonance Imaging of Glucose Uptake and Metabolism in Patients with Head and Neck Cancer." Scientific Reports **6**: 7.
Wang, L. H. V. and S. Hu (2012). "Photoacoustic Tomography: In Vivo Imaging from Organelles to Organs." Science **335**(6075): 1458-1462.
Wang, T., C. Marquardt and J. Foker (1976). "AEROBIC GLYCOLYSIS DURING LYMPHOCYTE-PROLIFERATION." Nature **261**(5562): 702-705.
Warburg, O. (1956). "ORIGIN OF CANCER CELLS." Science **123**(3191): 309-314.
Ward, K. M., A. H. Aletras and R. S. Balaban (2000). "A new class of contrast agents for MRI based on proton chemical exchange dependent saturation transfer (CEST)." Journal of Magnetic Resonance **143**(1): 79-87.
Waterhouse, C. (1974). "LACTATE METABOLISM IN PATIENTS WITH CANCER." Cancer **33**(1): 66-71.
Wegner, A., J. Meiser, D. Weindl and K. Hiller (2015). "How metabolites modulate metabolic flux." Current Opinion in Biotechnology **34**: 16-22.
Wei, Y. H., C. Y. Lu, H. C. Lee, C. Y. Pang and Y. S. Ma (1998). "Oxidative damage and mutation to mitochondrial DNA and age-dependent decline of mitochondrial respiratory function." Towards Prolongation of the Healthy Life Span: Practical Approaches to Intervention **854**: 155-170.
Willmann, J. K., N. van Bruggen, L. M. Dinkelborg and S. S. Gambhir (2008). "Molecular imaging in drug development." Nature Reviews Drug Discovery **7**(7): 591-607.
Wilson, N. E. (2016). ExerciseCEST.
Woessner, D. E., S. R. Zhang, M. E. Merritt and A. D. Sherry (2005). "Numerical solution of the Bloch equations provides insights into the optimum design of PARACEST agents for MRI." Magnetic Resonance in Medicine **53**(4): 790-799.
Wolfe, R. R. (2006). "The underappreciated role of muscle in health and disease." American Journal of Clinical Nutrition **84**(3): 475-482.
Wolff, S. D. and R. S. Balaban (1990). "NMR IMAGING OF LABILE PROTON-EXCHANGE." Journal of Magnetic Resonance **86**(1): 164-169.

Woods, M., E. W. C. Donald and A. D. Sherry (2006). "Paramagnetic lanthanide complexes as PARACEST agents for medical imaging." Chemical Society Reviews **35**(6): 500-511.
Wouters, F. S., P. J. Verveer and P. I. H. Bastiaens (2001). "Imaging biochemistry inside cells." Trends in Cell Biology **11**(5): 203-211.
Wyss, M., J. Smeitink, R. A. Wevers and T. Wallimann (1992). "MITOCHONDRIAL CREATINE-KINASE - A KEY ENZYME OF AEROBIC ENERGY-METABOLISM." Biochimica Et Biophysica Acta **1102**(2): 119-166.
Yabe, T., K. Mitsunami, T. Inubushi and M. Kinoshita (1995). "Quantiative measurements of cardiac phosphorous metabolites in coronary-artery disease by P-31 magnetic-resonance spectroscopy." Circulation **92**(1): 15-23.
Yadav, N. N., J. D. Xu, A. Bar-Shir, Q. Qin, K. W. Y. Chan, K. Grgac, W. B. Li, M. T. McMahon and P. C. M. van Zijl (2014). "Natural D-Glucose as a Biodegradable MRI Relaxation Agent." Magnetic Resonance in Medicine **72**(3): 823-828.
Yoo, B. and M. D. Pagel (2006). "A PARACEST MRI contrast agent to detect enzyme activity." Journal of the American Chemical Society **128**(43): 14032-14033.
Yoo, B., M. S. Raam, R. M. Rosenblum and M. D. Pagel (2007). "Enzyme-responsive PARACEST MRI contrast agents: a new biomedical imaging approach for studies of the proteasome." Contrast Media & Molecular Imaging **2**(4): 189-198.
Zhang, L., A. F. Martins, Y. Mai, P. Zhao, A. M. Funk, M. V. Jordan, S. Zhang, W. Chen, Y. Wu and A. D. Sherry (2017). "Imaging Extracellular Lactate In Vitro and In Vivo Using CEST MRI and a Paramagnetic Shift Reagent." Chem. Eur. J. **23**: 1752-1756.
Zhang, S. R., C. R. Malloy and A. D. Sherry (2005). "MRI thermometry based on PARACEST agents." Journal of the American Chemical Society **127**(50): 17572-17573.
Zhang, S. R., M. Merritt, D. E. Woessner, R. E. Lenkinski and A. D. Sherry (2003). "PARACEST agents: Modulating MRI contrast via water proton exchange." Accounts of Chemical Research **36**(10): 783-790.
Zhou, J., J. O. Blakeley, J. Hua, M. Kim, J. Laterra, M. G. Pomper and P. C. M. van Zijl (2008). "Practical data acquisition method for human brain tumor amide proton transfer (APT) imaging." Magnetic Resonance in Medicine **60**(4): 842-849.
Zhou, J. and P. C. M. van Zijl (2006). "Chemical exchange saturation transfer imaging and spectroscopy." Progress in Nuclear Magnetic Resonance Spectroscopy **48**(2-3): 109-136.
Zhou, J. Y., B. Lal, D. A. Wilson, J. Laterra and P. C. M. van Zijl (2003). "Amide proton transfer (APT) contrast for imaging of brain tumors." Magnetic Resonance in Medicine **50**(6): 1120-1126.
Zhou, J. Y., J. F. Payen, D. A. Wilson, R. J. Traystman and P. C. M. van Zijl (2003). "Using the amide proton signals of intracellular proteins and peptides to detect pH effects in MRI." Nature Medicine **9**(8): 1085-1090.
Zhou, J. Y., D. A. Wilson, P. Z. Sun, J. A. Klaus and P. C. M. van Zijl (2004). "Quantitative description of proton exchange processes between water and endogenous and exogenous agents for WEX, CEST, and APT experiments." Magnetic Resonance in Medicine **51**(5): 945-952.

Zierath, J. R. and J. A. Hawley (2004). "Skeletal muscle fiber type: Influence on contractile and metabolic properties." Plos Biology **2**(10): 1523-1527.
Zierz, C. M., P. R. Joshi and S. Zierz (2015). "Frequencies of myohistological mitochondrial changes in patients with mitochondrial DNA deletions and the common m.3243A > G point mutation." Neuropathology **35**(2): 130-136.
Zimmerman, J. (2005) "Functional metabolism: Regulation and adaptation: Storey, K. B. (ed.)."